

Boston University

OpenBU

<http://open.bu.edu>

Theses & Dissertations

Boston University Theses & Dissertations

2015

Strain engineering of graphene

<https://hdl.handle.net/2144/16093>

Boston University

BOSTON UNIVERSITY
COLLEGE OF ENGINEERING

Dissertation

STRAIN ENGINEERING OF GRAPHENE

by

ZENAN QI

B.S., University of Science and Technology of China, 2010
M.S., Boston University, 2012

Submitted in partial fulfillment of the
requirements for the degree of
Doctor of Philosophy

2015

© 2015 by
ZENAN QI
All rights reserved

Approved by

First Reader

Harold S. Park, PhD
Associate Professor of Mechanical Engineering

Second Reader

David K. Campbell, PhD
Professor of Physics
Professor of Electrical and Computer Engineering
Professor of Materials Science and Engineering

Third Reader

Joseph Scott Bunch, PhD
Assistant Professor of Mechanical Engineering
Assistant Professor of Materials Science and Engineering
Assistant Professor of Physics

Fourth Reader

Chuanhua Duan, PhD
Assistant Professor of Mechanical Engineering

There are only two ways to live your life. One is as though nothing is a miracle. The other is as though everything is a miracle.

Albert Einstein

Acknowledgments

I would like to first of all thank my advisors Prof. Harold S. Park and Prof. David K. Campbell, without whom my PhD journey wouldn't have been possible. You have always been supportive and taught me so much about how to do high-quality research; I enjoyed discussing mechanics with Prof. Park on various topics, and learning interesting solid state physics and quantum mechanics with Prof. Campbell. You have been my academic role models and trying the best to help me become an independent thinker and comprehensive researcher, strengthen my knowledge and broaden my horizons. I will surely benefit from this unique training and experience throughout my career.

An important part of my PhD is having the chance to work with Prof. Antonio H. Castro Neto and Prof. Vitor M. Pereira from National University of Singapore (NUS). Prof. Castro Neto's profound knowledge and insight in physics deeply impressed me, and the inspiring vision and optimism encouraged me to overcome all the difficulties through the fruitful research project on graphene electro-mechanical coupling. Prof. Pereira's solid condensed matter physics foundation and the terrific ability to teach complicated subjects lucidly helped me significantly to finish the main section of my thesis. I also thank my great collaborator Dr. Dario A. Bahamon, who conducted the transport calculations. Additionally, I thank the help from Miguel and all other colleagues at NUS. I acknowledge the financial support from Banco Santander for partial support of my trips to the NUS.

I thank Dr. Alexander L. Kitt for many informative discussions and inspiring ideas. You have been such an intelligent, modest and hardworking guy; our papers wouldn't be as good without your efforts. I thank Prof. Swan and Prof. Goldberg for the helpful meetings, and also thank Ted Pudlik and all the graduate students of physics and mechanical engineering for debates and discussions. Many of my other

PhD projects were done in collaboration as well; specifically, I'd like to thank, just to name a few, Prof. Andreas Isacsson, Dr. Daniel Midtvedt and Dr. Alexander Croy (all from Chalmers University of Technology) on the graphene resonator project and also thank Prof. Isacsson for inviting me to visit Sweden; Prof. Jin-wu Jiang (Shanghai University) on the MoS₂ project; Dr. Guiping Zhang (Renmin University of China) on the graphene sensor project; Dr. Penghui Cao (labmate, now at MIT) on the edge stress project. I'd also like to thank the comments and suggestions from Prof. Hengan Wu (USTC), Prof. Sulin Zhang, Prof. Liangbing Hu, etc. I acknowledge support from the Department of Mechanical Engineering and the Physics Department of Boston University; I acknowledge support from NUS which made my visits to Singapore possible.

I am grateful to all my labmates, Penghui, Shuangxing, Xue, Jin, Weiwei, Gwongchan, etc. who are not just research partners but lifetime friends. We have been through both difficulties and achievements all the way through. There are many great memories that we will cherish for a long time, such as the proposal, you know what I am talking about. I sincerely wish all of you a successful future and wonderful life.

Last but foremost, I thank my family, Yan, and all my friends for always being there at my different life stages. I, through five years' work, become a PhD; and you, Yan, after more than five years, became my wife.

Zenan Qi

STRAIN ENGINEERING OF GRAPHENE

ZENAN QI

Boston University, College of Engineering, 2015

Major Professors: Harold S. Park, PhD

Associate Professor of Mechanical Engineering

David K. Campbell, PhD

Professor of Physics

Professor of Electrical and Computer Engineering

Professor of Materials Science and Engineering

ABSTRACT

The focus of this thesis is on using mechanical strain to tailor the electronic properties of graphene. The first half covers the electro-mechanical coupling for graphene in different configurations, namely a hexagonal Y-junction, various shaped bubbles on different substrates, and with kirigami cuts. For all of these cases, a novel combination of tight-binding electronic structure calculations and molecular dynamics is utilized to demonstrate how mechanical loading and deformation impacts the resulting electronic structure and transport. For the Y-junction, a quasi-uniform pseudo magnetic field induced by strain restricts transport to Landau-level and edge-state-assisted resonant tunneling. For the bubbles, the shape and the nature of the substrate emerge as decisive factors determining the effectiveness of the nanoscale pseudo magnetic field tailoring in graphene. Finally, for the kirigami, it is shown that the yield and fracture strains of graphene, a well-known brittle material, can be enhanced by a factor of more than three using the kirigami structure, while also leading to significant enhancements in the localized pseudo magnetic fields.

The second part of the thesis focuses on dissipation mechanisms in graphene nanomechanical resonators. Thermalization in nonlinear systems is a central concept in statistical mechanics and has been extensively studied theoretically since the seminal work of Fermi, Pasta, and Ulam (FPU). Using molecular dynamics and continuum modeling of a ring-down setup, it is shown that thermalization due to nonlinear mode coupling intrinsically limits the quality factor of nanomechanical graphene drums and turns them into potential test beds for FPU physics. The relationship between thermalization rate, radius, temperature and prestrain is explored and investigated.

Contents

1	Introduction	1
1.1	Graphene electromechanical coupling	1
1.2	Graphene resonators	8
2	Simulation Methodology	10
2.1	Molecular dynamics simulation	10
2.2	Strain calculation in deformed graphene	12
2.2.1	Displacement approach	12
2.2.2	Stress approach	14
2.2.3	Benchmark examples	15
2.3	Pseudomagnetic fields in deformed graphene	16
2.4	Coupled mode equations in graphene resonator	21
2.5	Metastable states in FPU problem	24
3	Graphene Hexagon: In-Plane Deformation and Electromechanical Coupling	27
3.1	PMF distribution	31
3.2	Quantum transport	32
3.3	Valley splitting	35
3.4	Asymmetry, disorder and lattice orientation	37
3.4.1	Deformed hexagons under strain	38
3.4.2	Armchair Y-junction	39
3.4.3	Profile of B_s and LDOS (ZZ junction)	41

3.4.4	Profile of B_s and LDOS (AC junction)	44
3.4.5	Edge roughness and asymmetric strain	44
3.4.6	B_s as a barrier	48
4	Graphene Bubble: Three Dimensional Deformation and Electromechanical Coupling	50
4.1	Simulation setup	50
4.2	Clamped graphene nanobubbles	55
4.3	Substrate interaction: Graphene on Au (111)	63
4.4	Substrate interaction: Graphene on Cu (111)	69
4.5	Bending effects	73
5	Graphene Kirigami	79
5.1	Simulation setup	79
5.2	Numerical results	81
6	Mode Coupling in Graphene Nanoresonator	93
6.1	Simulation setup	93
6.2	Results and discussion	94
7	Future Work	102
8	Conclusions	104
	References	107
	Curriculum Vitae	120

List of Tables

5.1	Young's Modulus (E), Toughness (U_T) and Fracture Strength (σ_{frac})	90
-----	--	----

List of Figures

1·1	Graphene is a 2D building block for 0D buckyballs (left), 1D nanotubes (middle) and 3D graphite (right). Figure from Geim and Novoselov (Geim and Novoselov, 2007).	2
2·1	ϵ_{xx} distribution by displacement approach for uniaxial stretching case with 10% strain.	17
2·2	ϵ_{xx} distribution by stress approach for uniaxial stretching case with 10% strain.	17
2·3	ϵ_{xy} distribution by displacement approach for simple shear case with 1% strain.	17
2·4	ϵ_{xy} distribution by stress approach for simple shear case with 1% strain.	17
2·5	Schematic image of the simulated structure.	24
2·6	Visualization of the nonlinear mode coupling to the fundamental mode. The axes provide the mode number combinations. The coupling generally increases with mode number.	24
2·7	Mode energy distribution during the metastable state. The lowest four modes were initialized with equal energy. The energy is exponentially localized in mode space, with an increasing localization length with energy. Blue squares correspond to total energy $E = 5 \cdot 10^{-5}$, black circles to $E = 10^{-4}$ and green diamonds to $E = 2$. The mode energies are normalized to the energy of the fundamental mode.	26

3.1	Real-space distribution of the PMF B_s (Tesla) under $\epsilon_{\text{eff}} = 15\%$ obtained by mapping the tight-binding-derived LDOS at each atom. Inset: diagram of the tri-axial loading and contact scheme. $L \simeq 8$ nm.	28
3.2	(a) LDOS at two representative neighboring sites (Fig. 3.1) for $\epsilon_{\text{eff}} = 15\%$. (b) Peak positions vs $\text{sgn}(n)\sqrt{ n }$, extracted from spectra such as (a), and for different ϵ_{eff} . Straight lines are fits to Eq. 2.13 from which the local B_s can be extracted at the site where the LDOS was sampled.	28
3.3	Dependence of B_s^{max} on ϵ_{eff} obtained by the tight binding and displacement approaches discussed in the text.	29
3.4	(a) Transmission coefficient $T_{21}(T_{31})$ vs E_F for $\epsilon_{\text{eff}} = 0$ and 10%. The inset shows a close-up of the total DOS of the strained dot in the low energy region. A LDOS map (white is zero) of selected transmission resonances for $\epsilon_{\text{eff}} = 10\%$ is shown in (b) for $E = 0.018t_0$, and (c) for $E = 0.16t_0$. (d) A transverse section of (b) along the vertical direction through the center of the hexagon, showing the profile of the LDOS and the PMF (“displacement approach”). \tilde{R} marks the distance to the center.	30
3.5	(a) Detail of the splitting in the T_{21} resonances under an external field B_{ext} , for $\epsilon_{\text{eff}} = 10\%$. (b) Eigenenergies of the same hexagon vs B_{ext} , when disconnected from the contacts. (c) Likewise, but for $\epsilon_{\text{eff}} = 0$, where LL condensation (Lent, 1991) is more clearly observed. In (b) and (c) straight lines mark the lowest LLs in the infinite system, and the large range of B_{ext} used in the horizontal axes is to accommodate the very large PMF induced by strain.	35

3·6	(a) Hexagon (0% strain) with ZZ edges. The arrows are a schematic representation of the symmetrically applied tri-axial strain. In the transport calculations the contacts are attached to the edges under traction as well because the edge atoms are held fixed along the direction transverse to the tension, which allows us to keep the metallic contacts undeformed. (b) Deformed hexagon with ZZ edges after 10% of symmetric strain. (c) Deformed hexagon with ZZ edges after 15% of asymmetric (ramp) strain. (d) Hexagon (0% strain) with AC edges. The arrows are a schematic representation of the asymmetrical (ramp) strain setup. (e) Deformed hexagon with AC edges under 15% of symmetric strain. (f) Deformed hexagon with AC edges under 15% of asymmetric (ramp) strain.	38
3·7	(a) Transmission coefficient $T_{21}(T_{31})$ vs Fermi Energy for a symmetrically strained AC Y-junction. (b) LDOS mapping at $E = 0.043t_0$ for the 15% symmetrically strained AC Y-junction.	39
3·8	Sections of B_s and LDOS for a strained ZZ Y-junction with $\epsilon_{\text{eff}} = 10\%$. Panel (a) shows a density plot of B_s in the entire system obtained with the “displacement approach”. In panels (b)-(d) the profile of B_s (black) and LDOS (red) at $E = 0.018t_0$ were plotted along the directions defined in the text: $\theta = \pi/2$, $\theta = \pi/6$, and $\theta = -\pi/6$, respectively. . .	41
3·9	Sections of B_s and LDOS for a strained AC Y-junction with $\epsilon_{\text{eff}} = 15\%$. Panel (a) shows a density plot of B_s in the entire system obtained with the “displacement approach”. In panels (b)-(d) the profile of B_s (black) and LDOS (red) at $E = 0.043t_0$ were plotted along the directions defined in the text: $\theta = \pi/2$, $\theta = \pi/6$, and $\theta = -\pi/6$, respectively. . .	42

3·10	Transmission coefficient for: (a) 10% strained ZZ Y-junction with and without edge disorder; (b) 15% strained AC Y-junction with and without edge disorder; (c) 15% asymmetrically strained ZZ Y-junction; (d) 15% asymmetrically strained ZZ Y-junction with edge disorder. In panels (e) and (f) the distribution of B_s was displayed generated by the asymmetric traction illustrated in Fig. 3·6(d) for the case of, respectively, the ZZ and AC edged hexagon nanostructures considered in this work.	45
3·11	Current density mapping in real space for selected transmission features discussed above: (a) $E = 0.126t_0$ for the symmetric ZZ Y-junction with $\epsilon_{\text{eff}} = 10\%$; (b) for the asymmetrically strained ZZ Y-junction with $\epsilon_{\text{eff}} = 15\%$ at $E = 0.1t_0$; (c) at $E = 0.033t_0$ for the symmetric AC Y-junction with $\epsilon_{\text{eff}} = 15\%$; (d) for the asymmetrically strained AC Y-junction at $E = 0.095t_0$. In all plots, the length of the arrow is proportional to the value of the density current in that point.	47
4·1	Illustration of the strategy employed in the studies to generate nanobubbles by pressurizing graphene through a predefined substrate aperture. The picture shows one of the actual simulation cells used in MD computations. In gold, gray and red colors are represented, respectively, the Au substrate, the graphene sheet and the Ar atoms. A hole is carved in the Au substrate (perimeter outlined), and its perimeter geometry determines the shape of the resulting graphene bubble. Visualization is performed using VMD (Humphrey et al., 1996).	51

4.2 Results for a circular graphene bubble with 4 nm radius and pressurized up to ~ 1 nm deflection; in this case graphene was clamped at the edge of the substrate aperture. (a) Radial strain, (b) tangential strain, (c) PMF by TB method with both in-plane and bending components, (d) PMF arising from Hencky’s analytic model (Fichter, 1997) with the axes scaled in units of the circle radius, (e) PMF by TB method with in-plane component only, (f) PMF by displacement method. Note that, except for (d), all the panels refer to the same atomistic configuration. PMF shown in units of Tesla. The edge of the substrate aperture used in the MD simulation is outlined (gray line) for reference. 53

4.3 Angular-averaged amplitude of the PMF for the same cases presented in Fig. 4.2 in the form of density plots. The horizontal axis represents the distance from the center of a pressurized circular graphene nanobubble with clamped boundary conditions. The data contained here is the same shown in Fig. 4.4(a), except that here the (orange) data corresponding to the PMF obtained from the full hopping perturbation [Eq. 2.7] is included for comparison as well. The bending effects are clearly dominant around the edge/clamping region. Away from the edge, and inside, the three numerical curves follow Hencky’s model. 54

- 4.4 (a) Angular-averaged values of $B/\sin(3\theta)$ for the circular nanobubble with $R = 4\text{ nm}$ considered in Fig. 4.2. The different datasets correspond to different strategies discussed above to obtain the PMF. The vertical line at $r = R \approx 40\text{ \AA}$ marks the radius of the circular aperture in the substrate. For $r < R$ the results extracted from MD closely follow the analytical curve, but there is a sharp sign change and increase at $r \approx R$ (see 4.1 for details of the averaging procedure, as well as for the TB data including the full hopping perturbation). (b) Comparison between the pressure-induced deflection and maximum PMF magnitude at the edge, $|B(R \approx 40\text{ \AA})|$, obtained with the different approximations discussed in the text. The points corresponding to the complete TB hopping are scaled by 0.1 for better visualization. (c) A section of the simulated nanobubble (MD) at $\sim 19\text{ kBar}$ and the corresponding Hencky's solution (the inset shows a 3D perspective of the former with the color scale reflecting the vertical displacement). . . . 58
- 4.5 Top views of PMF patterns for graphene bubbles of different geometries without substrate. (a) circle (b) hexagon (c) pentagon (d) rectangle (aspect ratio 1:2) (e) square (f) triangle. All the bubble areas are $\sim 50\text{ nm}^2$, and side lengths and pressures can be found in the text. In all cases, the graphene lattice is oriented with the zigzag direction along the horizontal. The same color scale (in Tesla) is used in all panels. The edge of the substrate apertures used in the MD simulations is outlined (gray line) for reference. 61

4·6	<p>(a) Strain components ϵ_{rr} and $\epsilon_{\theta\theta}$ of a graphene bubble pressurized to a deflection of ~ 1 nm against a circular hole with 4 nm radius on a Au(111) substrate. (b) The corresponding PMF along the radial direction from the bubble center computed according to the extended Hencky model (Kitt et al., 2013a) (solid line) and from MD simulations within the TB (blue) or displacement (red) approach. Panel (d) shows the angular dependence of the PMF for selected radii.</p>	64
4·7	<p>Top views of PMF patterns for graphene bubbles of different geometries on Au(111) substrates. (a) circle (b) hexagon (c) pentagon (d) rectangle (aspect ratio 1:2) (e) square (f) triangle. All the bubble areas are ~ 50 nm², and side lengths and pressures can be found in the text. In all cases, the graphene lattice is oriented with the zigzag direction along the horizontal. The same color scale (in Tesla) is used in all panels. The edge of the substrate apertures used in the MD simulations is outlined (gray line) for reference.</p>	66
4·8	<p>Spatial patterns of the strain tensor components ϵ_{rr} and $\epsilon_{\theta\theta}$ for a triangular bubble with a 10.6 nm side. (a) and (b) pertain to graphene on a Au(111) substrate whose PMF profile has been shown in Fig. 4·5(f), while (c) and (d) correspond to the graphene bubble with an artificially fixed boundary condition whose PMF is shown in Fig. 4·7(f). The edge of the substrate aperture used in the MD simulation is outlined (gray line) for reference.</p>	67

4.9	Top views of PMF patterns for graphene bubbles of different geometries on Cu (111) substrate. (a) circle (b) hexagon (c) pentagon (d) rectangle (aspect ratio 1:2) (e) square (f) triangle. All the bubble areas are $\sim 50 \text{ nm}^2$, and side lengths and pressures can be found in the text. In all cases, the graphene lattice is oriented with the zigzag direction along the horizontal. The same color scale (in Tesla) is used in all panels. The edge of the substrate apertures used in the MD simulations is outlined (gray line) for reference.	70
4.10	PMF distributions of graphene on perfect (a) Cu (111) substrate and (b) Au (111) substrate without apertures nor gas pressure. The superlattice structure arises naturally from the need of the system to release strain buildup because of the mismatch in the lattice parameters of graphene and the underlying substrate. The PMF scale is in units of Tesla.	72
4.11	Density plot of the bending contribution to the pseudomagnetic field, $B^{(c)}$, for a circular graphene bubble with radius of 4 nm and a deflection of $\sim 1 \text{ nm}$ calculated by the TB method (a) and Hencky's model (b). The axes in (b) are scaled in units of the circle radius. The PMF scale is in units of Tesla. The edge of the substrate aperture used in the MD simulation is outlined (gray line) for reference.	74
4.12	Ratio of the maximum PMF induced by bending and stretching (B_c/B_{xy}) for circular graphene bubbles as a function of the graphene radius R , according to Hencky's solution.	75

4.13	Density plot of the bending contribution to the pseudomagnetic field, $B^{(c)}$, for a graphene bubble deflected to ~ 1 nm upon pressuring through a circular aperture of radius 4 nm in a Au (a) and a Cu (b) substrate. The PMF scale is in units of Tesla. The edge of the substrate apertures used in the MD simulations is outlined (gray line) for reference. . . .	77
5.1	Schematic of the graphene kirigami, with key geometric parameters labeled. The kirigami is deformed via tensile displacement loading that is applied at the two ends in the direction indicated by the arrows.	80
5.2	Left column: snapshots of the top view (a1-a4) illustrating the deformation stages for zigzag graphene kirigami. A representative yield region is marked in (a3). The tensile strains corresponding to the different stages are 14%, 29%, 56% and 65% respectively. Right column: schematic top view pictures (b1-b3) of similarly patterned paper kirigami for comparison. (b1-b3) correspond to (a1-a3) while paper kirigami fracture picture is not shown. Graphene figures were generated by VMD (Humphrey et al., 1996). <i>All snapshots were scaled for purposes of simplicity of visualization.</i>	81
5.3	Stress-strain curve of the representative graphene kirigami as shown in Fig. 5.2, where the 2D stress was calculated as stress σ times thickness t . Green, blue, orange and red regions correspond to the four stages of deformation discussed in the text and illustrated in Fig. 5.2. A stress-strain curve of a pristine zigzag graphene nanoribbon with the same width is shown in the inset for comparison.	82
5.4	(a) α validation with varying w and b , all cases were zigzag with constant $\alpha = 0.074$. (b) β validation with varying d and c , all cases were zigzag with constant $\beta = 0.052$, $L_0 = 115\text{\AA}$	84

5.5	Yield strain as a function of interior (N) and edge (M) cut pairs, demonstrating that the choice of 7 interior and 6 edge cut pairs used in this work is representative of the kirigami deformation within the limits of computational capabilities.	85
5.6	Influence of α on yield strain and fracture strain for zigzag and armchair graphene kirigami, for constant $\beta = 0.057$. Data are normalized by graphene nanoribbon results with the same width.	86
5.7	Influence of α on the kirigami yield stress, for constant $\beta = 0.057$. Data are normalized by graphene nanoribbon results with the same width.	87
5.8	Von Mises stress distribution of zigzag graphene kirigami corresponding to the snapshots in Fig. 5.2(a3), where the data was scaled between 0 to 1. Figure was generated by AtomEye (Li, 2003).	87
5.9	Influence of β on fracture strain and yield strain, for constant $\alpha = 0.07$. Data are normalized by graphene nanoribbon results with the same width.	89
5.10	(a) Original and (b) deformed ($\epsilon = 0.24$) configuration top-view snapshots of double Y-unit graphene kirigami structures. The geometry parameters are same as the text, Fig. 1, but with twice the width. Figure was generated by VMD (Humphrey et al., 1996). <i>The snapshots were scaled to same length for visualization purposes.</i>	91
5.11	Pseudomagnetic field distribution for zigzag graphene kirigami at $\epsilon \sim 0.17$ (i.e. before yield) with $L_0 \sim 340\text{\AA}$, $b \sim 100\text{\AA}$, $\alpha \sim 0.008$, $\beta \sim 0.06$	92

6.1	Time evolution of the energy spectral density of a circular graphene sheet obtained by MD simulations for the out-of-plane motion. Parameters are given in the text. Note the decay of the FM energy which is indicated by the filled area under the curve, as well as the shift in the FM frequency. The dashed black line is the FM frequency as estimated from the CM model. The inset shows the evolution of the individual mode energies obtained from the CM model in logarithmic scale. . . .	95
6.2	(a) Fundamental mode frequency as a function of mode energy. Symbols correspond to MD results, while the full line is the curve predicted from CM. The finite length of the time window used to calculate the frequency spectrum limits the frequency resolution. This is represented by the size of the symbols. (b) Simulation of Eq. 6.1 for a fixed total energy, but with varying initial FM energy. By shifting time, the curves align. The solid line is a fitted sigmoid function used to extract the transition time τ_{tr} . (c) Extracted rates $\Gamma = \tau_{tr}^{-1}$ from MD simulations (filled symbols) and CM (open symbols) for fixed initial value of $\eta = 1/2$ and varying total energy, reported as a function of the effective temperature T^* for fixed $\epsilon_{pre} = 0.2 \%$ according to Eq. 6.3. The dashed line corresponds to a linear scaling with T^*	97
6.3	Dependence of the metastable lifetime τ_m on system energy, for the CM model with 32 modes (triangles) and 40 modes (squares). The lines corresponds to stretched exponentials of the form $\tau_m \approx \exp(\tilde{E}^{-\alpha})$. The dashed line corresponds to $\alpha = 0.18$, the dotted corresponds to $\alpha = 0.25$	101

List of Abbreviations

AC	Armchair
AIREBO	Adaptive Intermolecular Reactive Empirical Bond Order
CM	Continuum Mechanics
CVD	Chemical Vapor Deposition
DFT	Density Functional Theory
DOS	Density of States
FCC	Face-Centered Cubic
FM	Fundamental Mode
FPU	Fermi, Pasta and Ulam
KdV	Korteweg-de Vries
LAMMPS	Large-scale Atomic/Molecular Massively Parallel Simulator
LDOS	Local Density of States
LL	Landau Level
MD	Molecular Dynamics
MEMS	Microelectromechanical System
MM	Molecular Mechanics
NEGF	Non-Equilibrium Green's function
NEMS	Nanoelectromechanical System
PMF	Pseudomagnetic Field
Q-factor	Quality Factor
TB	Tight Binding
TMD	Transition Metal Dichalcogenide
TRS	Time-Reversal Symmetry
ZZ	Zigzag

Chapter 1

Introduction

1.1 Graphene electromechanical coupling

The discovery of new materials is a significant driving force for technological innovation. Therefore, the discovery of *Graphene* in 2004 (Novoselov et al., 2004), a novel two dimensional (2D) material, initiated a huge wave of both fundamental scientific and technological efforts around the world (Geim, 2009). Graphene is a 2D allotrope of carbon with a honeycomb lattice structure (Fig. 1-1), first studied in 1947 (Wallace, 1947). However, the pure 2D structure was not believed to be possible until graphene was experimentally obtained by the famous Scotch Tape method (Novoselov et al., 2004). Afterwards, researchers soon found a variety of unique properties of graphene by theory, simulation and experiment: massless Dirac fermions at low energy (Novoselov et al., 2005; Castro Neto et al., 2009), Quantum Hall Effect (Zhang et al., 2005; Castro Neto et al., 2009), record high Young's modulus ($\sim 1\text{TPa}$) (Lee et al., 2008), extremely high electron mobility ($15,000\text{cm}^2 \cdot \text{V}^{-1} \cdot \text{s}^{-1}$) at room temperature (Geim and Novoselov, 2007; Bolotin et al., 2008), high opacity (Nair et al., 2008) and excellent thermal conductivity ($5,000\text{W} \cdot \text{m}^{-1} \cdot \text{K}^{-1}$) (Balandin et al., 2008), to name just a few. Among all those interesting and fantastic properties, this work focuses on the mechanical and electronic properties and in particular the mechanical-electronic coupling of graphene.

Graphene has attracted intense attention not only for its unusual physical properties (Geim and Novoselov, 2007; Castro Neto et al., 2009; Han et al., 2007; Seol et al.,

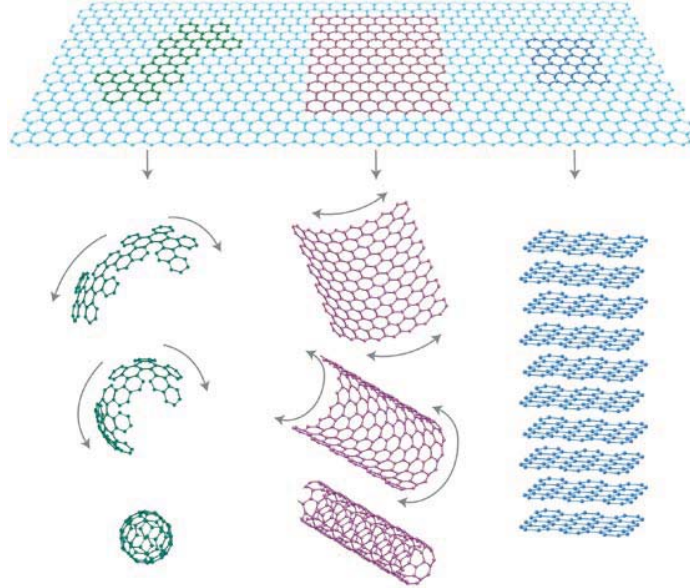


Figure 1.1: Graphene is a 2D building block for 0D buckyballs (left), 1D nanotubes (middle) and 3D graphite (right). Figure from Geim and Novoselov (Geim and Novoselov, 2007).

2010), but also for its potential as the basic building block for a wealth of device applications. However, there exist key limitations that appear to restrict the application of graphene for all-carbon electronic circuits: one such limitation is that graphene, in its pristine form, is well known to be a semi-metal with no band gap (Castro Neto et al., 2009). A highly active field of study has recently emerged based on the idea of applying mechanical strain to modify the intrinsic response of electrons to external fields in graphene (Guinea et al., 2010b; Qi et al., 2013; Tomori et al., 2011). This includes the strain-induced generation of spectral (band) gaps and transport gaps, which suppress conduction at small densities. Endowed with the strongest covalent bonding in nature, graphene exhibits the largest Young’s modulus ever registered ($E \simeq 1$ TPa), and a record range of elastic deformation for a crystal, which can be as high as 15-20% (Lee et al., 2008; Cadelano et al., 2009). Such outstanding mechanical characteristics are complemented by an unusual coupling of lattice deformations to the electronic motion, that can be captured by the concept of a pseudomagnetic field

(PMF) arising as a result of non-uniform local changes in the electronic hopping amplitudes (Kane and Mele, 1997; Suzuura and Ando, 2002; Castro Neto et al., 2009). In this context, several groups (Guinea et al., 2010a; Pereira and Castro Neto, 2009; Guinea and Low, 2010; Guinea et al., 2008; Abedpour et al., 2011; Guinea et al., 2010b; Kim et al., 2011; Yeh et al., 2011; Yang, 2011; Kitt et al., 2012; Kitt et al., 2013b; Yue et al., 2012) have employed continuum mechanics coupled with effective models of the electronic dynamics to study the generation of pseudomagnetic fields (PMFs) in different graphene geometries and subject to different deformations. The potential impact of strain engineering beyond the generation of bandgaps has also attracted tremendous interest (Pereira and Castro Neto, 2009; Pereira et al., 2010a; Abanin and Pesin, 2012; Wang et al., 2011).

However, a previous study (Pereira et al., 2009) showed that a band gap will not emerge under simple uniaxial strain unless the strain is larger than roughly 20%. This theoretical prediction, based on an effective tight-binding (TB) model for the electronic structure, has been subsequently confirmed by various more elaborate *ab-initio* calculations (Ni et al., 2009; Farjam and Rafii-Tabar, 2009; Choi et al., 2010). The robustness of the gapless state arises because simple deformations of the lattice lead only to local changes of the *position* of the Dirac point with respect to the undeformed lattice configuration (Kane and Mele, 1997; Suzuura and Ando, 2002) and to anisotropies in the Fermi surface and Fermi velocity (Pereira et al., 2010b). The shift in the position of the Dirac point is captured, in the low-energy, two-valley, Dirac approximation, by a so-called pseudomagnetic vector potential and resulting pseudomagnetic field (PMF) that arises from the strain-induced perturbation of the tight-binding hoppings (Suzuura and Ando, 2002). As a result, electrons react to mechanical deformations in a way that is analogous to their behavior under a real external magnetic field, except that overall time-reversal symmetry is preserved, since

the PMF has opposite signs in the two time-reversal related valleys (Castro Neto et al., 2009). Consequently, the ability to manipulate the strain distribution in graphene opens the enticing prospect of strain-engineering its electronic and optical properties, as well as of enhancing interaction and correlation effects (Guinea et al., 2010b; Pereira and Castro Neto, 2009; Pereira et al., 2010b; Pellegrino et al., 2010; Abanin and Pesin, 2012; Sharma et al., 2013).

The recent experimental confirmation that PMFs in excess of 300 T are possible with modest deformations in structures spanning only a few nm (Levy et al., 2010; Lu et al., 2012) brings this prospect of strongly impacting graphene's electronic properties by strain closer to fruition. Furthermore, a previous study (Guinea et al., 2010b) also found that nearly homogeneous PMFs could be generated in graphene through triaxial stretching, but the resulting fields were found to be moderate, unless relatively large (*i.e.*, $>10\%$) tensile strains could be applied. The ability to produce very large and fairly homogeneous PMFs within a few nm suggests the possibility of creating pseudomagnetic quantum dots, where confinement is driven by the PMF.

As a result, one of the objectives of this thesis is to undertake a theoretical study to probe the electronic and quantum transport properties of a representative graphene-based strained y-junction particularly suited to the generation of quasi-uniform PMFs (Guinea et al., 2010b). Despite this recent experimental evidence for strong PMF-induced Landau quantization, to the best of our knowledge, no measurements or calculations have been performed to assess the transport characteristics of such nanostructures. In this thesis, the quantum transport characteristics of such structures are assessed, revealing the Landau level- (LL) assisted character of the tunneling mechanism, as well as the interplay with an external field that breaks the valley degeneracy.

Though triaxial tension can generate quasi-uniform PMF in graphene, unfortu-

nately, such large planar tensile strains have not been experimentally realized in graphene to date. This is likely due to the record-high tensile modulus of graphene and the unavoidable difficulty in effectively transferring the required stresses from substrates to this monolayer crystal (Gong et al., 2010). It is thus remarkable that recent experiments report the detection of non-uniform strain distributions in bubble-like corrugations that generate PMFs locally homogeneous enough to allow the observation of Landau quantization by local tunneling spectroscopy. The magnitude of the PMFs reported from the measured Landau level spectrum reaches hundreds (300 to 600) of Teslas (Levy et al., 2010; Lu et al., 2012), providing a striking glimpse of the impact that local strain can potentially have on the electronic properties. A difficulty with these experiments is that, up to now, such structures have been seen and/or generated only in contact with the metallic substrates that are used in the synthesis of the sample. This is an obstacle, for example, to transport measurements, since this would require the transfer of the graphene sheet to another substrate, thereby destroying the favorable local strain distribution. In addition, a systematic study of different graphene bubble geometries and substrate types, which could reveal the subtleties that different geometries bring to the related strain-induced PMFs has not been reported. Furthermore, most previous studies of the interplay between strain and electronic structure in graphene have addressed the deformation problem from an analytic continuum mechanics point of view, with the exception of a few recent computational studies (Neek-Amal and Peeters, 2012b; Neek-Amal et al., 2012).

In this context, classical molecular dynamics (MD) simulations of strained graphene nanobubbles induced by gas pressure were conducted. The MD simulations are used to complement and compare continuum mechanics approaches to calculating strain, in order to examine the pressure-induced PMFs in ultra-small graphene nanobubbles of diameters on the order of 5 nm. Controlled synthesis of such small strained

nanobubbles has gained impetus following the recent experiments by Lu *et al.* (Lu et al., 2012). The aim is to use an unbiased calculation for the mechanical response of graphene at the atomistic level, on the basis of which one can (i) extract the relaxed lattice configurations without any assumptions; (ii) calculate the PMF distribution associated with different nanobubble geometries; (iii) discuss the influence of substrate and aperture shape on PMF distribution; (iv) identify conditions under which explicit consideration of the curvature is needed for a proper account of the PMFs.

In this thesis, the simulation methodology that was employed to determine the atomic displacements from which the strain tensor, modified electronic hopping amplitudes, and PMFs can be obtained is described. This is followed by numerical results of the strain-induced PMFs for different graphene nanobubble geometries in a simply clamped scenario. The considerable importance of the substrate interaction is discussed next and, then, the relative contributions of orbital bending and bond stretching to the total PMF is analyzed.

Recent experiments have shown that graphene nanobubbles smaller than 10 nm can be prepared on metallic substrates, and that large PMFs in the hundreds of Tesla result from the locally induced non-homogeneous strain (Levy et al., 2010; Lu et al., 2012). Because such small nanobubbles can be directly studied using classical MD simulations, MD is employed to obtain the deformed graphene bubble configurations due to an externally applied pressure. The atomistic potentials that describe the carbon-carbon interactions have been extensively investigated and, hence, graphene's nano-mechanics can be simulated without any particular bias, and to a large accuracy within MD. Once the deformation field is known from the simulations, the strain distribution in the inflated nanobubble is obtained, finally followed by a continuum gauge field approach to extract the resulting PMF distribution (Castro Neto et al., 2009; Guinea et al., 2010b; Guinea et al., 2010a; Guinea and Low, 2010; Guinea et al.,

2008; Abedpour et al., 2011).

While exhibiting high strength and stiffness, graphene's mechanical performance is hindered by its brittle nature, where under tensile loading graphene fractures immediately after yielding at strains generally not exceeding a few percent as found experimentally (Zhang et al., 2014; Lee et al., 2008), though the fracture strains obtained via simulation are much larger, and typically exceed 20% (Zhao et al., 2009; Zhao and Aluru, 2010; Lu et al., 2011; Liu et al., 2007). A key issue then for graphene is to not only develop techniques to enhance its ductility, but to do so in a systematic, tunable fashion. One example in this direction is the recent work of Zhu et al. (Zhu et al., 2014), who found that graphene nanomeshes can be stretched to nearly 50% strain. While the nanomeshes do enable substantial increases in mechanical stretchability, there is considerably greater opportunity to tailor the shapes and hence physical properties of graphene using the principles of kirigami, which is a version of origami in which cutting is used to change the morphology of a structure. Examples of the structural and geometric diversity that can be achieved using kirigami approaches for graphene have already been demonstrated experimentally (Blees et al., 2014).

One chapter in this thesis is devoted to the investigation of the mechanical properties, as well as the electromechanical coupling that is induced in graphene kirigami. Kirigami is a traditional Asian paper-cutting art (Temko and Takahama, 1978) and has been used for other smart designs in different scenarios (Xiaodong, 2007; Han et al., 2010; Sareh and Rossiter, 2013), while recently the rise of two-dimensional materials is generating another wave of studying Kirigami-like structures (Blees et al., 2014; Rose et al., 2014; Castle et al., 2014; Hou et al., 2014). In this work, Kirigami was applied to nanomaterials, specifically graphene, and the controllable mechanical response was investigated.

1.2 Graphene resonators

The second half of this work focuses on graphene nanoresonators. Graphene's high Young's modulus, low mass and 2D structure make it a wonderful candidate for resonator applications. Advances in fabrication techniques enable production and characterization of one and two dimensional nanoscale mechanical resonators (Bunch et al., 2007; Eriksson et al., 2008; Chen et al., 2009; Eichler et al., 2011). In particular, carbon-based resonators are considered to be promising for many applications due to their low mass and high quality factors (Q-factors) (Oshidari et al., 2012; Barton et al., 2011; van der Zande et al., 2010; Eom et al., 2011). It is also known that these systems display strongly nonlinear behavior (Atalaya et al., 2008; Eichler et al., 2011), which makes them interesting for investigations of nonlinear dynamics. The nonlinearities lead to a coupling between the vibrational modes (Matheny et al., 2013; Eriksson et al., 2013). This coupling allows for intermodal energy-transfer, which facilitates the redistribution of energy initially localized in a single mode.

In this respect, the mode-coupling provides a dissipation channel for the fundamental mode (FM) dynamics. In contrast to other dissipation mechanisms previously studied in nanomechanical resonators (Lifshitz and Roukes, 2000; Cross and Lifshitz, 2001; Wilson-Rae, 2008; Remus et al., 2009; Croy et al., 2012; Imboden and Mohanty, 2014), this is a fundamental intrinsic mechanism and therefore constitutes a lower limit on the relaxation rate of the FM. At finite temperatures, the effect of the mode couplings will be two-fold. First, they give rise to fluctuations in the resonator strain leading to dephasing or spectral broadening of the resonator (Barnard et al., 2012). Second, as shown in this work, they allow for energy redistribution among the modes. To distinguish the two effects, a ring-down setup was considered, where the total energy of the resonator is conserved and the evolution of the spectral distribution of energy is monitored. This allows us to access the dynamics of the FM

energy.

The process of thermalization in a system of nonlinearly coupled oscillators was originally considered by Fermi, Pasta and Ulam (FPU) in their famous computer experiment in 1955 (Fermi et al., 1955; Campbell et al., 2005), and spawned an impressive amount of research that eventually resulted in the development of chaos theory (Izrailev and Chirikov, 1966) and the discovery of solitons (Zabusky and Kruskal, 1965). For the FPU problem, it is known that above a certain critical energy density, energy initially fed into the FM is quickly redistributed among all modes, and the system approaches a thermal state. This threshold is connected to the onset of widespread chaos in the mode dynamics (Izrailev and Chirikov, 1966; Pettini et al., 2005) and the stability of localized modes (“q-breathers”) (Penati and Flach, 2007; Flach et al., 2005). In recent years, the consensus has been reached that the main features observed in the FPU problem are not specific to the original model Hamiltonian (Fucito et al., 1982; Bambusi and Ponno, 2008). A natural question, which is still under debate (Benettin et al., 2008), is whether those features can be observed in a physical system. For this to be possible two requirements need to be fulfilled: first, the nonlinearity has to be sufficiently strong to allow for appreciable coupling between resonator modes already at low energies. Second, the time-scale of energy dissipation to the environment must be long compared to that for thermalization due to the mode coupling. A chapter in this thesis is devoted to investigating the hypothesis that nanomembrane resonators can be used to test the persistence of the FPU phenomena in the thermodynamic limit.

Chapter 2

Simulation Methodology

Simulations at different length scales considering different physics require different simulation methods. To study the electro-mechanical coupling, molecular dynamics (MD) and molecular mechanics (MM) are used to calculate the mechanical deformation of graphene. A tight-binding (TB) model uses the deformed atomic positions from the MD or MM calculations to extract the PMF. Finally, the Landauer-Büttiker method is used to characterize the electron transport.

2.1 Molecular dynamics simulation

Computational methods for materials are developed for different length scales and material properties because the governing physics is distinct. The length scale covered in this thesis spans from nano to micro, and molecular dynamics simulation is a powerful technique for computational mechanics study. In 1957, MD was first introduced by Berni Alder for phase transition problems. Later on, researchers began using MD simulations for various studies in materials science, nanomechanics, chemistry, physics, biology, etc. Classical molecular dynamics is utilized here, and the word *classical* means particles in simulation obeys classical mechanics, or in another words Newton's laws. There are three important aspects in MD simulation: 1) Potential. The potential is to model the interaction between particles, and all electron interactions are lumped into the potential form. It usually takes an empirical description where the parameters are fitted from more accurate DFT calculations or experiments.

2) The time integrator. MD involves time integration during simulation, and integrators such as Verlet or Leapfrog are used for time iteration. 3) Ensemble. A statistical ensemble is necessary to control thermodynamic quantities like pressure, temperature and energy. Common ensembles include canonical ensemble (NVT), microcanonical ensemble (NVE) and isothermal-isobaric ensemble (NPT). MD has many advantages and is widely used nowadays for research in various fields. MD is capable of simulating many sophisticated systems with modern powerful clusters (Abraham et al., 2002; Buehler et al., 2004); however, it also has many well-known issues. The biggest issue is that the time step in MD simulations is small (Alder and Wainwright, 1959) (usually on the order of femtoseconds), and thus MD is not capable of simulating experimental time scales of seconds or longer (Tildesley and Allen, 1987; Frenkel and Smit, 2001). Furthermore, because the deformation in an MD simulation is achieved in a very short time frame, the resulting strain rate is often nearly 10 orders of magnitude larger than would be seen experimentally. (Yamakov et al., 2002; Wolf et al., 2005) Appropriate choice of strain rate can well describe the mechanical deformation of materials. (Kebblinski et al., 1998; Ikeda et al., 1999; Branício and Rino, 2000).

In this work, MD simulations were done with the Sandia-developed open source code LAMMPS (Lammps, 2012; Plimpton, 1995). Carbon-Carbon interactions were described by the AIREBO potential (Stuart et al., 2000) with a cutoff at 0.68 nm, which has been shown to capture accurately the mechanical properties of carbon-based nanostructures, including bond breaking, deformation, and various elastic moduli (Zhao et al., 2009; Wang and *et al.*, 2012; Qi et al., 2010). The Verlet integrator was used for time integration, and different ensembles were applied depending on the physical situation. Gas pressure was used to induce the deformation of graphene bubbles, which was modeled by stand 12-6 Lenard Jones potential.

2.2 Strain calculation in deformed graphene

One important output from the MD simulations is the computation of the PMF of deformed graphene structures, where the strain must be known to calculate the PMS. Derived from continuum mechanics theory, two different approaches were used to calculate strain field of graphene from the atomistic simulation results, which are introduced in the following sections.

2.2.1 Displacement approach

In continuum mechanics the infinitesimal strain tensor is written in Cartesian material coordinates (X_i) as: (U_i is displacement field)

$$\epsilon_{ij} = \frac{1}{2} \left(\frac{\partial u_i}{\partial X_j} + \frac{\partial u_j}{\partial X_i} \right) + \frac{1}{2} \left(\frac{\partial u_k}{\partial X_i} \frac{\partial u_k}{\partial X_j} \right). \quad (2.1)$$

To utilize Eq. 2.1, it is clear that the displacement field must be obtained such that its derivative can be evaluated to obtain the strain. In order to form a linear interpolation scheme using finite elements (Hughes, 1987), the geometry of the lattice was exploited and the results of MD simulation of the deformed graphene bubble were meshed using tetrahedral finite elements defined by the positions of four atoms: the atom of interest (with undeformed coordinates \mathbf{R}_0), and its three neighbors (with undeformed coordinates $\mathbf{R}_1, \mathbf{R}_2, \mathbf{R}_3$). After deformation, the new positions of the atoms are $\mathbf{r}_0, \mathbf{r}_1, \mathbf{r}_2$ and \mathbf{r}_3 , respectively. To remove spurious rigid body translation and rotation modes, the atom of interest (\mathbf{R}_0) was taken as the reference position, *i.e.*, $\mathbf{r}_0 = \mathbf{R}_0$. The displacement of its three neighbors could then be calculated, and subsequently the components of the strain tensor ϵ_{ij} were obtained by numerically evaluating the derivative of the displacement inside the element.

By subtracting the original position of each neighboring atom from its deformed position, the displacement vectors of the three nearest neighbors were obtained: $\mathbf{u}_{01} =$

$(u_{01x}, u_{01y}, u_{01z})$, $\mathbf{u}_{02} = (u_{02x}, u_{02y}, u_{02z})$, $\mathbf{u}_{03} = (u_{03x}, u_{03y}, u_{03z})$. Linear displacement field can be formulated from the four-node tetrahedral element as $\mathbf{U}(x, y, z) = (U_x, U_y, U_z)$ inside the tetrahedral element as: $U_x = a_1x + a_2y + a_3z$, $U_y = a_4x + a_5y + a_6z$, $U_z = a_7x + a_8y + a_9z$, where a_1 to a_9 are unknown constants for each tetrahedral element. Inserting the positions ($\mathbf{r}_1 = (x_1, y_1, z_1)$, $\mathbf{r}_2 = (x_2, y_2, z_2)$, $\mathbf{r}_3 = (x_3, y_3, z_3)$) and the corresponding displacements ($\mathbf{u}_{01}, \mathbf{u}_{02}, \mathbf{u}_{03}$) of the three neighboring atoms, a_1 to a_9 can be expressed in terms of \mathbf{r}_1 , \mathbf{r}_2 , \mathbf{r}_3 and \mathbf{u}_{01} , \mathbf{u}_{02} and \mathbf{u}_{03} , thus obtaining all coefficients of $\mathbf{U}(x, y, z)$. $\mathbf{U}(x, y, z)$ can be rearranged to express it in terms of \mathbf{u}_{01} , \mathbf{u}_{02} and \mathbf{u}_{03} in the following equation:

$$\begin{bmatrix} U_x \\ U_y \\ U_z \end{bmatrix} = \begin{bmatrix} N_1 & 0 & 0 & N_2 & 0 & 0 & N_3 & 0 & 0 \\ 0 & N_1 & 0 & 0 & N_2 & 0 & 0 & N_3 & 0 \\ 0 & 0 & N_1 & 0 & 0 & N_2 & 0 & 0 & N_3 \end{bmatrix} \begin{bmatrix} u_{01x} \\ u_{01y} \\ u_{01z} \\ u_{02x} \\ u_{02y} \\ u_{02z} \\ u_{03x} \\ u_{03y} \\ u_{03z} \end{bmatrix}, \quad (2.2)$$

where $N_i = N_i(x, y, z)$, $i = 1, 2, 3$ are the finite element shape functions. For simplicity, Eq. 2.2 can be rewritten as:

$$\mathbf{U} = \mathbf{N} \cdot \mathbf{u}_{\mathbf{N}}, \quad (2.3)$$

where $\mathbf{u}_{\mathbf{N}} = [\mathbf{u}_{01}, \mathbf{u}_{02}, \mathbf{u}_{03}]^T$ is the displacement field of the three neighboring atoms.

After obtaining the displacement field \mathbf{U} , the strain can be derived by differentiating Eq. 2.3 following the continuum strain as defined in Eq. 2.1 to give

$$\epsilon = \mathbf{T} \cdot \mathbf{u}_{\mathbf{N}}, \quad (2.4)$$

where $\mathbf{T} = \frac{\partial \mathbf{N}}{\partial \mathbf{x}}$ is constant inside each tetrahedral element.

2.2.2 Stress approach

In MD simulations, the atomic virial stress can be extracted on a per-atom basis. In the present work, the virial stress as calculated from LAMMPS (Thompson et al., 2009) was obtained for the strained graphene configuration. These stresses were then related to the strain via a linear constitutive relationship, as was done recently (Klimov et al., 2012). In the current work, a plane stress model was utilized for graphene, where the in-plane strains are written as $\epsilon_{xx} = \frac{1}{E}(\sigma_{xx} - \mu\sigma_{yy})$, $\epsilon_{yy} = \frac{1}{E}(\sigma_{yy} - \mu\sigma_{xx})$, $\epsilon_{xy} = \frac{\sigma_{xy}}{G}$. The material properties of graphene were chosen as $E = 1$ TPa (Huang et al., 2006), $G = 0.47$ TPa (Min and Aluru, 2011) and $\mu = 0.165$ (Blakslee et al., 1970), where E is the Young’s modulus, G the shear modulus, and μ Poisson’s ratio. It is important to note that, because a linear stress-strain relationship is assumed, the resulting strain is generally underestimated, particularly at large deformations due to the well-known nonlinear stress-strain response of graphene (Lee et al., 2008).

Both potential and kinetic parts were taken into account for virial stress calculation. Note that the virial stress calculated in LAMMPS is in units of “Pressure · Volume”, and thus the standard value of 3.42 \AA was used as the effective thickness of single layer graphene (Huang et al., 2006) to calculate the stress. A plane stress constitutive model was utilized to calculate the strain via

$$\begin{bmatrix} \epsilon_{xx} \\ \epsilon_{yy} \\ \epsilon_{xy} \end{bmatrix} = \begin{bmatrix} \frac{1}{E} & -\frac{\mu}{E} & 0 \\ -\frac{\mu}{E} & \frac{1}{E} & 0 \\ 0 & 0 & \frac{1}{2G} \end{bmatrix} \cdot \begin{bmatrix} \sigma_{xx} \\ \sigma_{yy} \\ \sigma_{xy} \end{bmatrix}, \quad (2.5)$$

2.2.3 Benchmark examples

The displacement and stress approaches were compared via two simple benchmark examples, those of uniaxial stretching and simple shear. For the uniaxial stretching case, $\epsilon_{xx} \approx 10\%$ strain was applied along the x-direction. The loading was done by applying a ramp displacement that went from zero in the middle of simulation box to a maximum value at the +x and -x edges of the graphene monolayers.

For the simple shear case, $\epsilon_{xy} \approx 1\%$ shear strain was applied by fixing the -x edge and displacing the +x edge in the y-direction. Both the uniaxial stretching and simple shear simulations were performed via MD simulations by LAMMPS (Lammps, 2012) code with the AIREBO potential (Stuart et al., 2000). The result for the uniaxial stretching is shown in Figs. 2.1 and Fig. 2.2, while the simple shear is shown in Figs. 2.3 and Fig. 2.4. The superior performance of the displacement approach is seen in both cases. Specifically, because a linear stress-strain relationship is assumed in the stress approach as shown in Eq. 2.5, the resulting strain is generally underestimated, particularly at large deformations due to the well-known nonlinear stress-strain response of graphene (Lee et al., 2008).

Once the strain distribution is determined from the MD simulations, the PMF, B , can be directly evaluated from the definitions above. However, if the strain tensor is calculated within the displacement approach, a second numerical derivative is needed to get B , which is likely to introduce a certain degree of error. Nevertheless the errors were found to be of acceptable magnitude.

Compared with the displacement approach, the stress approach avoids one numerical differentiation, but a constitutive approximation is involved. To compare the accuracy of the displacement and stress approaches, the PMF distribution in a circular bubble was calculated (for which an analytic solution is available and detailed analysis was recently performed (Kim et al., 2011)) by obtaining the strain via three

different methods: an analytic continuum mechanics model, *i.e.*, the Hencky solution (Fichter, 1997), the MD-based displacement approach and the MD-based stress approach. The PMFs generated from the MD-based displacement approach are in good agreement with those that follow from Hencky’s analytic solution, and also with previously reported values for a circular bubble (Kim et al., 2011). In contrast, the stress approach fails to yield reasonable results for this loading situation. Therefore, stress method is not used in this work.

2.3 Pseudomagnetic fields in deformed graphene

Non-zero PMFs arise from the non-uniform strain distribution in deformed graphene structure. These PMFs reflect the physical perturbation that the electrons near the Fermi energy in graphene feel as a result of the local changes in bond length. It emerges straightforwardly in the following manner. Nearly all low-energy electronic properties and phenomenology of graphene are captured by a simple single orbital nearest-neighbor tight-binding (TB) description of the π bands in graphene (Castro Neto et al., 2009). In second quantized form this tight-binding Hamiltonian reads

$$H = - \sum_{i, \mathbf{n}} t(\mathbf{r}_i, \mathbf{r}_i + \mathbf{n}) a_{\mathbf{r}_i}^\dagger b_{\mathbf{r}_i + \mathbf{n}} + \text{H. c.}, \quad (2.6)$$

where $t(\mathbf{r}_i, \mathbf{r}_i + \mathbf{n})$ represents the hopping integral between two neighboring π orbitals, \mathbf{n} runs over the three nearest unit cells, and $a_{\mathbf{r}_i}(b_{\mathbf{r}_i})$ are the destruction operators at the unit cell \mathbf{r}_i and sublattice $A(B)$. In the undeformed lattice the hopping integral is a constant: $t(\mathbf{r}_i, \mathbf{r}_i + \mathbf{n}) = t(\mathbf{R}_i, \mathbf{R}_i + \mathbf{n}) = t = 2.7 \text{ eV}$. The deformations of the graphene lattice caused by the gas pressure impact the hopping amplitudes in two main ways. One arises from the local stretch that generically tends to move atoms farther apart from each other and, consequently, directly affects the magnitude of the hopping t_{ij} between neighboring atoms i and j , which is exponentially sensitive

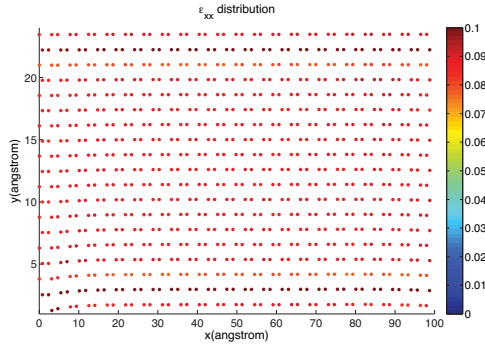


Figure 2.1: ϵ_{xx} distribution by displacement approach for uniaxial stretching case with 10 % strain.

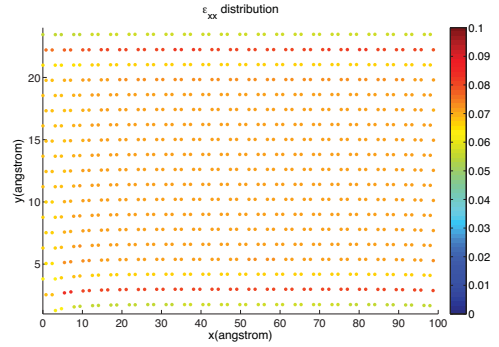


Figure 2.2: ϵ_{xx} distribution by stress approach for uniaxial stretching case with 10 % strain.

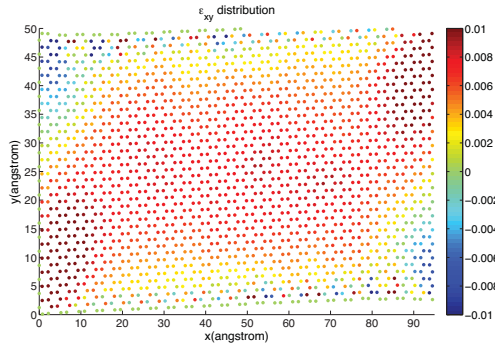


Figure 2.3: ϵ_{xy} distribution by displacement approach for simple shear case with 1 % strain.

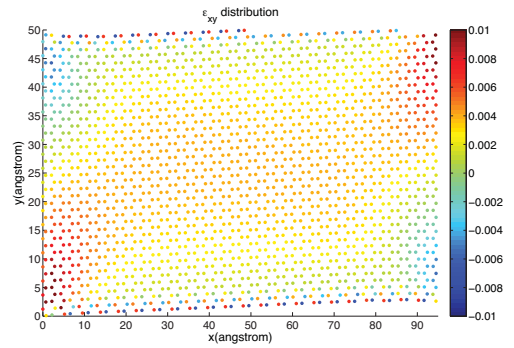


Figure 2.4: ϵ_{xy} distribution by stress approach for simple shear case with 1 % strain.

to the interatomic distance. The other effect is caused by the curvature induced by the out-of-plane deflection, which means that the hopping amplitude is no longer a purely $V_{pp\pi}$ overlap (in Slater-Koster notation) but a mixture of $V_{pp\pi}$ and $V_{pp\sigma}$. More precisely, one can straightforwardly show that the hopping between two p_z orbitals oriented along the unit vectors \mathbf{n}_i and \mathbf{n}_j and a distance \mathbf{d} apart is given by (Isacsson et al., 2008; Pereira et al., 2010a).

$$-t_{ij} = V_{pp\pi}(d) \mathbf{n}_i \cdot \mathbf{n}_j + \frac{V_{pp\sigma}(d) - V_{pp\pi}(d)}{d^2} (\mathbf{n}_i \cdot \mathbf{d})(\mathbf{n}_j \cdot \mathbf{d}). \quad (2.7)$$

To capture the exponential sensitivity of the overlap integrals to the interatomic distance d they were modeled by

$$V_{pp\pi}(d) = -t e^{-\beta(d/a-1)}, \quad (2.8a)$$

$$V_{pp\sigma}(d) = +1.7 t e^{-\beta(d/a-1)}, \quad (2.8b)$$

with $a \simeq 1.42 \text{ \AA}$ the equilibrium bond length in graphene. For static deformations a value $\beta \approx 3$ is seen to capture the distance dependence of $V_{pp\pi}(d)$ in agreement with first-principles calculations (Pereira et al., 2009; Pereira et al., 2010b); the same decay constant β is used for both overlaps, which is justified from a Mülliken perspective since the principal quantum numbers of the orbitals involved is the same (Hansson and Stafström, 2003). In the undeformed state Eq. 2.7 reduces to $-t_{ij} = V_{pp\pi}(a) \equiv -t$ and is, of course, constant in the entire system. But local lattice deformations cause $t(\mathbf{r}_i, \mathbf{r}_i + \mathbf{n})$ to fluctuate, which can be described by suggestively writing $t(\mathbf{r}_i, \mathbf{r}_i + \mathbf{n}) = t + \delta t(\mathbf{r}_i, \mathbf{r}_i + \mathbf{n})$. In the low energy (Dirac) approximation, the effective Hamiltonian around the point $\pm \mathbf{K}$ in the Brillouin zone can then be written as (Kane and Mele, 1997; Suzuura and Ando, 2002)

$$H_{\text{eff}}^{\pm \mathbf{K}} = v_F \boldsymbol{\sigma} \cdot (\mathbf{p} \mp q \mathbf{A}), \quad (2.9)$$

where $\hbar v_F = 3ta/2$, q represents the charge of the current carriers ($q > 0$ for holes and $q < 0$ for electrons), and the Cartesian components of the pseudomagnetic vector potential $\mathbf{A} = A_x \mathbf{e}_x + A_y \mathbf{e}_y$ are given explicitly in terms of the hopping perturbation by

$$A_x(\mathbf{R}) - iA_y(\mathbf{R}) = \frac{1}{qv_F} \sum_{\mathbf{n}} \delta t(\mathbf{r}, \mathbf{r} + \mathbf{n}) e^{i\mathbf{K} \cdot \mathbf{n}}. \quad (2.10)$$

For nearly planar deformations (small out-of-plane vs in-plane displacement ratios and thus neglecting bending effects) δt can be expanded in terms of the local displacement field and, consequently, can be cast in terms of the strain components. Orienting the lattice so that the zigzag (ZZ) direction is parallel to \mathbf{e}_x leads to

$$A_x(\mathbf{R}) - iA_y(\mathbf{R}) \simeq \frac{\hbar\beta}{2qa} (\epsilon_{xx} - \epsilon_{yy} + 2i\epsilon_{xy}), \quad (2.11)$$

Since ultimately the interest is the PMF, only the contributions to $\mathbf{A}(\mathbf{R})$ arising from the hopping modification are considered here, as they are the ones that survive after the curl operation (de Juan et al., 2013; Kitt et al., 2012; Kitt et al., 2013b; Sloan et al., 2013; Oliva-Leyva and Naumis, 2013); contributions beyond second order smallness are not considered ($\sim k\epsilon$, $\sim k^2$, etc.). In the planar strain situation the whole information about the electronic structure is reduced to the parameter $\beta = -\partial \log t(r) / \partial \log r|_{r=a}$. From the coupling in Eq. 2.9 where the effects of strain are captured by replacing $\mathbf{p} \rightarrow \mathbf{p} - q\mathbf{A}$ it is clear that the local strain is felt by the electrons in the \mathbf{K} valley in the same way as an external magnetic field would be. In particular, this effect can be quantified in terms of the PMF, which is defined as

$$B = \partial_x A_y(\mathbf{R}) - \partial_y A_x(\mathbf{R}). \quad (2.12)$$

From an operational perspective, B can be calculated directly from Eq. 2.10 by computing the hopping between all pairs of neighboring atoms in the deformed state, or from Eq. 2.11 by calculating the strain components throughout the entire system

as described in the previous section. The former strategy is here referred to as the *TB approach*, and the latter as the *displacement approach* and *stress approach*, as per the definitions in section 2.2.1 and 2.2.2. Another way to calculate strain is by the continuum Hencky model developed for clamped circular membrane with a large deflection (Fichter, 1997). There is also a third approach, namely *exact diagonalization*. Specifically, the relaxed atomic positions are used as input to the exact diagonalization of the π -band TB Hamiltonian for graphene, using the parametrization $V_{pp\pi}(l) = t_0 e^{-3.37(l/a-1)}$ to describe the dependence of this Slater-Koster parameter on the C-C distance l ($t_0 = 2.7$ eV and $a \simeq 0.142$ nm). This approximation was shown to describe with good accuracy both the threshold deformation for the Lifshitz band insulator transition at large deformations (Pereira et al., 2009; Ni et al., 2009), and the behavior of $V_{pp\pi}(l)$ or the optical conductivity when directly compared to *ab-initio* calculations (Ribeiro and *et al.*, 2009; Pereira et al., 2010b). Here electron-electron interactions are not considered. One property extracted from this procedure is the exact (within this TB model) local density of states (LDOS), from which the local PMF distribution can be mapped by fitting the resonant LDOS at each atom to the Landau level (LL) spectrum expected for graphene (McClure, 1956; Castro Neto et al., 2009):

$$E_n = \pm \hbar \omega_c \sqrt{n}, \quad \hbar^2 \omega_c^2 = 2e \hbar v_F^2 B_s, \quad \hbar v_F = 3ta/2. \quad (2.13)$$

The approaches used to calculate PMF are explicitly stated in following sections. There is a recent proposal to connect structure and electronic properties of two-dimensional crystals based on concepts from discrete geometry that allows yet another efficient alternative to obtain the strain and PMF at discrete lattice points without the need, for example, to perform numerical derivatives upon the displacement fields or vector potentials extracted from the MD data (Sloan et al., 2013; Pacheco Sanjuan

et al., 2014).

Once the strains for each atom are determined, the vector gauge field \mathbf{A} is straightforward to compute. However, to get the pseudomagnetic field, another derivative is needed (Eq. 2.12), calculated in a similar fashion as the strain is calculated from the displacement field. Thus, the displacement approach involves two numerical derivatives, but no approximation is made about material properties. The stress approach involves one numerical derivative, but linear elastic plane stress approximation is made for the material. The TB approach involves one numerical derivative, and at the same time no material properties are assumed. The exact diagonalization approach does not involve any numerical derivative, neither assumes any material properties, but the system size is limited due to the Hamiltonian diagonalization.

2.4 Coupled mode equations in graphene resonator

The dynamics of suspended graphene resonators are described within continuum mechanics by the Föppl-von Karmann equations (Atalaya et al., 2008). For the drum geometry (Fig. 2.5), they read (Eriksson et al., 2013)

$$\rho_G \ddot{u}_r - [\partial_r \sigma_{rr} + r^{-1} \partial_\phi \sigma_{r\phi} + r^{-1} (\sigma_{rr} - \sigma_{\phi\phi})] = 0, \quad (2.14a)$$

$$\rho_G \ddot{u}_\phi - [\partial_r \sigma_{r\phi} + 2r^{-1} \sigma_{r\phi} + r^{-1} \partial_\phi \sigma_{\phi\phi}] = 0, \quad (2.14b)$$

$$\rho_G \ddot{w} - \epsilon_{\text{pre}} (\lambda + 2\mu) r^{-1} \partial_r (r \partial_r w) - r^{-1} [\partial_r (r \sigma_{rr} \partial_r w + \sigma_{r\phi} \partial_\phi w) + \partial_\phi (\sigma_{r\phi} \partial_r w + r^{-1} \sigma_{\phi\phi} \partial_\phi w)] = 0, \quad (2.14c)$$

where u_r , u_ϕ and w are the radial, angular and out-of-plane displacement fields, σ_{ij} is the stress tensor, ρ_G is the mass density of graphene, ϵ_{pre} is the pre-strain of the sheet and λ and μ are the Lamé parameters of graphene. To derive the equation of

motion for the mode dynamics, the in-plane dynamics is first eliminated adiabatically by setting $\ddot{u}_r = 0$ and $\ddot{u}_\phi = 0$ and solve the remaining stationary equations for the in-plane fields. The equations are made dimensionless through the following scaled variables,

$$\tilde{r} = \frac{r}{R}; \quad \tilde{t} = \frac{\sqrt{\epsilon_{\text{pre}}} c_L}{R} t; \quad \tilde{w}^2 = \frac{1}{2} \frac{w^2}{R^2 \epsilon_{\text{pre}}}; \quad \tilde{E} = \frac{E}{2 \epsilon_{\text{pre}}^2 c_L^2 \rho_G R^2}, \quad (2.15)$$

where $c_L^2 = (\lambda + 2\mu)/\rho_G$ is the longitudinal speed of sound in graphene and R is the radius of the drum. In the following, only radially symmetric deformations are considered.

The dimensionless equations for the in- and out-of-plane components are, skipping the tildes over the scaled variables for convenience,

$$\left[u_{r,rr} + \frac{1}{r} u_{r,r} - \frac{1}{r^2} u_r \right] - \frac{1-\nu}{2} \frac{1}{r} w_{,r}^2 - \frac{1}{2} \partial_r w_{,r}^2 = 0, \quad (2.16a)$$

$$\ddot{w} - \left(\partial_r + \frac{1}{r} \right) \left(w_{,r} + \frac{w^3}{2} \right) - \left(\partial_r + \frac{1}{r} \right) u_{r,r} w_{,r} - \nu \frac{1}{r} \partial_r u_r w_{,r} = 0, \quad (2.16b)$$

with boundary conditions $w(1, t) = 0$, $u_r(1, t) = 0$. Subscript $,r$ denotes radial differentiation and ν is the Poisson ratio. The in-plane field is expanded as $u_r(r, t) = \sum_k Q_k(t) J_1(\xi_{1k} r)$ where ξ_{nk} is the k :th zero of the n :th Bessel function, $J_n(\xi_{nk}) = 0$. The amplitudes $Q_k(t)$ are given by

$$Q_k = \frac{J_2(\xi_{1k})^2}{2\xi_{1k}^2} C_k(t), \quad (2.17)$$

where

$$C_k(t) \equiv \int_0^1 dr r J_1(\xi_{1k} r) \left[\frac{1-\nu}{2r} w_{,r}^2 + \frac{1}{2} \partial_r w_{,r}^2 \right]. \quad (2.18)$$

Inserting this result into the equation for w , leads to

$$\ddot{w} - \left(\partial_r + \frac{1}{r} \right) \left(w_{,r} + \frac{w_{,r}^3}{2} \right) - \sum_k \frac{J_2(\xi_{1k})^2 C_k}{2\xi_{1k}^2} \left[\left(\partial_r + \frac{1}{r} \right) J_1'(\xi_{1k}r) w_{,r} + \frac{\nu}{r} \partial_r (J_1(\xi_{1k}r) w_{,r}) \right] = 0. \quad (2.19)$$

Next $w(r, t) = \sum_n q_n(t) J_0(\xi_{0n}r) \equiv \sum_n q_n(t) \phi_n(r)$ was expanded for brevity. The equation of motion then becomes

$$\frac{2}{J_1(\xi_{0n})^2} \ddot{q}_n + \frac{2}{J_1(\xi_{0n})^2} \xi_{0n}^2 q_n + \frac{1}{2} \sum_{k,l,m} M_{klmn} q_k q_l q_m - \sum_{k,l} \frac{J_2(\xi_{1k})^2 C_k}{2\xi_{1k}^2} K_{kln} q_l, \quad (2.20)$$

with

$$M_{klmn} = \int_0^1 dr r \phi_{k,r} \phi_{l,r} \phi_{m,r} \phi_{n,r}, \quad (2.21a)$$

$$K_{kln} = - \int_0^1 dr [r J_1'(\xi_{1,k}r) \phi_{n,r} \phi_{l,r} + \nu J_1(\xi_{1,k}r) \phi_{n,r} \phi_{l,r}]. \quad (2.21b)$$

Inserting the expansion of w into the definition of C_k leads to

$$C_k = \frac{1}{2} \sum_{ij} K_{kij} q_i q_j. \quad (2.22)$$

Consequently, the equation of motion for the out-of-plane motion becomes

$$\ddot{q}_n + \xi_{0n}^2 q_n + \sum_{i,j,m} W_{ij;mn} q_i q_j q_m = 0, \quad (2.23)$$

with

$$W_{ij;mn} = J_1(\xi_{0n})^2 \frac{1}{4} M_{ijmn} - J_1(\xi_{0n})^2 \frac{1}{4} \sum_k \frac{J_2(\xi_{1,k})^2}{2\xi_{1,k}^2} K_{kim} K_{kjn}. \quad (2.24)$$

being the effective coupling matrix, which enters Eq.(1). From the definition, it is clear that M_{ijmn} is symmetric in all indices. The second term in the definition of the coupling matrix is symmetric under $i \leftrightarrow j$ and $m \leftrightarrow n$, which is reflected in

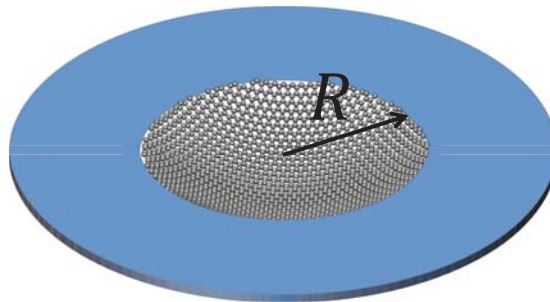


Figure 2.5: Schematic image of the simulated structure.

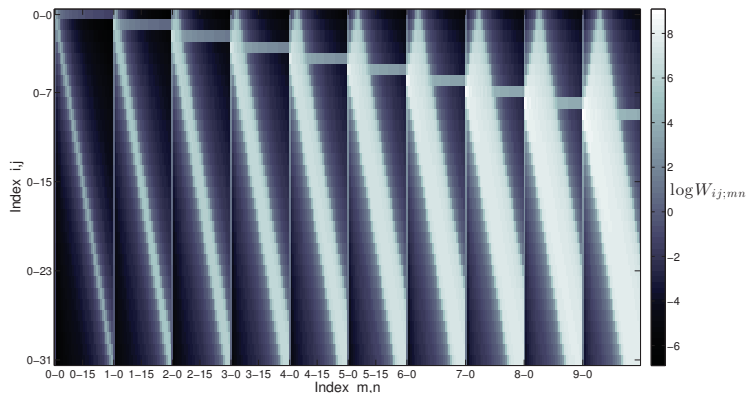


Figure 2.6: Visualization of the nonlinear mode coupling to the fundamental mode. The axes provide the mode number combinations. The coupling generally increases with mode number.

the notation $W_{ij;mn}$. An alternative derivation based on the Airy stress function is outlined in (Eriksson et al., 2013).

2.5 Metastable states in FPU problem

The dynamics of the fundamental mode is the interest of this thesis, hence the structure of the matrix can be visualized by fixing the first index to $i = 0$, and loop over the remaining indices, treating ij and mn as superindices. From Fig. 2.6, it is clear that the strength of the coupling as well as the density of modes to which the fundamental mode couples increases with mode number. One of the striking features of

the FPU problem is the existence of a long-lived metastable state far from equipartition. An initial understanding of the apparent lack of equipartition was based on the similarity of the FPU model to the Korteweg-de Vries (KdV) equation (Zabusky and Kruskal, 1965). The KdV equation is integrable, and the lack of equipartition was attributed to this fact. However, the metastability persists only for energies below a certain threshold. Above the threshold, the metastable state disappears and the system approaches equipartition on a relatively short time scale (Izrailev and Chirikov, 1966). The metastability is therefore not completely explained by the similarity of the FPU problem to the integrable KdV equation. A complementary approach to describe the metastable state was developed by Flach and coworkers (Flach et al., 2005), which focusses on the energy spectrum in mode space (q-space). For vanishing nonlinearity, any excitation consisting of only one mode is a periodic orbit. For nonzero nonlinearity, the orbit will spread out to nearby modes, constituting what is denoted a q-breather. These q-breathers are exponentially localized in mode space, and are obtained by treating the FPU system as a perturbation to a system of uncoupled harmonic oscillators. Consequently, the q-breather formalism applies to generic nonlinear lattices as long as a non-resonance condition is fulfilled and for sufficiently low energies. The exponential localization in mode space is present also in the system considered in this thesis, see Fig. 2.7. Here, the four lowest modes are initialized with equal energy simulated with 32 sites in continuum model. The localization length shows a clear dependence on the excitation energy, and in the limit of large energies the spectrum is essentially flat, signifying equipartition.

To study the intrinsic loss mechanisms in such systems, MD simulations were also performed to systematically investigate the free vibrations of pristine circular graphene monolayers with varying radius, prestrain, temperature and excitation energy. After an initial relaxation stage, the graphene monolayer was strained and

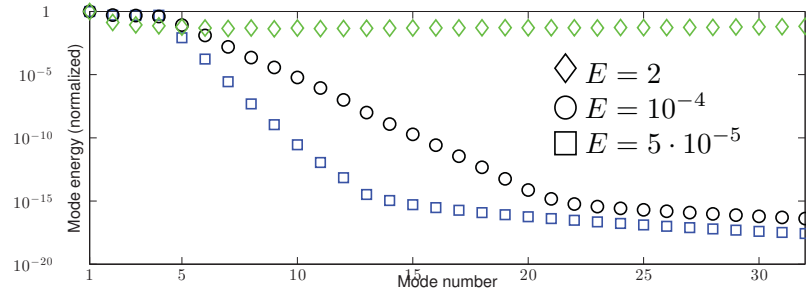


Figure 2.7: Mode energy distribution during the metastable state. The lowest four modes were initialized with equal energy. The energy is exponentially localized in mode space, with an increasing localization length with energy. Blue squares correspond to total energy $E = 5 \cdot 10^{-5}$, black circles to $E = 10^{-4}$ and green diamonds to $E = 2$. The mode energies are normalized to the energy of the fundamental mode.

system was equilibrated for 10 ps. Thereafter, the monolayer was actuated and allowed to vibrate freely for 5000 ps. More details can be found in section 6.1.

Chapter 3

Graphene Hexagon: In-Plane Deformation and Electromechanical Coupling

In order to capture the microscopic details as realistically as possible, a combined atomistic, electronic and transport calculation procedure is employed, which provides a set of unbiased results at all these levels. The microscopic configuration of each carbon atom is obtained by a fully relaxed Molecular Mechanics (MM) approach. Knowledge of the position of each atom allows us to extract the π -band bandstructure of the relaxed lattice via a tight-binding exact diagonalization approach, as well as to calculate the quantum transport properties across the structure via a non-equilibrium Green's function (NEGF) approach. In this way one unveils the local electronic structure, from which the local pseudo-magnetic fields and local current distribution can be extracted, without approximations, using a system of realistic dimensions with more than 6000 atoms.

The deformed configurations of an hexagonal graphene monolayer were obtained using standard MM simulations at 0 K. For definiteness, the system shown in Fig. 3-1 was focused on, with 6144 atoms, and a side length, $L = 7.87$ nm, but note that the results do not show variance among specific sizes and can be straightforwardly rescaled to larger or smaller dimensions. The lattice orientation is nevertheless important, and the one in Fig. 3-1 is chosen, which maximizes the magnitude of the PMF (Guinea et al., 2010b).

The system was triaxially stretched by in-plane displacement increments of 10^{-3} nm

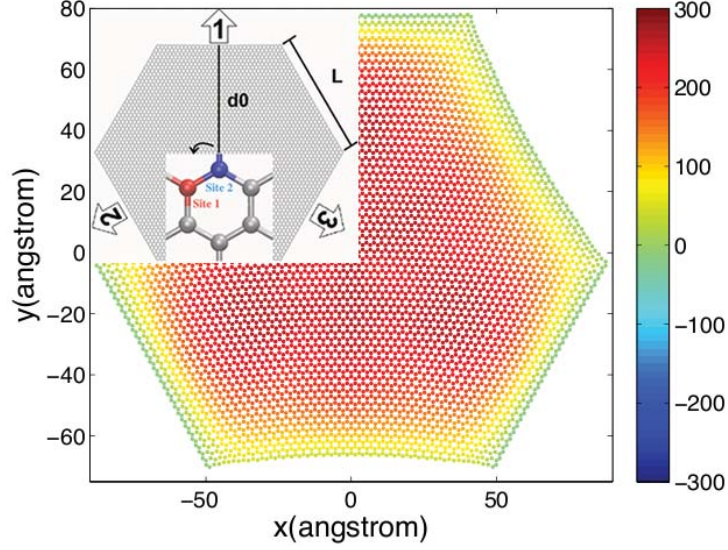


Figure 3-1: Real-space distribution of the PMF B_s (Tesla) under $\epsilon_{\text{eff}} = 15\%$ obtained by mapping the tight-binding-derived LDOS at each atom. Inset: diagram of the tri-axial loading and contact scheme. $L \simeq 8$ nm.

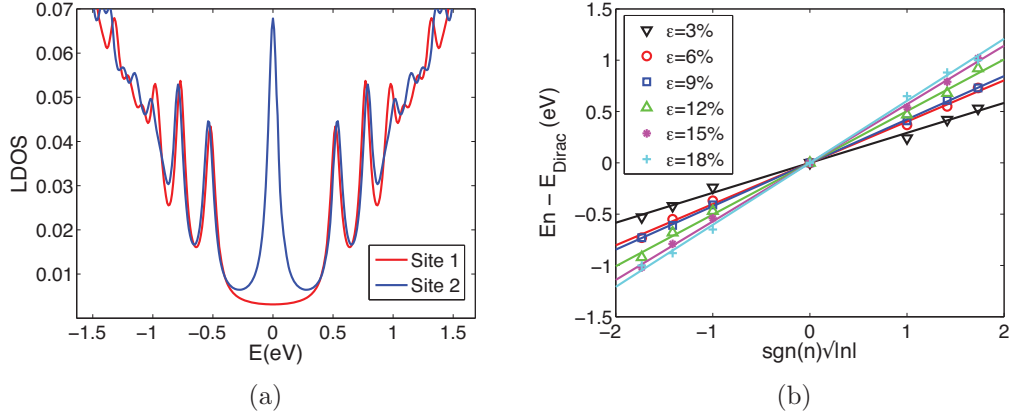


Figure 3-2: (a) LDOS at two representative neighboring sites (Fig. 3-1) for $\epsilon_{\text{eff}} = 15\%$. (b) Peak positions vs $\text{sgn}(n)\sqrt{|n|}$, extracted from spectra such as (a), and for different ϵ_{eff} . Straight lines are fits to Eq. 2.13 from which the local B_s can be extracted at the site where the LDOS was sampled.

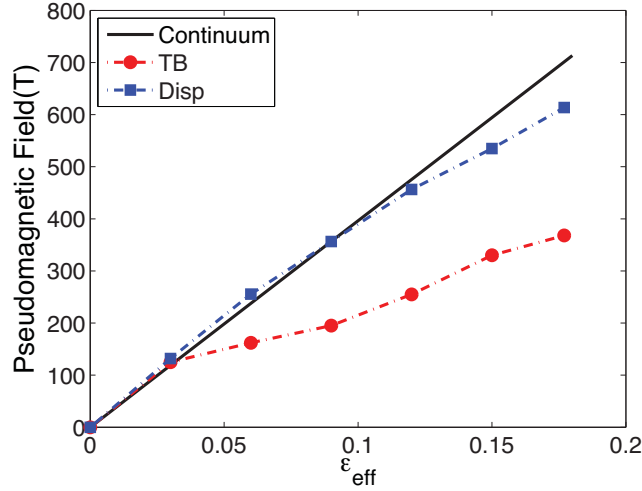


Figure 3.3: Dependence of B_s^{max} on ϵ_{eff} obtained by the tight binding and displacement approaches discussed in the text.

along each of the three arms shown in Fig. 3.1. Following each strain increment, graphene was allowed to relax according to the conjugate gradient algorithm, until relative changes in the system energy from one increment to the next were smaller than 10^{-7} . Since the strain thus generated is non-uniform, the nominal strain $\epsilon_{\text{eff}} = (d - d_0)/d_0$ is introduced, where $d_0(d)$ is the distance from the center to the edge of the hexagon before (after) stretching, as illustrated in Fig. 3.1. Nominal strains ranging from 0 to 18% are considered below. Once the relaxed configurations were obtained at each value of strain the atomic positions were used as the basis for electronic structure and quantum transport calculations. Here exact diagonalization approach was used to extract PMF from MM results.

An example of typical LDOS spectra is shown in Fig. 3.2(a). Eq. 2.13 was used to obtain the local B_s distribution throughout the system by fitting the slope of E_n vs \sqrt{n} seen in the numerical LDOS at various strains, as shown in Fig. 3.2(b). Notice that the $n = 0$ LL is absent in the LDOS of one of the sublattices, similarly to data recently reported in experiments with artificial honeycomb lattices (Gomes and

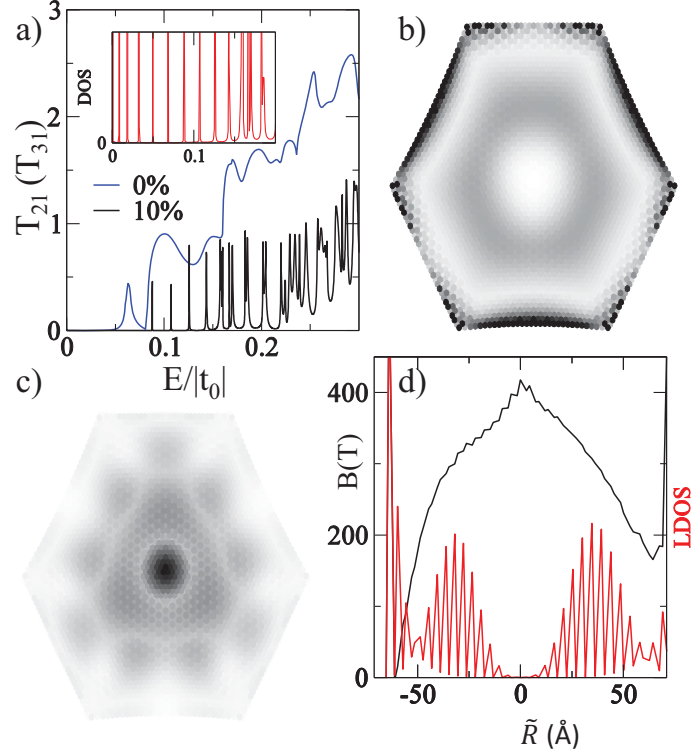


Figure 3.4: (a) Transmission coefficient $T_{21}(T_{31})$ vs E_F for $\epsilon_{\text{eff}} = 0$ and 10%. The inset shows a close-up of the total DOS of the strained dot in the low energy region. A LDOS map (white is zero) of selected transmission resonances for $\epsilon_{\text{eff}} = 10\%$ is shown in (b) for $E = 0.018t_0$, and (c) for $E = 0.16t_0$. (d) A transverse section of (b) along the vertical direction through the center of the hexagon, showing the profile of the LDOS and the PMF (“displacement approach”). \tilde{R} marks the distance to the center.

et al., 2012). To complement this exact numerical calculation of B_s at each lattice point, the displacement approach was also used for comparison and control. Both methods are used to map the PMF distribution, thus assessing the range of validity of this “displacement approach + Dirac equation” in comparison with the direct exact diagonalization on the deformed lattice.

3.1 PMF distribution

Recent experiments show in a spectacular way how strain can impact the electronic properties of graphene by confirming the existence of strain-induced LLs corresponding to fields from 300 to 600 T in graphene nanobubbles (Levy et al., 2010; Lu et al., 2012). The approach of sampling the LDOS and fitting the LL resonances to Eq. 2.13, as illustrated in Fig. 3.2, is the theoretical analog of the STM analysis done in those experiments. The real space PMF distribution for $\epsilon_{\text{eff}} = 15\%$ is shown in Fig. 3.1, and follows the general predictions of previous study (Guinea et al., 2010b). Most notably, the PMF is nearly uniform in most of the inner portion, which is a consequence of the trigonal loading conditions. This field uniformity is crucial to have well defined LLs at nominal strains as small as 3%. To quantify the dependence of the field on the nominal strain, the maximum, B_s^{max} was plotted at the center of the hexagon in Fig. 3.3, showing that, for the parameter β used here and at small ϵ_{eff} , each 1% of nominal strain increases B_s^{max} by ≈ 40 T. Direct comparison of the curves generated by the two methods mentioned above shows that B_s obtained using the “displacement approach” begins overestimating B_s beyond $\epsilon_{\text{eff}} \sim 5\%$. This is expected insofar as Eq. 2.11 results from an expansion of $V_{pp\pi}(l)$ to linear order in ϵ_{eff} , and hence is bound to overestimate the rate of change of $V_{pp\pi}$ (and thus B_s) at higher deformations. On the basis of data at low ϵ_{eff} , the scaling $B_s^{\text{max}} = C \epsilon_{\text{eff}}/L$ was extracted, with $C \simeq 3 \times 10^4$ T nm. This relation can be used to obtain B_s for systems with any L and ϵ_{eff} . For large ϵ_{eff} the data in Fig. 3.3 must be taken into account to correct for the overestimate. The magnetic lengths, ℓ_{B_s} , associated with these large PMFs can easily become comparable to the system size, and thus a strong interplay between magnetic and spatial confinement is expected. In particular, the small size of the quantum dot implies that most low energy states will not be “condensed” into LLs (Lent, 1991) and, in addition, resonant transport behavior can be seen in these

structures as a result of tunneling assisted by the magnetically confined states in the central region. This is characterized next.

3.2 Quantum transport

To calculate the quantum transport characteristics of the strained hexagon, three unstrained semi-infinite metallic armchair (AC) graphene nanoribbons were coupled to the sides of the ZZ hexagon where the load was applied (cf. inset of Fig. 3.1), thereby creating a Y-junction. There is no barrier between the metallic contacts and the central region, and the only perturbation to the electronic motion arises from the strain-induced changes in the nearest neighbor hoppings inside the hexagon. The width of the contacts coincides with the side, L , of the hexagon. In a multi-contact device the current in the p -th contact is expressed using the Landauer-Büttiker formalism as $I_p = \frac{2e^2}{h} \sum_q [T_{qp}V_p - T_{pq}V_q]$ (Datta, 1995). With no loss of generality, a bias voltage V_1 was applied to contact 1, while contacts 2 and 3 were grounded. In this configuration $I_1 = \frac{2e^2}{h} [T_{21} + T_{31}]V_1$, $I_2 = -\frac{2e^2}{h} T_{21}V_1$ and $I_3 = -\frac{2e^2}{h} T_{31}V_1$, reducing the calculations to the transmission coefficient between contact 1 and 2: T_{21} ($T_{31} = T_{21}$ under symmetric loading). The transmission coefficient is given by $T_{qp} = \text{Tr}[\Gamma_q G^r \Gamma_p G^a]$, where the Green's functions are $G^r = [G^a]^\dagger = [E + i\eta - H - \Sigma_1 - \Sigma_2 - \Sigma_3]^{-1}$, the coupling between the contacts and the device is $\Gamma_q = i[\Sigma_q - \Sigma_q^\dagger]$, and Σ_q is the self energy of contact q , all of them calculated numerically (Bahamon et al., 2010). Fig. 3.4(a) shows the transmission coefficient T_{21} ($= T_{31}$ under symmetric loading) as a function of the Fermi energy, E_F , for the Y-junction of Fig. 3.1. The smooth (blue) curve is the transmission in the absence of strain, and the resonant trace (black) the transmission for $\epsilon_{\text{eff}} = 10\%$. The unstrained junction's transmission is characterized by a threshold and a broad resonance around $E/t_0 \approx 0.063$, and a set of broad resonances and anti-resonances on a smooth background as E increases. The resonance

at the threshold marks the fundamental mode of the hexagonal cavity which, from the geometry, is estimated to appear at $E \approx \hbar v_F(\pi/\sqrt{2}L) = 0.06t_0$. Spatial mapping of the LDOS (not shown) at this energy confirms this. Upon stretching, three different regions can be identified in the curve of $T_{21}(E)$ in Fig. 3·4(a): (i) at low energies the transmission is suppressed; (ii) at intermediate energies the transmission develops a series of regularly spaced sharp resonances; (iii) at higher energies the transmission shows unevenly spaced and rapidly oscillating peaks. To characterize these different regimes, the features of the overall DOS, as well as the LDOS distribution, $N(\mathbf{r}, E) = (-1/\pi) \text{Im}[G^r(\mathbf{r}, \mathbf{r}; E)]$ were resorted, at representative energies. The DOS is shown in the inset of Fig. 3·4(a) and, even though there are plenty of low energy states, only those above $E \approx 0.08t_0$ have an appreciable signature in the transmission. To understand this absence of transmission, refer to Fig. 3·4(b), which plots a real-space LDOS map of a state at $E = 0.018t_0$, representative of these low energy states that have no signature in the transmission. Apart from the non-propagating LDOS accumulation at the ZZ edges, the significant LDOS amplitude is distributed within an annulus of radius ≈ 4 nm and width ≈ 2.5 nm. Since the LDOS does not extend to the vicinity of the contacts, revealing a small coupling between this state and the modes of the contacts, the only possibility for transmission is through tunneling. But since the spatial barrier for tunneling into this confined state is rather large (≈ 2.5 nm), the resonant peak in the transmission associated with this state has a vanishingly small amplitude and is not seen on the scale of Fig. 3·4. A transverse cut of the LDOS in (b) along the vertical direction through the hexagon center is shown in panel (d). It reflects the wavefunction of a PMF-induced Landau edge state confined to the hexagonal quantum dot, analogous to the edge states in magnetic quantum dots (Lent, 1991). As the energy is progressively increased, the associated states spread out, approaching the boundaries. Their coupling to the contacts in-

creases until the tunneling-assisted conductance becomes of the order of the quantum conductance and the associated transmission resonances become visible in the black trace of Fig. 3-4(b). The LDOS map in Fig. 3-4(c) corresponds to $E = 0.16t_0$, and typifies the behavior at higher E_F . It is clear that this state is completely different from the one in Fig. 3-4(b), as its LDOS spreads over the entire quantum dot and is highly peaked at the center. It corresponds to a state in the $n = 1$ LL. The rapid oscillations in the transmission coefficient and DOS at that energy are also consistent with this interpretation (Sivan et al., 1989). An additional quantitative confirmation is given as follows. If the state at $E = 0.16t_0$ belongs to the $n = 1$ LL, its associated magnetic length will be $\ell_{B_s} = \sqrt{2\hbar v_F/E_{n=1}} \simeq 1.9$ nm. The energy difference between Landau edge states whose energy is below $E_{n=1}$ will be given by $\Delta E \approx E_{n=1}\ell_{B_s}/2L \approx 0.02t_0$ (Sivan et al., 1989). Inspecting the inset of Fig. 3-4(a) one sees that below $E \simeq 0.1t_0$ the level spacing is indeed $\sim 0.02t_0$. Moreover, given that this quantitative estimate is consistent, the average magnetic field determining the transport behavior can be extracted, which is $B_s^{\text{av}} = \hbar/e\ell_{B_s}^2 \simeq 164$ T. This value, obtained independently and solely from the transmission characteristics, expectedly corresponds to the PMF in the region of maximum LDOS for this state: from Fig. 3-4(d), and correcting for the overestimation in the PMFs obtained from the “displacement approach” in Fig. 3-3, that would be $\approx 270/1.6 = 169$ T. Hence, transport in the strained junction is characterized by LL-assisted resonant tunneling, analogously to a magnetic quantum dot, with the novelty that here the Landau quantization arises from the strain-induced PMF, B_s . Due to the effective magnetic barrier, electrons injected from contact 1 can tunnel with a probability $0 < T < 1$, which is enhanced when there is significant LDOS in the contact region. The maximum tunneling probability through a localized state is $T = 1$, irrespective of the number of open channels in the contacts. This implies that between the LL $n = 0$ and $n = 1$, $T_{21}^{\text{max}} = 0.5$ is expected (0.5 because

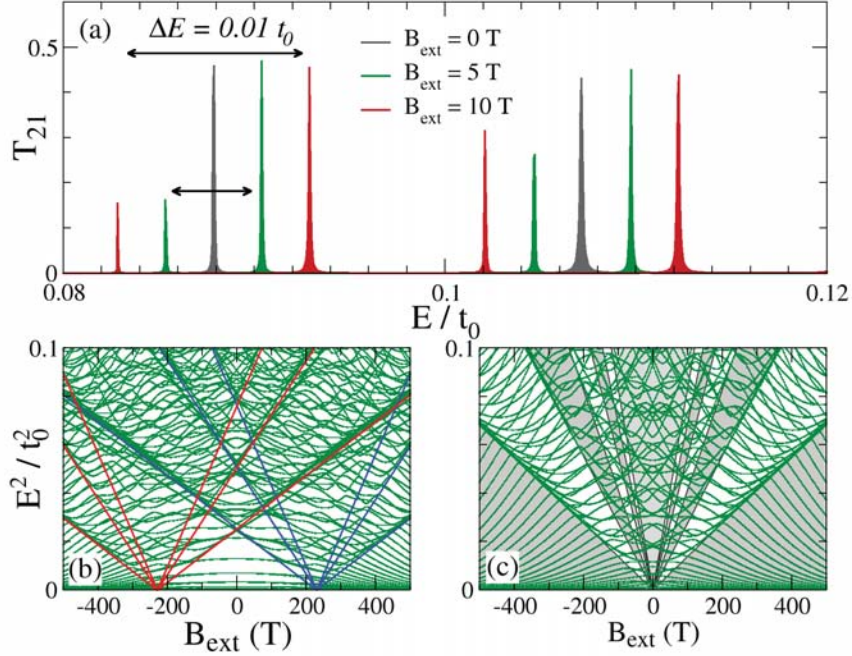


Figure 3-5: (a) Detail of the splitting in the T_{21} resonances under an external field B_{ext} , for $\epsilon_{\text{eff}} = 10\%$. (b) Eigenenergies of the same hexagon vs B_{ext} , when disconnected from the contacts. (c) Likewise, but for $\epsilon_{\text{eff}} = 0$, where LL condensation (Lent, 1991) is more clearly observed. In (b) and (c) straight lines mark the lowest LLs in the infinite system, and the large range of B_{ext} used in the horizontal axes is to accommodate the very large PMF induced by strain.

there are two symmetric exit channels). However each LL with $n \neq 0$ in graphene is doubly degenerate, and hence $T_{21}^{\text{max}} = 1$, which is consistent with the calculated transmission seen in Fig. 3-4(a), where $T_{21}(E = 0.126t_0) = 0.79$, for example.

3.3 Valley splitting

The strain-induced PMF does not break time-reversal symmetry (TRS) in the system, which in practice means that a low energy electron around one of the zone-edge valleys feels a PMF which is exactly the opposite to the one felt by its TRS counterpart at the other inequivalent valley. This leads to the degeneracy discussed above and,

in addition, to the result that the currents associated with the two valleys exactly cancel each other. This degeneracy is lifted under a real magnetic field, B_{ext} , since the total field at each valley will be different: $B_{\text{ext}} \pm B_s$. The corresponding LL splitting is given by $E_n^+ - E_n^- \simeq E_n B_{\text{ext}} / B_s^{\text{av}}$. Fig. 3·5(a) shows explicitly this splitting for the edge states detached from the $n = 1$ LL. Taking the values estimated above for $B_s^{\text{av}} \simeq 164 \text{ T}$, and $E_{n=1} \simeq 0.16 t_0$, the expected splitting under the external field is $(E^+ - E^-) / t_0 \simeq 0.001 B_{\text{ext}} \text{ T}^{-1}$. Direct inspection of Fig. 3·5(a) shows that this is indeed quantitatively verified. A different perspective over the splitting of valley degeneracy is given in Fig. 3·5(b), which shows the spectrum of the strained hexagon disconnected from the contacts, as a function of B_{ext} . When compared with the unstrained case in Fig. 3·5(c), one sees that the effect of the large PMF induced by strain is to split the Landau fan, which is a clear evidence of valley degeneracy breaking. Notice also that this degeneracy breaking is visibly achieved under 10 T, as shown in Fig. 3·5(a). Another interesting consequence of breaking the valley degeneracy is that, as B_{ext} increases, the edge states in one valley will shrink to a smaller radius than in Fig. 3·4(b), whereas the ones associated with the other will expand due to the opposite evolution of the respective magnetic lengths. Therefore, by increasing B_{ext} one can spatially “expand” the edge states of one valley [cf. Fig. 3·4(b)] so that they start coupling more effectively with the leads. This is reflected in Fig. 3·5 by the asymmetry in T_{12} of the split transmission resonances: the state which increases in energy under B_{ext} is the one whose ℓ_B increases, thereby facilitating the resonant tunneling process, and displaying higher transmission than its counterpart associated with the other valley. Consequently, with an external field one can restrict the assisted tunneling to states from one or the other valley. The current path will then have a well defined chirality depending on which valley is assisting the tunneling. This suggests the possibility of exploring this chiral resonant tunneling to channel

the current from lead 1 selectively to lead 2 or 3.

3.4 Asymmetry, disorder and lattice orientation

The triaxial strain profile of Fig. 3.1 was chosen in this investigation as it provides a nearly optimal PMF distribution within the nanostructure (Guinea et al., 2010b). However, the magnitude of the PMF will depend on the relative orientation of traction and crystal directions, implying that the magnitude of the confining effects, for example, is sensitive to that orientation. This is a general feature of strain induced PMFs in graphene. Likewise, non-symmetric triaxial tension perturbs the PMF distribution as well, which has consequences for the electronic behavior. For a perspective on this, the transport behavior was discussed for different lattice orientations, as well as asymmetric tension. An analysis of the consequences of edge roughness shows that the LL-assisted tunneling is sensitive to the amount of roughness at the boundaries, which is expected since the large PMF at the center of the hexagon forces the current to flow close to the boundary. In this sense, the experimental exploration of the LL-assisted tunneling described here is more straightforwardly observable in graphene structures synthesized via bottom-up microscopic approaches (Zhi and Mullen, 2008; Cai, 2010), or artificial graphene structures (Gomes and *et al.*, 2012), where the effects of fabrication-induced disorder can be minimized. With respect to the strain symmetry, it is observed that extreme deviations from symmetric traction deteriorate the LL-assisted resonant tunneling that is possible under the conditions discussed above. This arises because asymmetric strain displaces the region of strong field towards one of the boundaries. This, on the other hand, can be explored to selectively block one of the output contacts in the y-junction, allowing control over which of the two is the exit channel. A specific case is analyzed bellow.

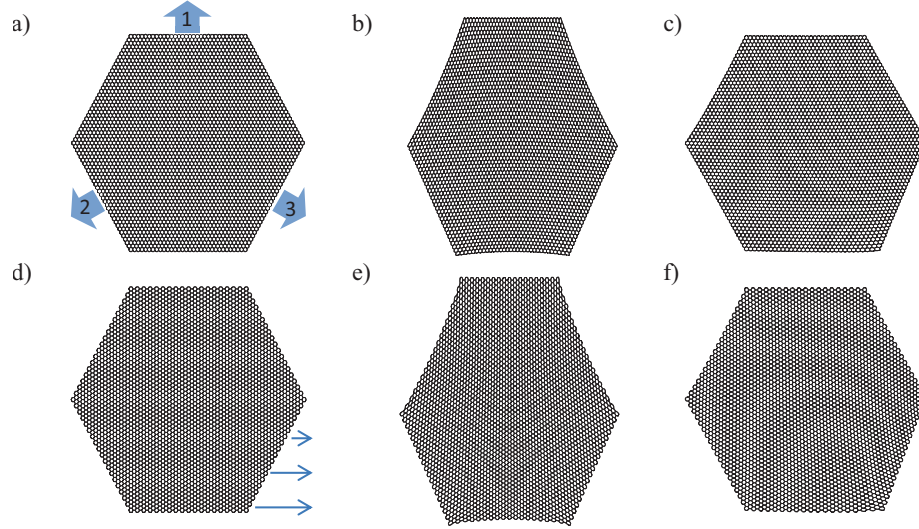


Figure 3-6: (a) Hexagon (0% strain) with ZZ edges. The arrows are a schematic representation of the symmetrically applied tri-axial strain. In the transport calculations the contacts are attached to the edges under traction as well because the edge atoms are held fixed along the direction transverse to the tension, which allows us to keep the metallic contacts undeformed. (b) Deformed hexagon with ZZ edges after 10% of symmetric strain. (c) Deformed hexagon with ZZ edges after 15% of asymmetric (ramp) strain. (d) Hexagon (0% strain) with AC edges. The arrows are a schematic representation of the asymmetrical (ramp) strain setup. (e) Deformed hexagon with AC edges under 15% of symmetric strain. (f) Deformed hexagon with AC edges under 15% of asymmetric (ramp) strain.

3.4.1 Deformed hexagons under strain

Fig. 3-6 shows the hexagonal quantum dots considered in this study under different loading conditions and for different lattice orientations with respect to the applied strain. The strategy used to explore deviations from the symmetric loading is shown schematically in Fig. 3-6(d). In this case the traction was applied only to edge 3, and in such a way that the displacement follows a ramp pattern, being maximal at one end of the edge and linearly decreasing to zero towards the opposite end. Edges 1 and 2 were held fixed Figs 3-6c and 3-6f show the actual relaxed structures after the MM simulation under this ramp traction profile, and for 15% of atomic displacement

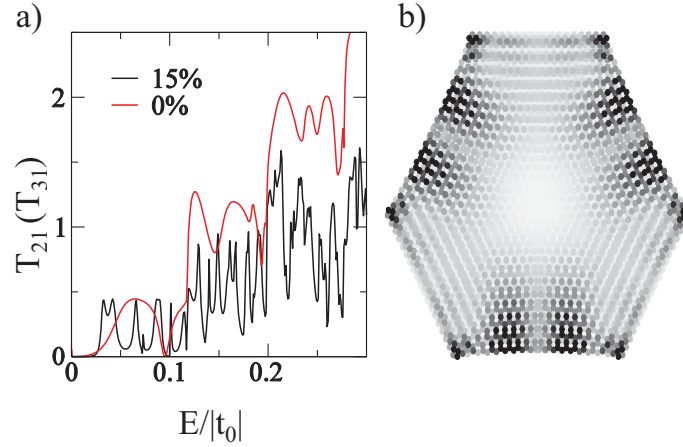


Figure 3.7: (a) Transmission coefficient $T_{21}(T_{31})$ vs Fermi Energy for a symmetrically strained AC Y-junction. (b) LDOS mapping at $E = 0.043t_0$ for the 15% symmetrically strained AC Y-junction.

applied to the lower atoms.

3.4.2 Armchair Y-junction

The electronic spectrum and transport characteristics of graphene nanostructures is strongly influenced by the nature of the edges. Strain-induced PMFs also depend on the relative orientation of the strain with respect to the underlying crystal directions of the graphene lattice. Here a quantum dot was considered with the same geometry and the same approximate dimensions as the one discussed above, but for which the graphene lattice has been rotated so that the edges were the armchair type. This corresponds to a rotation of the original lattice by $\pi/2$, or any other equivalent angle.

The calculation of the transmission was done now by attaching three unstrained semi-infinite zigzag graphene nanoribbons, which acted as ideal contacts. The contacts were connected to the sides of the hexagon where the load was applied, creating an AC Y-junction. In Fig. 3.7(a) it shows the transmission coefficient for 0% strain (red). As discussed above for the ZZ case, the onset of transmission in the unstrained structure is characterized by a very broad hump that is associated with the funda-

mental mode of the cavity. The different nature of the AC edges manifests itself by the wider and deeper resonances and anti-resonances that develop as the energy increases, in comparison with the transmission fingerprint of the unstrained ZZ junction discussed above. When strain was applied up to the nominal value of 10% the transmission coefficient mostly resembles the unstrained case, and the case of $\epsilon_{\text{eff}} = 15\%$, represented by the black curve in Fig. 3·7(a) was still qualitatively similar to the unstrained situation. More specifically, despite the additional structure, there were no isolated resonant peaks in contrast to the case of the ZZ junction, and transmission was never zero after the initial onset at around $E \simeq 0.02$. In clear contrast with the case analyzed above for ZZ Y-junction, the transmission signature of this junction is not compatible with the presence of a significant pseudomagnetic field within the central region of the hexagon. Direct inspection of the real-space LDOS distribution at the transmission peaks confirms this. Fig. 3·7(b) represents a density plot of the LDOS for the transmission peak at $E = 0.043t_0$, revealing a LDOS distribution qualitatively similar to any resonance in the unstrained structure.

The inference that there is no significant homogeneous magnetic field within the junction from the transport fingerprint alone is compatible with the expectation for the pseudomagnetic field distribution anticipated in this case. Despite the generic relevance of the edge chirality in small graphene structures, the crucial detail in the context of generating suitable PMF distributions is the orientation of the lattice with respect to the strain directions. On the basis of the results derived in reference (Guinea et al., 2010b) it is expected that the magnitude of the PMF near the center of the hexagon to vary with the lattice orientation as $\propto \cos(3\varphi)$, where $\varphi = 0$ corresponds to a lattice with a ZZ direction along the horizontal axis. Since the AC case studied in Fig. 3·7 corresponds to $\varphi = \pi/6, \pi/2$, etc. the magnitude of the pseudomagnetic field is expected to be mostly suppressed in the central region.

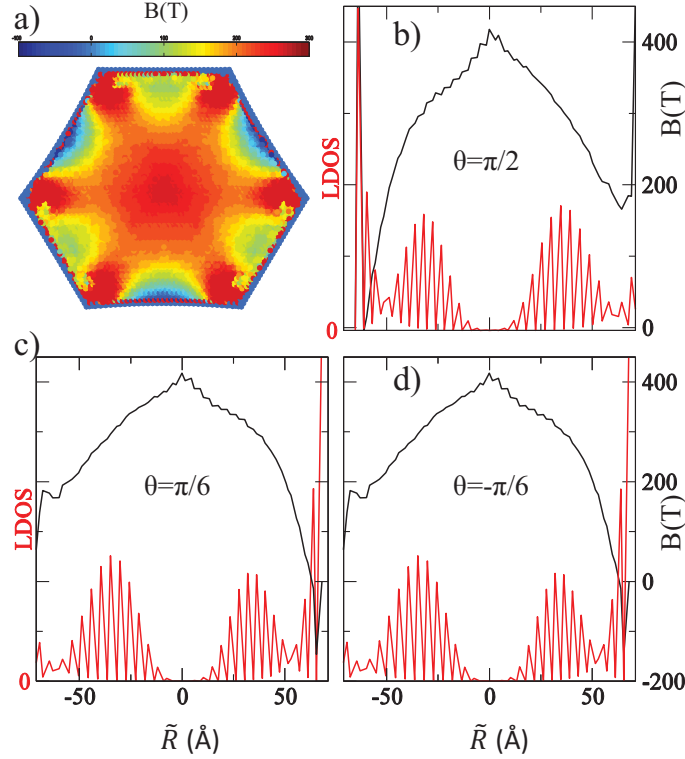


Figure 3-8: Sections of B_s and LDOS for a strained ZZ Y-junction with $\epsilon_{\text{eff}} = 10\%$. Panel (a) shows a density plot of B_s in the entire system obtained with the “displacement approach”. In panels (b)-(d) the profile of B_s (black) and LDOS (red) at $E = 0.018t_0$ were plotted along the directions defined in the text: $\theta = \pi/2$, $\theta = \pi/6$, and $\theta = -\pi/6$, respectively.

3.4.3 Profile of B_s and LDOS (ZZ junction)

The case of a ZZ junction under $\epsilon_{\text{eff}} = 10\%$ above was studied in detail. From the nature of the resonant transmission at low energies, and from the equidistant spacing between resonances, an average PMF B_s^{av} determining the behavior of transmission was extracted. Moreover, the resonant transmission occurred only through the assistance of those edge states whose radius was such that they effectively couple to the contacts at the border.

To clarify these points, the values of B_s and LDOS at $E_1 = 0.018t_0$ in the ZZ junction with $\epsilon_{\text{eff}} = 10\%$, were extracted along transverse sections equivalent by

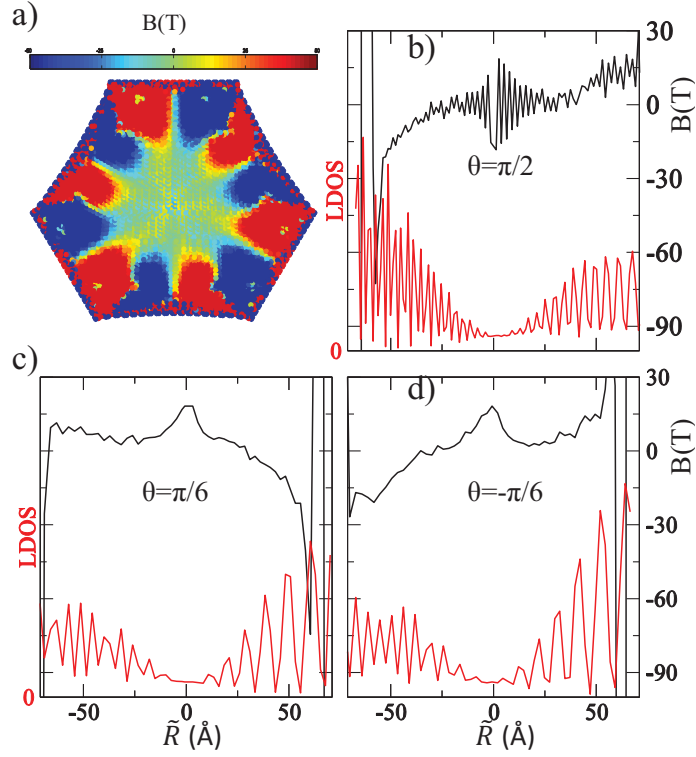


Figure 3.9: Sections of B_s and LDOS for a strained AC Y-junction with $\epsilon_{\text{eff}} = 15\%$. Panel (a) shows a density plot of B_s in the entire system obtained with the “displacement approach”. In panels (b)-(d) the profile of B_s (black) and LDOS (red) at $E = 0.043t_0$ were plotted along the directions defined in the text: $\theta = \pi/2$, $\theta = \pi/6$, and $\theta = -\pi/6$, respectively.

symmetry. The origin of coordinates is set at the center of the strained hexagon, with the x and y axes along the conventional horizontal and vertical directions. The direction of the transverse section with respect to the horizontal axis is defined by the angle θ , and the position of a point in the lattice along this section is identified by $\tilde{R} = \text{sign}(y)\sqrt{x^2 + y^2}$. The three equivalent transverse sections are considered along $\theta = \pi/2$ and $\pm\pi/6$. For example, contact 1 appeared at $\tilde{R} \approx 74 \text{ \AA}$ in a section taken along $\theta = \pi/2$. These three sections were chosen to confirm and highlight the isotropy of both B_s and the LDOS in the interior of the structure.

The overall distribution of B_s within the hexagon is shown in Fig. 3-8(a). The value of B_s shown here was extracted using the ‘‘displacement’’ approach discussed in Section 2.2.1. It consists in using the coordinates of the relaxed atoms directly to interpolate the strain tensor, after which the vector potential \mathbf{A}_s is extracted. This method has the potential disadvantage of requiring a sequence of two numerical derivatives to obtain the value of B_s at a given lattice point, given the relaxed atomic coordinates, and also overestimates B_s at large deformations, as shown in Fig. 3-3. However it is much more expeditious than the mapping of the LDOS, and extraction of the local LL spectrum from the tight-binding calculation, which was the method used to plot B_s in Fig. 3-1. Correcting for the overestimate in magnitude discussed and shown in Fig. 3-3, the distribution of B_s obtained with either method in the interior of the structure is equivalent. The values of B_s and LDOS along the three sections mentioned above are plotted in Figs. 3-8(b)-(d), represented by the black traces. The LDOS is plotted together with the PMF along the three sections, represented by the red traces. First, note that the large peaks located at boundary $\tilde{R} = -65 \text{ \AA}$ ($\theta = \pi/2$), $\tilde{R} = 68 \text{ \AA}$ ($\theta = \pi/6$), and $\tilde{R} = 68 \text{ \AA}$ ($\theta = -\pi/6$) are due to ZZ edge states. At the opposite boundary (where the contacts are attached) the LDOS is small, signaling that this state is well confined within the interior of the structure,

and that the probability of transmission through it is small. The most interesting detail of the LDOS distribution, however, is its distribution in the interior of the structure. It is clear that the wave function does not follow local features in B_s , such as changes of strength or sign of B_s (Masir et al., 2011). In contrast, the LDOS intensity is almost completely confined to an annular region inside the junction, fully resembling the LDOS of an edge state in a magnetic quantum dot, as described by Lent (Lent, 1991). From the LDOS profile $\ell_{B_s} \approx 2$ nm is obtained, which corresponds to the average field $B_s^{\text{av}} = \hbar/el_{B_s}^2 \simeq 164$ T.

3.4.4 Profile of B_s and LDOS (AC junction)

The procedure described in the previous section was applied to the analysis of the AC junction with $\epsilon_{\text{eff}} = 15\%$. As expected, the magnitude of B_s is roughly zero in the interior region of the junction. Sharp features appear only around small regions near the corners and edges, where the field is strong and alternates in sign. Figs. 3-9(b)-(d) show the profile of B_s together with the LDOS at $E = 0.043t_0$, the same energy used in Fig. 3-7 above.

3.4.5 Edge roughness and asymmetric strain

In order to simulate the effect of edge roughness, vacancies were added with a probability of 0.4 to the edges of the two types of Y-junction. These vacancies were added in the strained electronic Hamiltonian neglecting the relaxation of local strain in the vicinity of the vacancy. This simplification should not modify the results since the main ingredient is that edge roughness reduces the transmission through pseudo-magnetic edge states (standing waves in the strain barrier) for ZZ edged Y-junctions, as can be seen in Fig. 3-10(a). In these structures the B_s in the interior of the junction behaves like a barrier, pushing the current towards the edges. This current is effectively suppressed at low energies by the strong backscattering induced by the

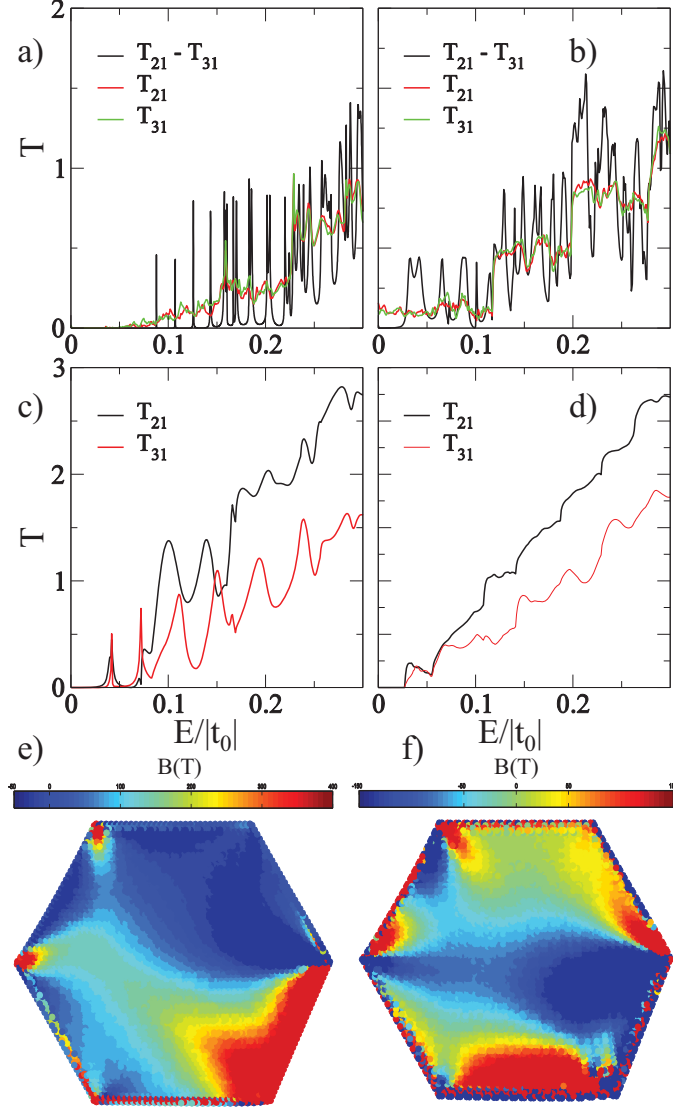


Figure 3-10: Transmission coefficient for: (a) 10% strained ZZ Y-junction with and without edge disorder; (b) 15% strained AC Y-junction with and without edge disorder; (c) 15% asymmetrically strained ZZ Y-junction; (d) 15% asymmetrically strained ZZ Y-junction with edge disorder. In panels (e) and (f) the distribution of B_s was displayed generated by the asymmetric traction illustrated in Fig. 3-6(d) for the case of, respectively, the ZZ and AC edged hexagon nanostructures considered in this work.

vacancies. This creates the gap in transmission at low energies that can be seen in Fig. 3·10(a). In the AC-edged hexagonal dot, since the average $B_s \approx 0$ in the center of the Y-junction, current flows easily through the central region, and there is no transmission gap.

To address the problem of asymmetry in the traction (and consequently in the overall strain distribution), the extremely asymmetric situations considered are illustrated in Figs. 3·6(c) and (f). The transmission data is shown in Fig. 3·10(c), for a structure where a ramp displacement is applied only to the hexagon side where the third contact is attached. An asymmetric strain pattern ensures that $T_{21} \neq T_{31}$, and can potentially be explored to channel the current between specific pairs of contacts by suitable asymmetric traction conditions. The ramp strain considered here creates a B_s that is not uniform in the center of the hexagon, but has a strong maximum in the vicinity of the third contact. Although the values of B_s in that region are large ($\ell_{B_s} < L_0$), and of the same order of magnitude as the ones found in the symmetric junction, the transmission and LDOS signatures are rather different from the signatures of a symmetrically strained hexagon. In particular the resonant peaks in T_{31} at $E = 0.042t_0$ and $E = 0.072t_0$ are due to states having a LDOS distribution of two distorted standing waves, rather than the magnetic edge state profiles seen in the symmetric case in Fig. 3·8. The reason for the different behavior is mostly due to the non-uniform nature of B_s in the interior of the system, in comparison with the symmetrically strained situation. This means that the electrons don't feel a quantum dot with a nearly constant magnetic field everywhere in this case, but instead are scattered from the regions of higher field. In essence, this extreme asymmetric case results in a distribution of B_s that acts as a barrier for current flow only in certain regions inside the Y-junction. Since that barrier is higher in the region of contact 3 the current is scattered to contact 2 and, consequently, $T_{31} < T_{21}$. This imbalance in

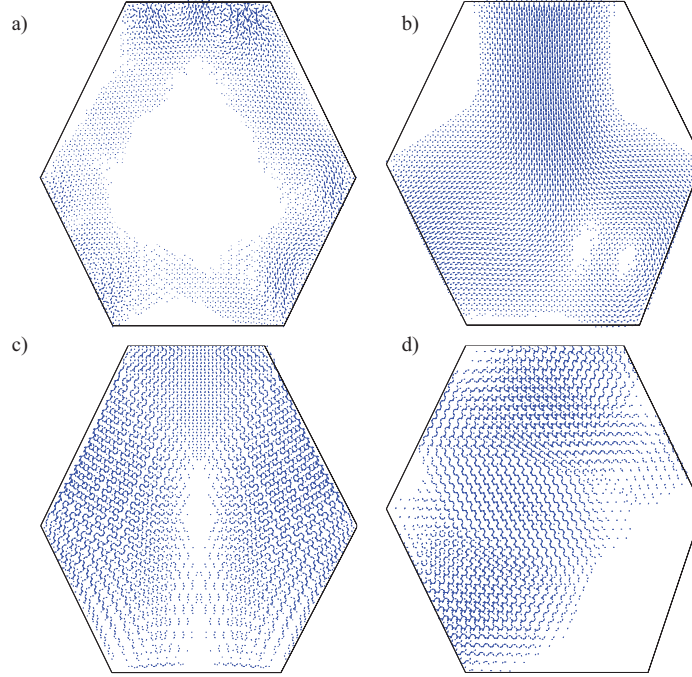


Figure 3-11: Current density mapping in real space for selected transmission features discussed above: (a) $E = 0.126t_0$ for the symmetric ZZ Y-junction with $\epsilon_{\text{eff}} = 10\%$; (b) for the asymmetrically strained ZZ Y-junction with $\epsilon_{\text{eff}} = 15\%$ at $E = 0.1t_0$; (c) at $E = 0.033t_0$ for the symmetric AC Y-junction with $\epsilon_{\text{eff}} = 15\%$; (d) for the asymmetrically strained AC Y-junction at $E = 0.095t_0$. In all plots, the length of the arrow is proportional to the value of the density current in that point.

T_{31} vs T_{21} becomes even more evident at higher energies. Inside the ZZ Y-junction, for low energies, the current flows through the regions of low B_s , as shown in more detail the next section.

The effect of edge disorder in the asymmetric ZZ junction is presented in Fig. 3-10(d), where the effect is not as marked as in the symmetric case shown in Fig. 3-10(a). This is consistent with the above description of the transmission process in this case, whereby electronic current flows through the large portions of the hexagon that are not under a significant B_s .

3.4.6 B_s as a barrier

The current between neighboring sites m and n can be expressed as (Datta, 1995; Bahamon et al., 2011)

$$I_{mn} = \frac{2e}{h} \int_{-\infty}^{+\infty} dE [t_{nm} G_{mn}^< - t_{mn} G_{nm}^<], \quad (3.1)$$

where the lesser Green's function in the absence of interactions can be written as $G^<(E) = G^r(E)[\Gamma_1 f_1 + \Gamma_2 f_2 + \Gamma_3 f_3] G^a(E)$. $f_{1(2)(3)}$ is the Fermi distribution in the respective electrodes. The current density is mapped for different energies for the ZZ and AC Y-junction with symmetric and asymmetric strain. For reference, Fig. 3-11 shows the current maps for some of the cases discussed above.

The case plotted in Fig. 3-11(a) pertains to a symmetrically strained ZZ Y-junction, at the energy $E = 0.126t_0$ that corresponds to one of the isolated transmission resonances. Since B_s is strong in most of the interior region, the current path exhibits the intuitively expected behavior by flowing through the regions of smallest field towards the edges. Due to the microscopic details of B_s the current density distribution is not perfectly symmetric between contacts 1-2 and contacts 1-3. A higher density of current flows between 1-3, and part of it is scattered from contact 3 to contact 2 ensuring final transmissions of $T_{21}(0.126t_0) = 0.31 \approx T_{31}(0.126t_0) = 0.32$.

For the asymmetrically strained ZZ Y-junction in Fig. 3-11(b) the bulk of the current flows directly through the center of the junction, exiting predominantly via contact 2. Most of the current near contact 3 is scattered towards 2, since in the asymmetric ZZ case the magnetic barrier induced by B_s is displaced to the vicinity of 3. This explains the quantitative imbalance in the respective transmissions: $T_{21}(0.1t_0) = 1.37 > T_{31}(0.1t_0) = 0.47$ [cf. Fig. 3-10(c)]. The qualitative picture is similar for the AC Y-junction asymmetrically strained by 15% in Fig. 3-11(d). The

main point is that under asymmetric traction conditions the distribution of B_s is no longer nearly homogeneous in the central region, and a strong maximum appears towards one of the pulling arms. This restricts the magnetic barrier to a particular portion of the system, but does not lead to the Landau level assisted tunneling resonances seen in the symmetric ZZ case. The asymmetric cases can be understood intuitively by considering the regions of strong B_s as barriers that divert the electronic current, and lead to an asymmetry in the conductance measured between contacts 1–2 and 1–3.

For completeness in Fig. 3.11(c) the current density in a 15% symmetrically strained AC Y-junction is also shown, extracted at a maximum in the transmission at $E = 0.033t_0$.

Chapter 4

Graphene Bubble: Three Dimensional Deformation and Electromechanical Coupling

4.1 Simulation setup

The graphene nanobubble system consisted of three parts, as illustrated in Fig. 4-1: a graphene monolayer, the hexagonal (111) surface of an face-centered cubic (FCC) gold substrate, and argon gas which was used to inflate the graphene bubble. The substrate-graphene and gas-graphene interactions were modeled by a standard 12-6 Lennard-Jones potential:

$$V(r_{ij}) = 4 \epsilon_{ij} \left[\left(\frac{\sigma_{ij}}{r_{ij}} \right)^{12} - \left(\frac{\sigma_{ij}}{r_{ij}} \right)^6 \right], \quad (4.1)$$

where r_{ij} represents the distance between the i -th carbon and the j -th gold atom. The dimension of the simulation box was $20 \times 20 \times 8 \text{ nm}^3$, and the substrate was comprised of Au atoms with a thickness of 2 nm, or about 2.5 times the cutoff distance of the interatomic potential (Neek-Amal and Peeters, 2012a). Apertures of different shapes (viz. triangle, rectangle, square, pentagon, hexagon, and circle) were “etched” in the center of the substrate to allow the graphene membrane to bulge inwards due to the pressure exerted by the Ar gas. The whole system was first relaxed for 50 ps, at which time the Ar gas was pushed downward (as in a piston) to exert pressure on the graphene monolayer, causing it to bulge inward in the shape cut-out

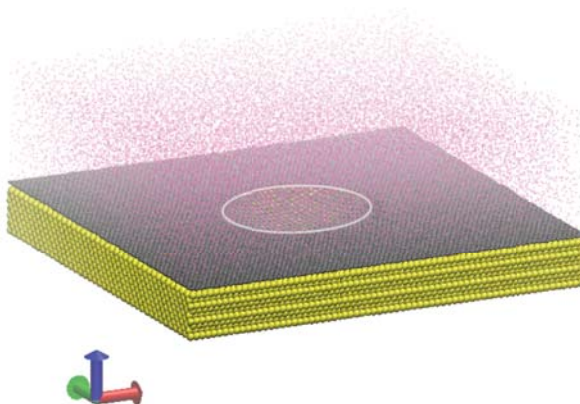


Figure 4.1: Illustration of the strategy employed in the studies to generate nanobubbles by pressurizing graphene through a predefined substrate aperture. The picture shows one of the actual simulation cells used in MD computations. In gold, gray and red colors are represented, respectively, the Au substrate, the graphene sheet and the Ar atoms. A hole is carved in the Au substrate (perimeter outlined), and its perimeter geometry determines the shape of the resulting graphene bubble. Visualization is performed using VMD (Humphrey et al., 1996).

from the gold substrate. The system was then allowed to equilibrate again under the increased gas pressure. All simulations were carried out at room temperature (300 K) using the Nose-Hoover thermostat (Hoover, 1985). The choice of Ar in the calculations is not mandatory. Substitution with other molecular species should pose no difficulty, the same being true regarding the substrate, as shown previously in references (Neek-Amal and Peeters, 2012a; Neek-Amal et al., 2012). To elucidate the effect of different substrates on the PMF distributions in the nanobubbles, MD simulations were performed with two different substrates, in addition to performing the simulations with fixed edges and no substrate. Specifically, both Au and Cu (111) substrates were used, where the detailed parameters and descriptions will be discussed in later sections. After obtaining the graphene bubble, the pressure was held constant for 10 ps to achieve thermal equilibrium. Note that during the entire simulation no gas molecules leaked away from the system, which again demonstrates the experimentally

observed atomic impermeability of monolayer graphene (Nair et al., 2012; Bunch et al., 2008).

The simulations are close in spirit to the experiments reported in reference (Koenig et al., 2011), but targeting smaller hole apertures due to computational limitations. This method of using gas-pressure to generate the graphene nanobubbles is different from the situations explored in the recent experiments that focus on the PMF distribution (Levy et al., 2010; Lu et al., 2012). However, it is in some ways more controllable due to the utilization of a substrate with a distinct pattern coupled with externally applied pressure to force graphene through the patterned substrate to form a bubble with controllable shape and height. The final (inflated bubble) configuration gives the basic ingredients needed to extract the strain distribution in the system, as well as the perturbed electronic hopping amplitudes. To calculate the strain directly from the displaced atomic positions, “displacement” approach is employed. A previous study (Klimov et al., 2012) used “stress” approach for a similar calculation. However, the stress approach fails to predict reasonable results in this case, which attributes to the inability of the virial stresses to properly convey the total stress at each atom of the graphene sheet when the load results from interaction with gas molecules. Furthermore, in the stress approach one assumes a planar (and, in addition, usually linear) stress-strain constitutive relation which leads to errors when large out-of-plane deformations arise, as in the case of the nanobubbles.

PMF is the central quantity of interest in this work; in the subsequent sections the combined effects of gas pressure, hole geometry, and substrate interaction will be analyzed from the point of view of the resulting magnitude and space distribution of the PMF, B , obtained in this way. For definiteness it is set as $q = e$, e being the elementary charge, which means that the PMF is analyzed from the perspective of holes ($q > 0$).

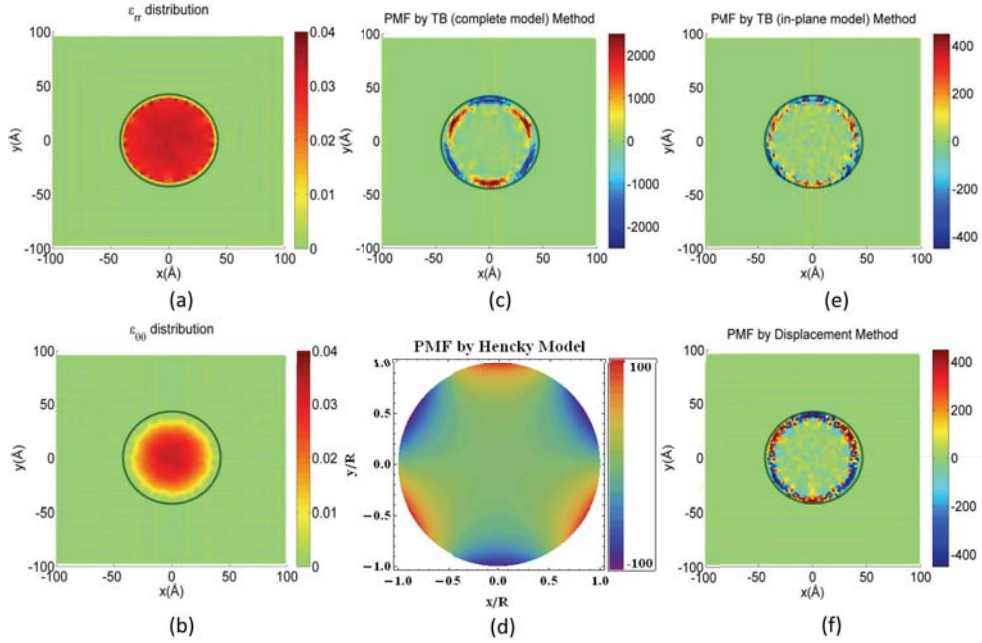


Figure 4.2: Results for a circular graphene bubble with 4 nm radius and pressurized up to ~ 1 nm deflection; in this case graphene was clamped at the edge of the substrate aperture. (a) Radial strain, (b) tangential strain, (c) PMF by TB method with both in-plane and bending components, (d) PMF arising from Hencky’s analytic model (Fichter, 1997) with the axes scaled in units of the circle radius, (e) PMF by TB method with in-plane component only, (f) PMF by displacement method. Note that, except for (d), all the panels refer to the same atomistic configuration. PMF shown in units of Tesla. The edge of the substrate aperture used in the MD simulation is outlined (gray line) for reference.

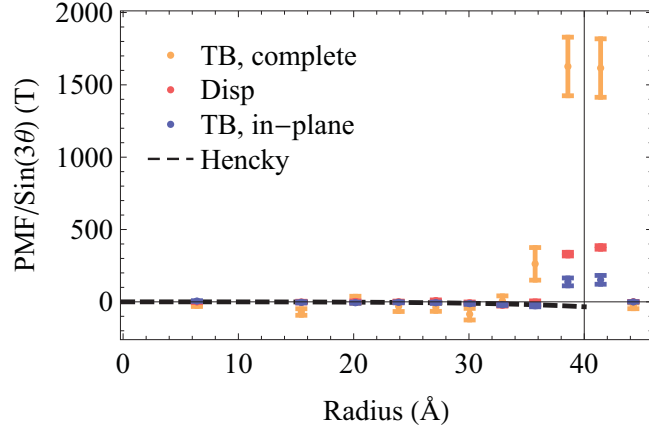


Figure 4-3: Angular-averaged amplitude of the PMF for the same cases presented in Fig. 4-2 in the form of density plots. The horizontal axis represents the distance from the center of a pressurized circular graphene nanobubble with clamped boundary conditions. The data contained here is the same shown in Fig. 4-4(a), except that here the (orange) data corresponding to the PMF obtained from the full hopping perturbation [Eq. 2.7] is included for comparison as well. The bending effects are clearly dominant around the edge/clamping region. Away from the edge, and inside, the three numerical curves follow Hencky’s model.

Fig. 4-3 below shows the radial dependence of the averaged PMF amplitude close to the edge of the circular aperture for the clamped circular case discussed in section 4.2 (Fig. 4-2).

The data shown reflect the PMF amplitude averaged over the azimuthal direction. To extract the average PMF at a given radius, the 2D distribution of the field is divided into a sequence of radial and azimuthal bins (annular sectors). For each radial annulus there are 20 bins, each with a 18 degree width. The width of the radial annulus is chosen such that at least 10 atoms lie in each bin (this is why there are fewer data points near the center of the bubble). The average and standard deviations of the PMF in each bin correspond to the value and error bar of that bin. For example, each point in Fig. 4-6(c) corresponds to this average PMF for a

given bin. Afterwards, for each radial annulus the data is fit to the expected $\sin(3\theta)$ dependence. The amplitude of the best fit is plotted as a point [e.g., as in Fig. 4.3] and the fitting error provides the error bar.

4.2 Clamped graphene nanobubbles

The simulation cases start an idealized system consisting only of Ar gas molecules and graphene, neglecting the interaction with the underlying substrate, and where all carbon atoms outside the aperture region are strictly fixed during simulation. This provides a good starting point to understand how the shape of the substrate aperture affects the PMF distribution. A similar system has been used in previous work (Wang et al., 2013), as this corresponds to a continuum model with clamped edges (Guinea et al., 2008; Kim et al., 2011). Analysis starts with the most symmetric geometry, a circular graphene bubble, and compares the atomistic result with the continuum Hencky solution (Fichter, 1997). In contrast to small deformation continuum models (Kim et al., 2011), the Hencky model is valid for large in-plane (stretching) deformations, which lead to a different PMF distribution. To compute the PMFs associated with this analytical solution Eq. 2.11 was used. Figs. 4.2(c,d) show that the PMF distribution is dominated by very large magnitudes at the edges followed by a rapid decay towards the inside region of the nanobubble. Both the MD and Hencky results show the six-fold symmetry expected for a cylindrically symmetric strain distribution; this agreement demonstrates the MD simulation successfully captures the strain distribution underlining the computed PMF. There are, however, two quite clear discrepancies between the PMF in these two figures: (i) Hencky's solution (panel d) yields values considerably smaller in magnitude than the calculation based on the MD deformations combined with Eqs. 2.7 and 2.10 (panel c); (ii) the sign of the PMF in panel (d) is *apparently* reversed with respect to the sign of panel

(c). These discrepancies stem from the substantial bending present in graphene near the hole perimeter, and deserve a more detailed inspection in terms of the relative magnitude of the two contributions to the hopping variation: bond stretching and bond bending. Since Hencky’s result of Fig. 4·2(d) hinges on Eq. 2.11 that expresses the vector potential directly in terms of the strain tensor components, it starts by analyzing the predictions obtained by applying it to the atomistic case as well; to do that one computes the strain from the MD simulations using the displacement approach discussed earlier. The result of that is shown in Fig. 4·2(f), where the most important difference in comparison with Fig. 4·2(c) is the significant reduction of the maximal fields obtained near and at the edges; this reflects the error incurred in the quantitative estimate of B when the effect of bending is neglected. Note that, by construction, Eq. 2.11 accounts only for the bond-stretching, and is accurate only to linear order in strain because it is based on a linear expansion of the hopping in the interatomic distances. Hence, in order to correctly extract from the atomistic simulations the total stretching contribution beyond linear order while still ignoring bending effects, the PMF calculation should be done with the hopping as defined in Eq. 2.7 (TB approach), but explicitly setting $\mathbf{n}_i \cdot \mathbf{n}_j = 1$ and $\mathbf{n}_i \cdot \mathbf{d} = 0$ (*i.e.* assuming local flatness). The outcome of this calculation is shown in Fig. 4·2(e) which, in practical terms, is the counterpart of Fig. 4·2(c) with bending effects artificially suppressed. In comparison with panel (f), it leads to slightly smaller PMF magnitudes. The linear expansion in strain of Eq. 2.10 thus slightly overestimates the field magnitudes, something expected because the hopping is exponentially sensitive to the interatomic distance and, by expanding linearly, one overestimates its rate of change with distance, overestimating the field magnitude as a result. One key message from Fig. 4·2 and the comparison between panel (c) and any of the subsequent ones is that the effects of curvature are significant at these scales of deflection and bubble

size, particularly at the edge, where they clearly overwhelm the “in-plane” stretching contribution. This will be revisited in more detail in section 4.5.

The second key message gleaned from Fig. 4.2 pertains to the importance of properly considering the boundary and loading conditions when analytically modeling the strain and deflection of graphene. This is related to the apparent opposite sign in the PMF at the edge obtained from Hencky’s solution in panel (d) when compared with all the other panels (containing the MD-derived results). To elucidate the origin of the difference, Fig. 4.4(a) shows the PMF divided by the angular factor $\sin(3\theta)$, and averaged over all the angles (details discussed in 4.1). This plot provides a summary of the data in Figs. 4.2(d,e,f) and allows a cross-sectional view of the variation of the field magnitude with distance from the center of the nanobubble. Direct inspection shows that the averaged MD data follows Hencky’s prediction inside the bubble nearly all the way to the edge, at which point the PMF derived from the atomistic simulations swerves sharply upwards, changes sign, and returns rapidly to zero within one lattice spacing beyond the bubble edge (the curve derived from Hencky’s model terminates at the edge, by construction). This effective sectional view explains why the density plots in Figs. 4.2(c,d) seem to have an overall sign mismatch: in the MD-derived data, the plots of the PMF distribution are dominated by the large values at the edge which have an opposite sign to the field in the inner region. Fig. 4.4(a) shows that, rather than a discrepancy, there is a very good agreement between the strain field predicted by Hencky’s solution and a fully atomistic simulation throughout most of the inner region of the nanobubble. However, since Hencky’s solution assumes fixed boundary conditions at the edge (zero deflection, zero bending moment) (Fichter, 1997), it cannot capture the sharp bends expected at the atomic scale generated by the clamping imposed in these particular MD simulations (in effect, corresponding to zero deflection and its zero derivative). The finite bending stiffness of graphene (Wei et al.,

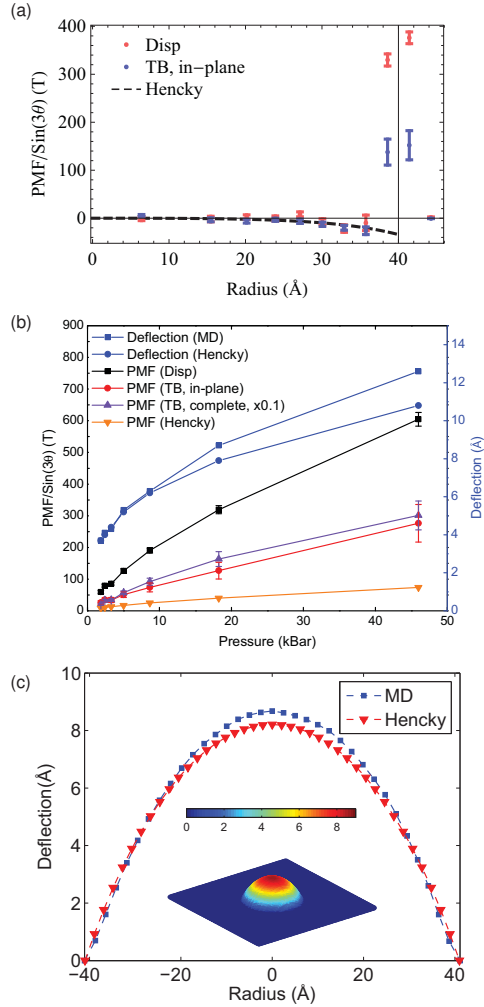


Figure 4.4: (a) Angular-averaged values of $B/\sin(3\theta)$ for the circular nanobubble with $R = 4 \text{ nm}$ considered in Fig. 4.2. The different datasets correspond to different strategies discussed above to obtain the PMF. The vertical line at $r = R \approx 40 \text{ \AA}$ marks the radius of the circular aperture in the substrate. For $r < R$ the results extracted from MD closely follow the analytical curve, but there is a sharp sign change and increase at $r \approx R$ (see 4.1 for details of the averaging procedure, as well as for the TB data including the full hopping perturbation). (b) Comparison between the pressure-induced deflection and maximum PMF magnitude at the edge, $|B(R \approx 40 \text{ \AA})|$, obtained with the different approximations discussed in the text. The points corresponding to the complete TB hopping are scaled by 0.1 for better visualization. (c) A section of the simulated nanobubble (MD) at $\sim 19 \text{ kBar}$ and the corresponding Hencky's solution (the inset shows a 3D perspective of the former with the color scale reflecting the vertical displacement).

2013) comes into play in that region, generating additional strain gradients which explain the profile and large magnitude of the PMF seen in the atomistic simulations. In Fig. 4-4(b) the evolution of the deflection and maximum PMF with increasing gas pressure are plotted. The maximum PMF is obtained around the edge of the aperture, and the values shown in the figure correspond to an angular average of the PMF amplitude there (see 4.1 for details). The MD and analytical (Hencky's) solutions give comparable results for the deflection in the pressure range below $< 1 \times 10^4$ bar (Fig. 4-4(b), right vertical scale). At higher pressures, Figs 4-4(b) and 4-4(c) show that the analytical solution yields a slightly smaller deflection, as the underlying model does not capture the nonlinear elastic softening that has been observed in graphene in both experiments (Lee et al., 2008) and previous MD simulations (Jun et al., 2011). Fig. 4-4(b) includes also the maximum PMFs occurring at the bubble edge, when computed with the different approaches discussed above in connection with Figs 4-2(c-f). Note that Hencky's solution cannot generate significant PMFs even at the largest deflections, whereas experiments in similarly sized and deflected nanobubbles easily reveal PMFs in the hundreds of Teslas (Levy et al., 2010; Lu et al., 2012). This raises questions about the applicability of the Hencky solution at these small scales and large deflections. The pressure required to rupture this graphene bubble was determined to be around 1.9×10^5 bar from the MD simulations. Such a large value is required because of the small dimensions of the bubble. The fracture stress can be calculated by adopting a simple model for a circular bulge test, *i.e.*, $\sigma \sim \frac{R\delta P}{2w}$, where σ , δP , R , and w are the stress, pressure difference, radius, and thickness of the membrane, respectively. Assuming w to be 3.42 \AA , a fracture strength of about 80 GPa is obtained, which is in agreement with previous theoretical (Zhao and Aluru, 2010) and experimental (Lee et al., 2008; Zhao and Aluru, 2010) results. Note that the plot in Fig. 4-4 shows very large pressures (up to near the rupture limit

of the bubble) and correspondingly large deflections since it is to highlight the points of departure between the elastic model and the simulation results. Pressures and deflections considered in the specific cases discussed below are considerably smaller. With the good performance of the atomistic model on the circular graphene bubble established, next the analysis is extended to nanobubbles with different shapes. The bubbles are similarly obtained by inflation of graphene under gas pressure against a target hole in the substrate with the desired shape. Fig. 4-5 shows results of a study of different shapes to which the displacement approach was applied to obtain the strain field and, thus, the PMFs. The shapes are a square, a rectangle (aspect ratio of 1:2), a pentagon, a hexagon, and a circle, and are presented in order of approximately decreasing symmetry. Those geometries were chosen because they are sufficiently simple that they can be readily fabricated experimentally with conventional etching techniques. The dimensions of the different bubbles were chosen such that their areas were approximately $\sim 50 \text{ nm}^2$. The pressure was 19000 bar and side lengths for the bubble geometries shown in Figs. 4-5(a)-4-5(f) were, respectively, 4 nm (circle), 4.4 nm (hexagon), 5.7 nm (pentagon), 5 nm (rectangle, short edge), 7.1 nm (square), 10.6 nm (triangle).

It is worth emphasizing that these features depend on the orientation of the graphene lattice with respect to the substrate aperture, as expected. This is clearly visible in the case of the square bubble in Fig. 4-5(e), for which the sharp magnetic field along the boundary is present along the horizontal (zigzag) edges of the bubble but not along the vertical ones (armchair). This is also the reason why only the triangular aperture shown in Fig. 4-5(f) leads to a strong PMF that is nearly uniform as one goes around the boundary of the nanobubble. This is an important consideration for the prospect of engineering strained graphene nanostructures capable of guiding or confining electrons within, much like a quantum dot (Qi et al., 2013). The sharp

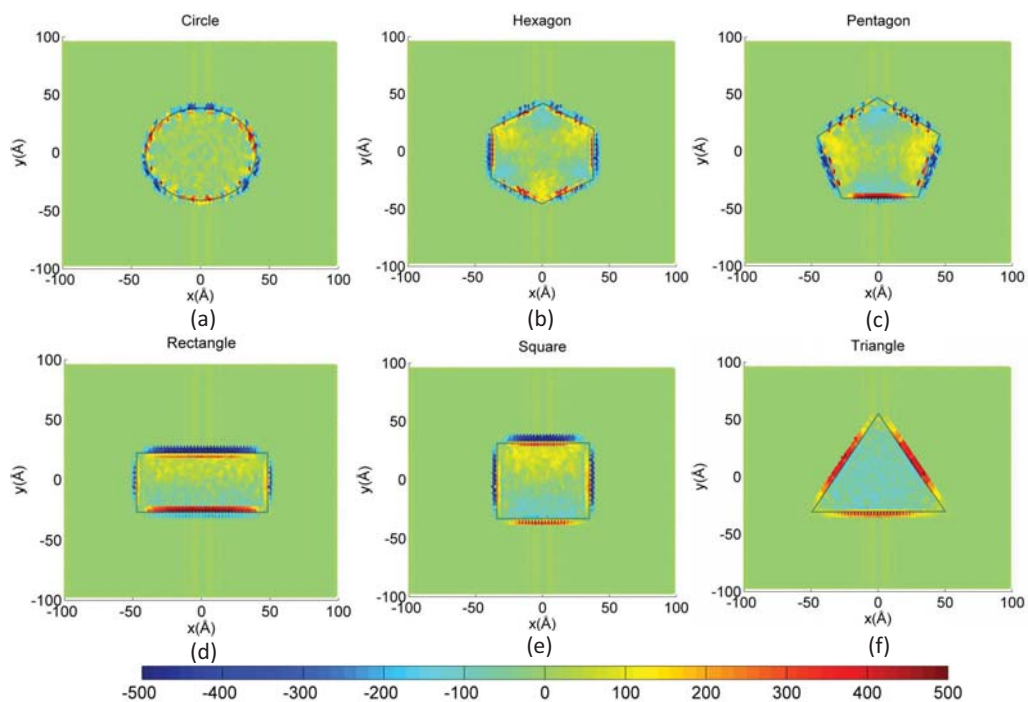


Figure 4-5: Top views of PMF patterns for graphene bubbles of different geometries without substrate. (a) circle (b) hexagon (c) pentagon (d) rectangle (aspect ratio 1:2) (e) square (f) triangle. All the bubble areas are $\sim 50 \text{ nm}^2$, and side lengths and pressures can be found in the text. In all cases, the graphene lattice is oriented with the zigzag direction along the horizontal. The same color scale (in Tesla) is used in all panels. The edge of the substrate apertures used in the MD simulations is outlined (gray line) for reference.

PMF at the boundary acts effectively as a strong magnetic barrier, which might be tailored to confine some of the low energy electronic states (De Martino et al., 2007; Masir et al., 2009; Klimov et al., 2012). The resulting PMF patterns in Fig. 4-5 show that the highest values are found at the corners and edges of the different bubble shapes. To illustrate more clearly the PMF patterns, the bubbles are inflated to large deflections (~ 1 nm) with strains reaching 10% and the corresponding pressure exceeding 1×10^4 bar. These large deflections explain why the PMF magnitudes in Fig. 4-5 may reach over 500 T. Given that the gas pressures used to achieve the results shown in this figure are rather high, some comments are in order. First, it is worth emphasizing that the relevant parameter is the deflection, rather than the pressure itself. In other words, gas pressure was employed here as *one* way of generating graphene nanobubbles with predefined boundary geometries and target deflections, but other loading conditions might be used to achieve the same parameters. This choice is motivated by the desire to constrain graphene and its interaction with the substrate as little as possible. Since it is intended to reproduce bubbles with lateral size and deflections matching the magnitude of the values observed experimentally (Levy et al., 2010; Lu et al., 2012) this requires large pressures (for a given target deflection P is naturally smaller for larger apertures).

Second, a previous study (Lu et al., 2012) reported that experimental bond elongations, estimated from direct STM mapping of the atomic positions and deflections, can exceed 10% in graphene nanobubbles on Ru. The high pressures considered in the MD simulations allow us to reach bond elongations of this order of magnitude.

Third, pressures of the order of 10 kbar (1 GPa) have been recently estimated to occur within nanobubbles of similar dimensions and deflections to the ones considered here, formed upon annealing of graphene-diamond interfaces (Lim et al., 2012). Thus, pressures of this magnitude are not unrealistic in the context of nanoscale graphene

blisters.

4.3 Substrate interaction: Graphene on Au (111)

After the ideal case of graphene without a substrate, a more realistic case of graphene lying on an Au(111) substrate is studied. The main difference is that the carbon atoms are not rigidly attached to the substrate anymore outside the aperture, meaning that graphene can slide into the aperture during inflation, subject to the interaction with the substrate. This is an important qualitative difference, and reflects more closely the experimental situation, as recently reported in reference (Kitt et al., 2013a). The interatomic interactions were parameterized with $\epsilon_{C-Au}=0.02936$ eV, $\sigma_{C-Au}=2.9943$ Å (Piana and Bilic, 2006); $\epsilon_{C-Ar}=0.0123$ eV, $\sigma_{C-Ar}=3.573$ Å (Tuzun et al., 1996); $\epsilon_{Ar-Ar}=0.0123$ eV, $\sigma_{Ar-Ar}=3.573$ Å (Rytken et al., 1998); the Ar-Au (gas-substrate) interactions were neglected to save computational time, and the substrate layer was held fixed for the entire simulation process. Most of the graphene layer was unconstrained, except for a 0.5 nm region around the outer edges of the simulation box where it remained pinned. Since the interaction with the substrate is explicitly taken into consideration, this approach realistically describes the sliding and sticking of graphene on the substrate as the gas pressure is increased, as well as details of the interaction with the substrate in and near the hole perimeter.

The discussion starts with a direct comparison of the deformation state of a circular bubble obtained from the simulations with the predictions of a recently developed and experimentally verified ‘extended-Hencky’ model (Kitt et al., 2013a) that accounts for the same sliding and friction effects. As can be seen in Fig. 4-6(a), after fitting the friction in the continuum model to the MD simulation there is a very good agreement between the MD and extended Hencky results for the radial and tangential strains, ϵ_{rr} and $\epsilon_{\theta\theta}$, both in the inner and outer regions with respect to the substrate

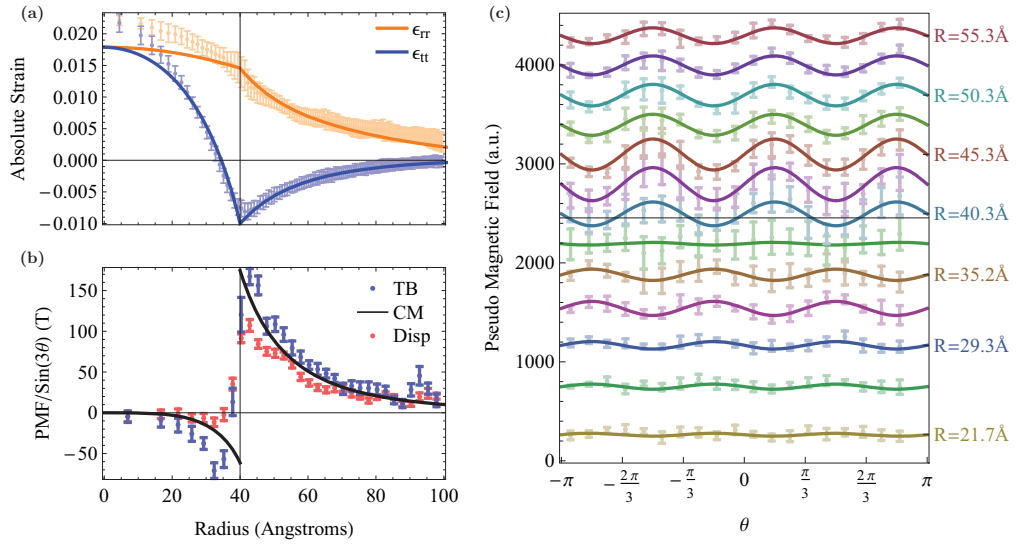


Figure 4-6: (a) Strain components ϵ_{rr} and $\epsilon_{\theta\theta}$ of a graphene bubble pressurized to a deflection of ~ 1 nm against a circular hole with 4 nm radius on a Au(111) substrate. (b) The corresponding PMF along the radial direction from the bubble center computed according to the extended Hencky model (Kitt et al., 2013a) (solid line) and from MD simulations within the TB (blue) or displacement (red) approach. Panel (d) shows the angular dependence of the PMF for selected radii.

aperture. The same good agreement is seen in the PMF profile extracted from the MD and analytical approaches, which is presented in Fig. 4-6(b). The numerical data points shown in this panel represent an angular average over an annulus centered at different radii.

An important message from Fig. 4-6(b) is that the maximum magnitude of the PMF occurs around the edge of the aperture, but on the outside of the bubble. Whereas one expects the maximal PMFs to occur around the edge where the strain gradients are larger, the fact that the magnitude is considerably higher right outside rather than inside is not so obvious. This has important implications for the study of PMFs in graphene nanostructures but has been ignored by previous studies. It implies that models where only the deflection inside the aperture is considered (such as the simple Hencky model) can miss important quantitative and qualitative features. They are captured here because the friction and sliding effects due to graphene-substrate interactions are naturally taken into account from the outset. One consequence is the “leakage” of strain outside the bubble region and the concurrent emergence of PMFs outside the aperture. This should be an important consideration in designing nanoscale graphene devices with functionalities that rely on the local strain or PMF distribution.

The other shapes studied on the Au(111) substrate are shown in Fig. 4-7. The dimensions are the same as in Fig. 4-5, with an applied pressure of ~ 30 kbar. In addition to the appearance of non-negligible PMF outside the aperture region, a comparison with the data for bubbles clamped to the hole perimeter shows that now the PMF distribution inside is noticeably perturbed, and that the large field magnitudes observed in Fig. 4-5 along the perimeter are considerably reduced and smoother.

To understand the origin of this difference, detailed analysis should be done for the

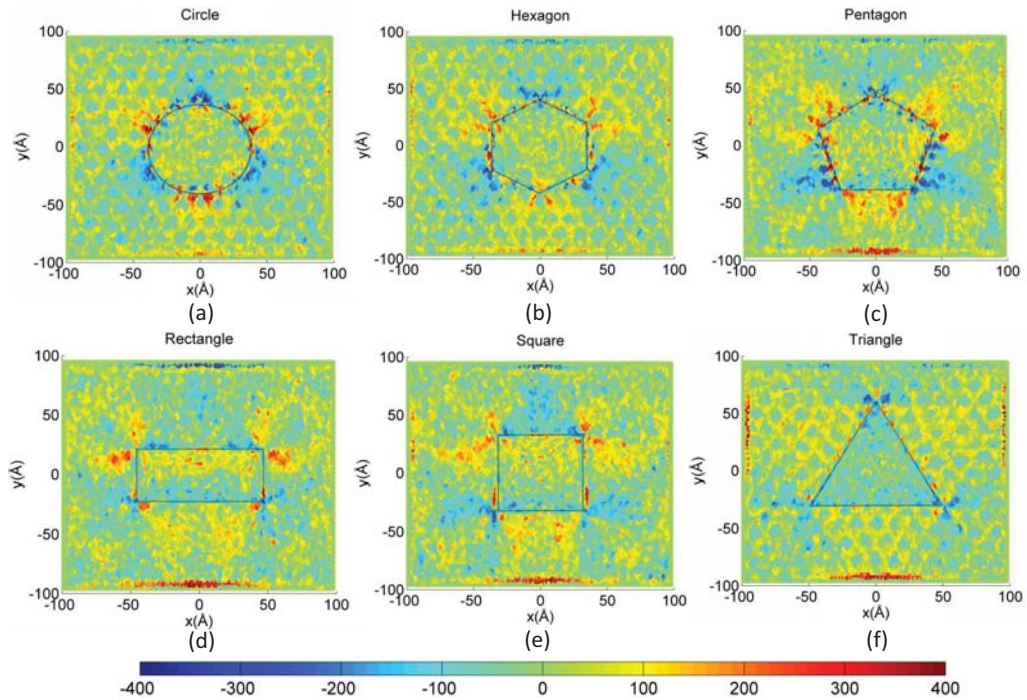


Figure 4.7: Top views of PMF patterns for graphene bubbles of different geometries on Au(111) substrates. (a) circle (b) hexagon (c) pentagon (d) rectangle (aspect ratio 1:2) (e) square (f) triangle. All the bubble areas are $\sim 50 \text{ nm}^2$, and side lengths and pressures can be found in the text. In all cases, the graphene lattice is oriented with the zigzag direction along the horizontal. The same color scale (in Tesla) is used in all panels. The edge of the substrate apertures used in the MD simulations is outlined (gray line) for reference.

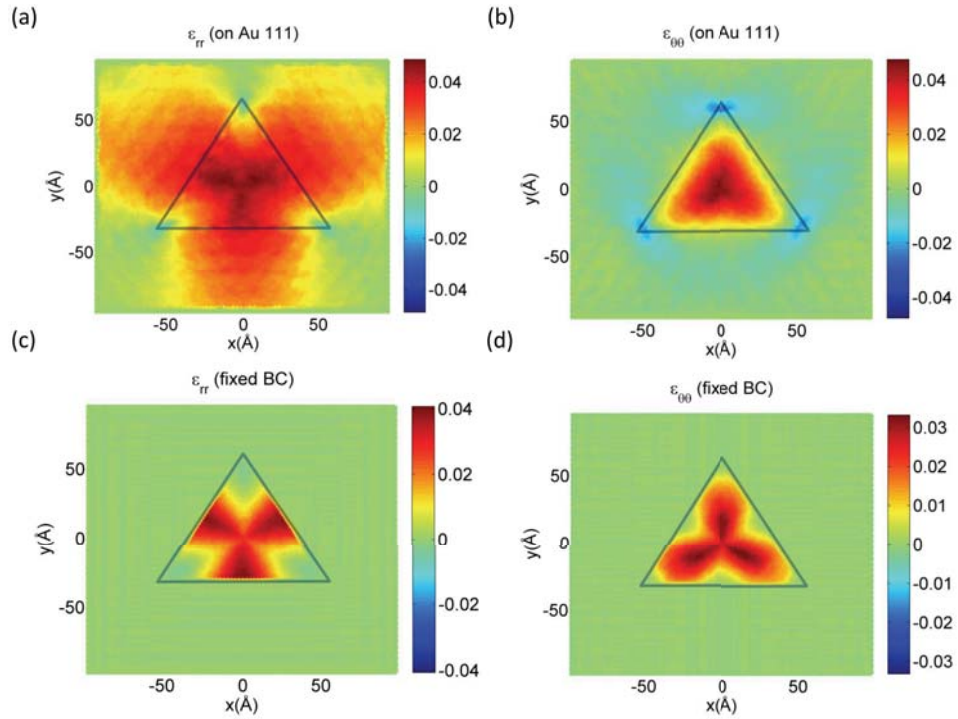


Figure 4-8: Spatial patterns of the strain tensor components ϵ_{rr} and $\epsilon_{\theta\theta}$ for a triangular bubble with a 10.6 nm side. (a) and (b) pertain to graphene on a Au (111) substrate whose PMF profile has been shown in Fig. 4-5(f), while (c) and (d) correspond to the graphene bubble with an artificially fixed boundary condition whose PMF is shown in Fig. 4-7(f). The edge of the substrate aperture used in the MD simulation is outlined (gray line) for reference.

representative case of a triangular nanobubble, as previous experiments have shown that such nanobubbles can exhibit PMFs in excess of 300 T (Levy et al., 2010). Using the MD-based simulation approach, the PMFs for triangular graphene bubbles were calculated by inflating a graphene monolayer through a triangular hole in the substrate. The set-up is as illustrated in Fig. 4-1, but with the circular hole replaced by a triangular one. The triangular hole in the substrate had a side length of 10.6 nm, and the graphene sheet was inflated to a deflection of ~ 1 nm.

The resulting PMF distribution when one artificially clamps graphene outside the hole region has been shown in Fig. 4-5(f); the underlying strain components can be seen in Figs. 4-8(c,d). Upon inflation under the gas pressure, the geometry and the clamped conditions enforce an effective tri-axial stretching in the graphene surface that is clearly visible in the strain distribution. As pointed out by previous study (Guinea et al., 2010b), this tri-axial symmetry is crucial for the experimental observation of Landau levels in reference(Levy et al., 2010) because it leads to a quasi-uniform PMF inside the nanobubble. Inspection of Fig. 4-5(f) confirms that the field is indeed of significant magnitude and roughly uniform within the bubble. When the full interaction with the substrate is included and the graphene sheet is allowed to slip and slide towards the aperture under the inflation pressure, the geometry is no longer as effective as before in generating a clear triaxial symmetry: a comparison of the top and bottom rows of Fig. 4-8 shows that the triaxial symmetry of the strain distribution is not so sharply defined in this case. Therefore, the finite and roughly uniform PMF inside the triangular boundary that is seen clearly in Figs. 4-5(f) is largely lost here.

To understand the difference, note that the orientation of the triangular hole with respect to the crystallographic axes used here is already the optimum orientation in terms of PMF magnitude, with its edges perpendicular to the $\langle 100 \rangle$ directions

(*i.e.*, parallel to the zigzag directions). Further, since the graphene sheet is allowed to slide, the strain distribution in the central region of the inflated bubble tends to be more isotropic, as expected for an inflated membrane because of the out of plane displacement, and as can be seen in Fig. 4·8. This means that the trigonal symmetry imposed on the overall strain distribution by the boundaries of the hole is less pronounced near the center. As a result, even though strain increases as one moves from the edge towards the center (as measured, for example, by looking at the bond elongation directly from the MD simulations), the magnitude of the PMF decreases because the trigonal symmetry and strain gradients become increasingly less pronounced and recall that the isotropic (circular) hole yields zero PMF at the apex (Fig. 4·2). The differences in trend and the sensitivity of the PMF distribution to the details of the interaction with the substrate highlight the importance of the latter in determining the final distribution and magnitude of the PMF, in addition to the loading, hole shape, and boundary conditions. In order to stress this aspect, and to make the role of the substrate interaction even more evident, a different metal surface needs to be considered.

4.4 Substrate interaction: Graphene on Cu (111)

To gain further insight into the important effects of substrate interactions, simulations were carried out for a Cu (111) substrate, in addition to the Au (111) case considered above. This is in part motivated by a recent experimental study (He et al., 2012) showing that graphene grown by chemical vapor deposition (CVD) on a Cu(111) substrate is under a nonuniform strain distribution. This nonuniform strain suggests that there might be interesting PMFs in the region of graphene surrounding the bubble. To analyze that the PMF profile generated by the inflation of a graphene bubble constrained by a circular aperture was studied with a radius of 4 nm on a

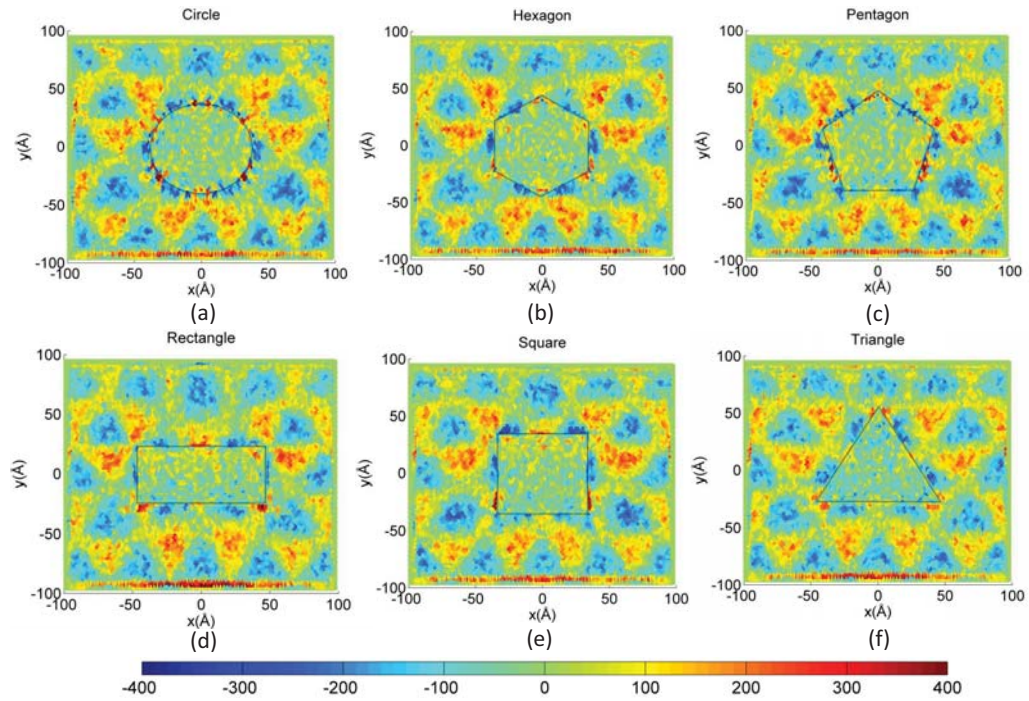


Figure 4-9: Top views of PMF patterns for graphene bubbles of different geometries on Cu(111) substrate. (a) circle (b) hexagon (c) pentagon (d) rectangle (aspect ratio 1:2) (e) square (f) triangle. All the bubble areas are $\sim 50 \text{ nm}^2$, and side lengths and pressures can be found in the text. In all cases, the graphene lattice is oriented with the zigzag direction along the horizontal. The same color scale (in Tesla) is used in all panels. The edge of the substrate apertures used in the MD simulations is outlined (gray line) for reference.

Cu(111) substrate. The Cu-C interactions were modeled using a Morse potential with parameters $D_0=0.1$ eV, $\alpha=1.7$ Å, $r_0=2.2$ Å, and a cutoff radius of 6 Å (Maekawa and Itoh, 1995). Fig. 4.9 shows the PMF distributions for differently shaped bubbles with deflection of ~ 1 nm on Cu(111) substrate. Despite the similarity between the geometry, dimensions, and deflections of this system and the one studied in Fig. 4.7, this one shows a much more pronounced modulation of PMF in the regions outside the aperture. In the same way that the Moiré patterns seen experimentally in a previous study (He et al., 2012) reflect a non-negligible graphene-Cu interaction, the PMF distributions in Figs. 4.9(a-f) are much richer than in Figs. 4.7(a-f). That this simulation strategy involves pressing graphene against the substrate certainly enhances the interaction and promotes increased adhesion. This, in turn, adds a non-isotropic constraint for the longitudinal displacement and deformation of the graphene sheet which will affect the overall magnitude and spatial dependence of the PMF in the central region in such a way that, for this case, the PMF magnitude is higher outside the inflated portion of graphene, rather than inside or in the close vicinity of the boundary. This shows that the strain and PMF patterns in graphene can be strongly influenced by the chemical nature of the substrate and not just its topography.

To reveal the PMF that is induced by the substrate alone, Fig. 4.10 presents a side-by-side comparison of the PMFs that result when graphene is let to relax on Au(111) and Cu(111), respectively. The plotted data are obtained from energy minimization without pressure or aperture to show the intrinsic effect of the two substrates. Several interesting features emerge from these results, the first of which being the spontaneous development of a superlattice structure with a characteristic and well defined periodicity that is different in the two substrates. This Moiré pattern in the PMF is the result of a corresponding pattern in the strain field throughout the graphene sheet, which is

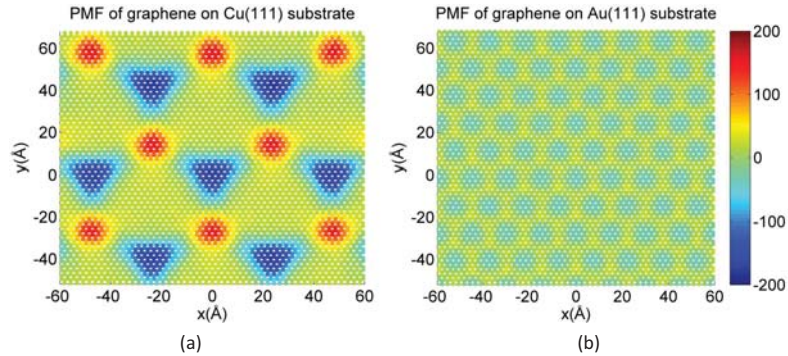


Figure 4-10: PMF distributions of graphene on perfect (a) Cu(111) substrate and (b) Au(111) substrate without apertures nor gas pressure. The superlattice structure arises naturally from the need of the system to release strain buildup because of the mismatch in the lattice parameters of graphene and the underlying substrate. The PMF scale is in units of Tesla.

caused by the need of the system to release strain buildup due to the mismatch in the lattice parameters of graphene and the substrate. A second important aspect is the considerable magnitude of the PMFs that can locally reach a few hundreds of Tesla just by letting graphene reach the minimum energy configuration in contact with the flat metal substrate. Another detail clearly illustrated by these two examples is the sensitivity to the details of the substrate interaction: the substrate-induced PMF on Cu can be many times larger than that on Au, and the Moiré period is also different.

These super-periodicities are expected to perturb the intrinsic electronic structure of flat graphene whose electrons now feel the influence of this additional periodic potential. That leads, for example, to the appearance of band gaps at the edges of the folded Brillouin zone. Such effects are currently a topic of interest in the context of transport and spectroscopic properties of graphene deposited on boron nitride, where this type of epitaxial strain is conjectured to play a crucial role in determining the metallic or insulator character (Woods et al., 2014; San-Jose et al., 2014; Neek-Amal and Peeters, 2014; Jung et al., 2015). Since Fig. 4-10 reveals a

strong graphene-substrate interaction, it is not surprising that the PMF patterns in Fig. 4.9 are still strongly dominated by the substrate-induced PMF. Unlike the cases discussed in Fig. 4.5, a significant structure remains in the PMF distribution outside the hole region due to the tendency of the lattice to relax towards the characteristic Moiré periodicity of Fig. 4.10(a) when in contact with a flat portion of substrate. In contrast, Au(111) has a larger lattice spacing and generates considerably less epitaxial strain in the graphene film, implying comparatively weaker PMFs. It is then natural that in the presence of the nanobubbles the geometry of the aperture dominates the final PMF distribution over the entire system when pressed against Au(111) (Fig. 4.7), whereas for Cu(111) the epitaxial contribution is the one that dominates (Fig. 4.9).

4.5 Bending effects

The large deflection-to-linear dimension ratio in the inflated graphene bubbles analyzed so far calls for an analysis of the relative importance of the contribution to the PMF from bending in comparison with that from the local stretching of the distance between carbon atoms. When full account of stretching and bending is taken by replacing the hopping Eq. 2.7 in the definition of the vector potential \mathbf{A} given in Eq. 2.10 the resulting PMF can have considerably higher magnitudes, as was already seen in Fig. 4.2(f). To isolate the effect of bending alone one can split the full hopping Eq. 2.7 in two contributions, $t_{ij} = t_{ij}^{(xy)} + t_{ij}^{(c)}$, where the “in plane” stretching term is simply

$$-t_{ij}^{(xy)} = V_{pp\pi}(d). \quad (4.2)$$

Since the gauge field \mathbf{A} is a linear function of the hopping Eq. 2.10, it can be likewise split into the respective stretching and bending contributions so that $\mathbf{A} = \mathbf{A}^{(xy)} + \mathbf{A}^{(c)}$. When the PMF associated with $\mathbf{A}^{(c)}$ is thus calculated for the circular bubble of

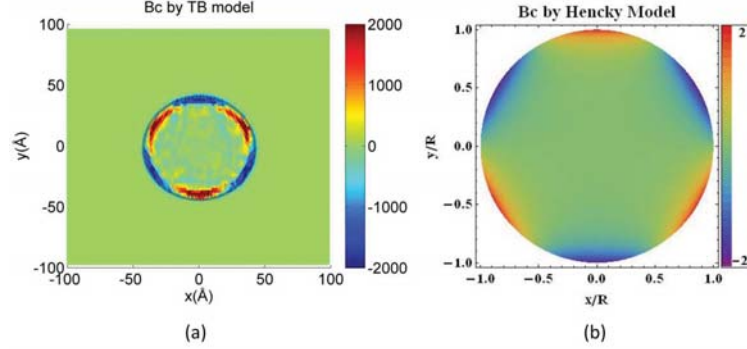


Figure 4.11: Density plot of the bending contribution to the pseudomagnetic field, $B^{(c)}$, for a circular graphene bubble with radius of 4 nm and a deflection of ~ 1 nm calculated by the TB method (a) and Hencky’s model (b). The axes in (b) are scaled in units of the circle radius. The PMF scale is in units of Tesla. The edge of the substrate aperture used in the MD simulation is outlined (gray line) for reference.

Fig. 4.2 the result is obtained shown in Fig. 4.11(a). As was already seen when comparing the different PMF curves in Fig. 4.4, the effect of the curvature at the edges is quite remarkable and overwhelmingly dominant in that region.

More importantly, this fact could have been underappreciated if the stretching and bending contributions had been extracted only on the basis of an analytical solution of the elastic problem such as Hencky’s model. To be definite in this regard, the magnitude of the contribution to the PMF that comes from bending in the continuum limit was considered. If a gradient expansion of the full hopping Eq. 2.7 is performed, the vector potential Eq. 2.10 can be expressed in terms of quadratic combinations of the second derivatives of the deflection $h(x, y)$ (Pereira et al., 2010a). For example, the term $V_{pp\pi}(d) \mathbf{n}_i \cdot \mathbf{n}_j$ in Eq. 2.7 leads to

$$A_x^{(c)} = -\frac{3a^2 V_{pp\pi}^0}{8qv_F} \left[\left(\frac{\partial^2 h}{\partial y^2} \right)^2 - \left(\frac{\partial^2 h}{\partial x^2} \right)^2 \right], \quad (4.3a)$$

$$A_y^{(c)} = -\frac{3a^2 V_{pp\pi}^0}{4qv_F} \left[\frac{\partial^2 h}{\partial x \partial y} \left(\frac{\partial^2 h}{\partial y^2} + \frac{\partial^2 h}{\partial x^2} \right) \right]. \quad (4.3b)$$

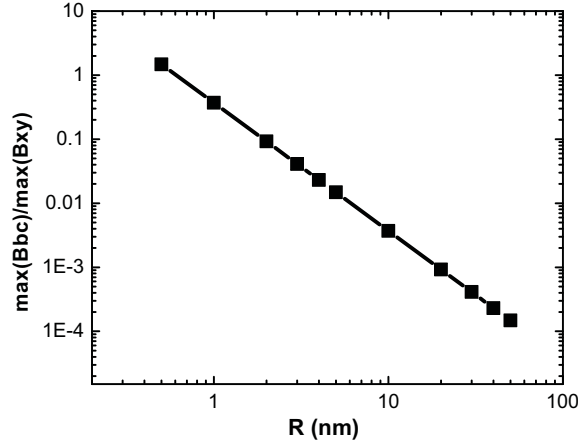


Figure 4.12: Ratio of the maximum PMF induced by bending and stretching (B_c/B_{xy}) for circular graphene bubbles as a function of the graphene radius R , according to Hencky’s solution.

This particular contribution was previously discussed by a previous study (Kim and Castro Neto, 2008) and, since all the bending terms have the same scaling $\sim a^2 h^2 / R^4$, where h and R are the characteristic height and radius, respectively, consideration of this one alone suffices for the purpose of establishing the magnitude of the bending terms in comparison with the stretching one. Replacing the deflection $h(x, y)$ provided by Hencky’s solution in Eq. 4.3 leads to the result shown in Fig. 4.11(b); it is clear that the maximum B_c so obtained at the edges is much smaller than the one derived from the atomistic simulation with the full hopping. It is not surprising that the PMF coming from bending at the level of Hencky’s model is so small. A simple scaling analysis of the vector potentials in the continuum limit shows that, from Eq. 2.11, \mathbf{A}_{xy} scales with strain as $\mathbf{A}_{xy} \sim \epsilon$ and strain itself scales with deflection as $\epsilon \sim (h/R)^2$ for a characteristic linear dimension R of the bubble. On the other hand, from Eq. 4.3 \mathbf{A}_c scales like $\mathbf{A}_c \sim (ah)^2 / R^4$. Therefore, the ratio B_c/B_{xy} will scale as $\sim (a/R)^2$. Since the bubble under analysis has $a/R \approx 0.04$ the bending contribution is indeed expected to be much smaller than the stretching one. It can even be more quanti-

tative and extracts the maximum values of B_c and B_{xy} from Hencky's solution and compare their relative magnitudes as a function of circle radius, as shown in Fig. 4.12. Hencky's solution predicts that only when the radius of the circular bubble decreases below about 1 nm does the contribution of the curvature-induced pseudomagnetic field become of the same order as that due to in-plane stretching. This situation is equivalent to the need to account for the curvature and orbital re-hybridization when describing the electronic structure of carbon nanotubes with diameters below length scales of this same magnitude at the tight-binding level (Blase et al., 1994; Kane and Mele, 1997); the neglect of these effects in the nanotube case leads to incorrect estimation of the band gaps and even of their metallic or insulating character. The problem with these considerations is that they fail to anticipate the large effect at the edges, particularly the scaling analysis which only tells about the relative magnitude of bending *vs* stretching in the central region. But, because graphene is inflated under very high pressures in order to achieve deflections of the order of 1 nm, a sharp bend results at the edge of the substrate aperture through which graphene can bulge outwards; it is this curvature effect that dominates the PMF plot in Fig. 4.11, not the overall curvature of the bubble on the large scale. Hencky's solution cannot capture this since it is built assuming zero radial bending moment at the edge (Fichter, 1997). Moreover, since this happens within a distance of the order of the lattice constant itself, the details of the displacements at the atomistic level including non-linearity and softening at large strains and curvatures become crucial. This further highlights the importance of accurate atomistic descriptions of the deformation fields in small structures such as the sub-5 nm graphene bubbles considered in this thesis, and which have been shown experimentally to lead to significant PMFs (Levy et al., 2010; Lu et al., 2012); at this level models based on continuum elasticity theory can become increasingly limited for accurate quantitative predictions and should be applied with

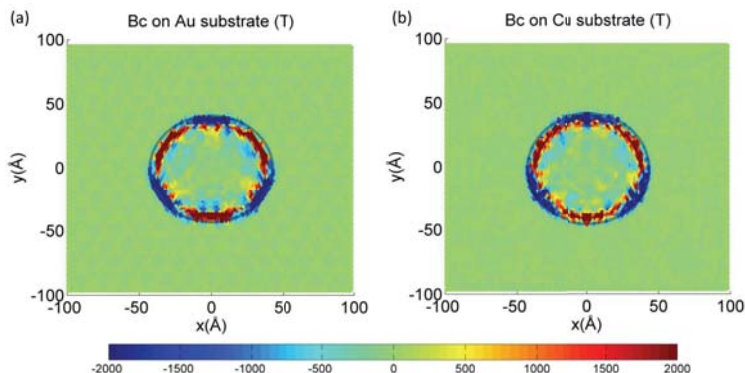


Figure 4-13: Density plot of the bending contribution to the pseudo-magnetic field, $B^{(c)}$, for a graphene bubble deflected to ~ 1 nm upon pressing through a circular aperture of radius 4 nm in a Au (a) and a Cu (b) substrate. The PMF scale is in units of Tesla. The edge of the substrate apertures used in the MD simulations is outlined (gray line) for reference.

caution.

Finally, when realistic substrate conditions are considered, one can see that the slippage effects contribute very differently for the PMFs arising from stretching and from bending. A general feature of the PMF distribution obtained with realistic Au and Cu substrates is its smaller overall magnitude in comparison with the artificially clamped nanobubbles. This is easy to understand because the ability to slide in contact with the substrate allows graphene to stretch not only in the bubble region, but essentially everywhere, thereby reducing the strain concentration around the edge of the aperture; and with smaller strain gradients one gets smaller PMFs. The bending effects, on the other hand, are not expected to be much affected by the sliding, especially when comparing nanobubbles with the same amount of vertical deflection, because the sharpness of the bend at the edge of the aperture is constrained mostly by the geometry alone. Direct inspection of the contribution to the PMF arising from curvature in the Au and Cu substrates directly confirms this intuitive expectation, as shown in Fig. 4-13. Just as in the clamped case where graphene is pinned to the

substrate and cannot slide, the PMF associated with bending is seen to dominate the field distribution, with magnitudes similar to the registered in Fig. 4.11, and much larger than the PMF in the center of the bubble or the substrate region (cf. Figs. 4.7 and 4.9). This not only shows how crucial the PMF associated with bending can be in certain approaches to generate graphene nanobubbles, but also that it is an effect largely insensitive to the details of the substrate.

Chapter 5

Graphene Kirigami

5.1 Simulation setup

Beyond the in-plane deformation imposed on the graphene hexagon, and the out of plane deformation imposed on the graphene bubble, graphene can be deformed and manipulated in other ways. In this chapter, the results of classical MD simulations on the tensile deformation of a specific, experimentally-realized form of graphene kirigami (Blees et al., 2014) is presented. It is demonstrated that the resulting monolayer graphene kirigami can sustain yield and fracture strains that can be more than three times larger than can pristine, bulk graphene. While kirigami has traditionally been applied to increase the flexibility of macroscale structures, here its benefits extend down to single-layer, two-dimensional nanomaterials. Moreover, two non-dimensional design constants are introduced that can be used to tailor and tune the mechanical and electronic properties of the kirigami.

The graphene kirigami were constructed by making cuts in a graphene nanoribbon, which exposed free edges with the resulting kirigami shown schematically in Fig. 5-1. The graphene kirigami in Fig. 5-1 is marked by several key geometric features, which will be described now. First, the length of the nanoribbon is L_0 , while the width is b . The height of each interior cut is w , while the width of each interior cut is c . The distance between successive kirigami cuts is d , while the edge cut length is defined to be half of the interior cut length (i.e. $0.5w$). For simplicity, all of the half cut lengths are the same, while all of the interior cut lengths are also fixed. While the

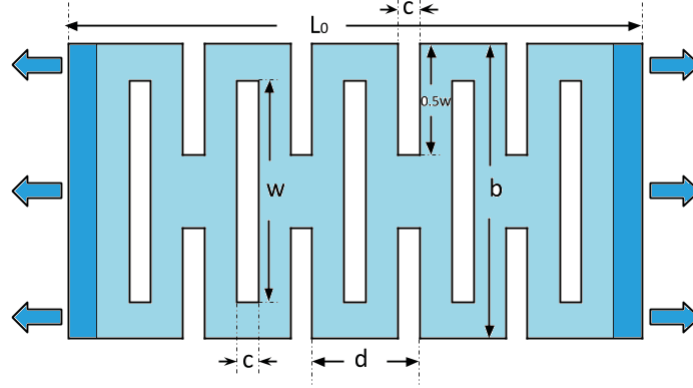


Figure 5.1: Schematic of the graphene kirigami, with key geometric parameters labeled. The kirigami is deformed via tensile displacement loading that is applied at the two ends in the direction indicated by the arrows.

dimensions of the kirigami changed according to the parametric studies performed, a representative kirigami structure studied here had 11408 atoms, $L_0 \sim 340 \text{ \AA}$, $w \sim 67 \text{ \AA}$, $b \sim 100 \text{ \AA}$, $c \sim 5 \text{ \AA}$ and successive kirigami cut distance of $d \sim 48 \text{ \AA}$. The discussion below on the deformation mechanisms and failure process will be based on this specific geometry, though trends in mechanical properties will be reported based on a range of geometric parameters, to be described later.

The kirigami structure was first relaxed for 10 ps within the constant temperature (NVT) ensemble at room temperature (300K). Zigzag chirality was primarily considered, though simulations of armchair graphene were also conducted to verify that the results are qualitatively independent of chirality. Non-periodic boundary conditions were used in three directions. The kirigami was deformed in tension within the same NVT ensemble by applying a uniform displacement loading on both edges, resulting in a strain rate of $\sim 10^9 \text{ s}^{-1}$ until fracture occurred. To illustrate the deformation response, a series of snapshots of the representative stages are shown during elongation in Fig. 5.2 along with the tensile stress strain curve in Fig. 5.3 for the zigzag graphene kirigami configuration illustrated in Fig. 5.1.

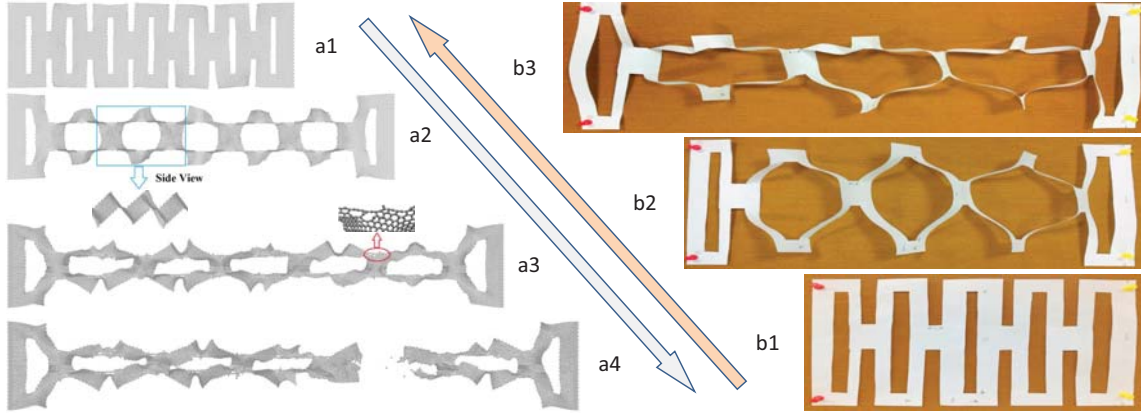


Figure 5.2: Left column: snapshots of the top view (a1-a4) illustrating the deformation stages for zigzag graphene kirigami. A representative yield region is marked in (a3). The tensile strains corresponding to the different stages are 14%, 29%, 56% and 65% respectively. Right column: schematic top view pictures (b1-b3) of similarly patterned paper kirigami for comparison. (b1-b3) correspond to (a1-a3) while paper kirigami fracture picture is not shown. Graphene figures were generated by VMD (Humphrey et al., 1996). *All snapshots were scaled for purposes of simplicity of visualization.*

5.2 Numerical results

Fig. 5.2(a1)-(a4) shows that the graphene kirigami exhibits four distinct stages preceding fracture. Before any tensile loading was applied, the structure rippled out of plane during the initial thermal equilibration stage. Once tensile loading was applied, as shown in (a1), the kirigami structure elongated, with the interior cuts exhibiting tensile elongations of roughly 20% strain along the loading direction. While the interior cuts were initially vertical after the thermal equilibration, during this initial stage of tensile loading (for strains smaller than about 20%), the cuts flipped and rotated such that they make a nearly 45 degree angle with the loading direction, as shown in (a1). This flipping and rotation is the key mechanism that enables the high ductility of graphene kirigami, and during this stage kirigami structure was elongated without significantly stretching carbon bonds. This can be seen from Fig. 5.3 where

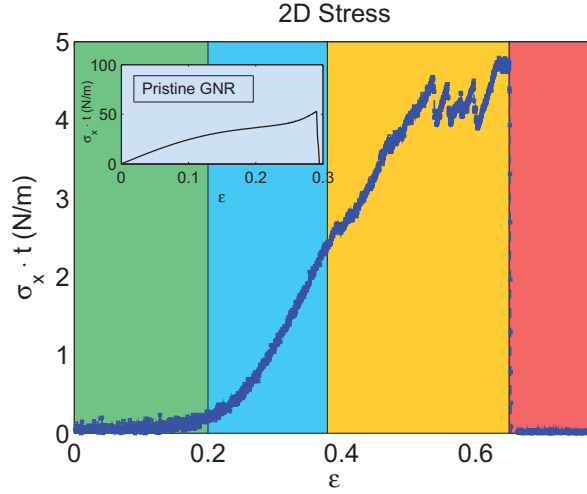


Figure 5-3: Stress-strain curve of the representative graphene kirigami as shown in Fig. 5-2, where the 2D stress was calculated as stress σ times thickness t . Green, blue, orange and red regions correspond to the four stages of deformation discussed in the text and illustrated in Fig. 5-2. A stress-strain curve of a pristine zigzag graphene nanoribbon with the same width is shown in the inset for comparison.

the stress was nearly zero in this stage (green region). In the second stage, shown in (a2), the carbon bonds started to be stretched together with the strained kirigami structure causing the stress increase as shown in Fig. 5-3 for strains between about 20% and 38% (blue region). Note that the deformation in the first two stages, which accounted for nearly 40% tensile strain, was elastic and reversible.

Yielding began in the third stage, as shown in (a3) at a global tensile strain of almost 40%. The yielding initiated from the tips of the interior cuts, as marked in (a3), as those tips exhibited high stress concentrations due to the large deformations. Finally, fracture occurred in the fourth stage at a strain of about 65% in (a4). Armchair graphene kirigami structures were also studied and found similar deformation patterns. Note that (a2) are snapshots before yield while (a3) are after yield in Fig. 5-2.

In order to demonstrate that the atomic scale, single-layer graphene kirigami de-

forms similarly to macroscale kirigami, paper kirigami was created using A4 paper with similar geometric parameters, and subjected to uniaxial stretching as shown in Fig. 5.2(b1-b3). As can be seen, the graphene and paper kirigami exhibited qualitatively similar deformation features, which shows that many of the known advantages of macroscale kirigami may hold even for a single-layer, two-dimensional material. Fracture of the paper kirigami is not shown for preservation purposes.

Having established that kirigami is an effective method to enhance stretchability in graphene, one key challenge is to systematically understand how the geometric parameters of the kirigami shown in Fig. 5.1 impact the key mechanical properties of interest, *i.e.* the yield stress and strain, as well as the fracture strain. Such an understanding will enable experimentalists to design graphene kirigami that possesses a desired combination of mechanical properties. Two dimensionless parameters are defined to characterize the mechanical properties of the kirigami: $\alpha = (w - 0.5b)/L_0$ and $\beta = (0.5d - c)/L_0$. Apparently, the number of cuts will directly affect the mechanical response of the kirigami, and thus these parameter choices are based on the assumption that all cases contain the same number of cuts, namely seven middle cuts and six edge cut pairs for all the cases studied in this thesis as shown in Fig. 5.2.

Verification of the choices for α and β as the appropriate geometric parameters was conducted and shown in Fig. 5.4. To validate the choice of α and β , we conducted simulations with constant α , β values but with varying values of b and w , c and d , respectively to test the validity of the two dimensionless parameters. In Fig. 5.4, it can be seen that for constant α and β , yield strains are essentially constant, which validate the choices made for these constants.

The kirigami structures studied in this thesis contained seven interior cuts and six edge cut pairs. To demonstrate that the results in this thesis are independent of this particular choice of interior and edge cut numbers, simulation with different

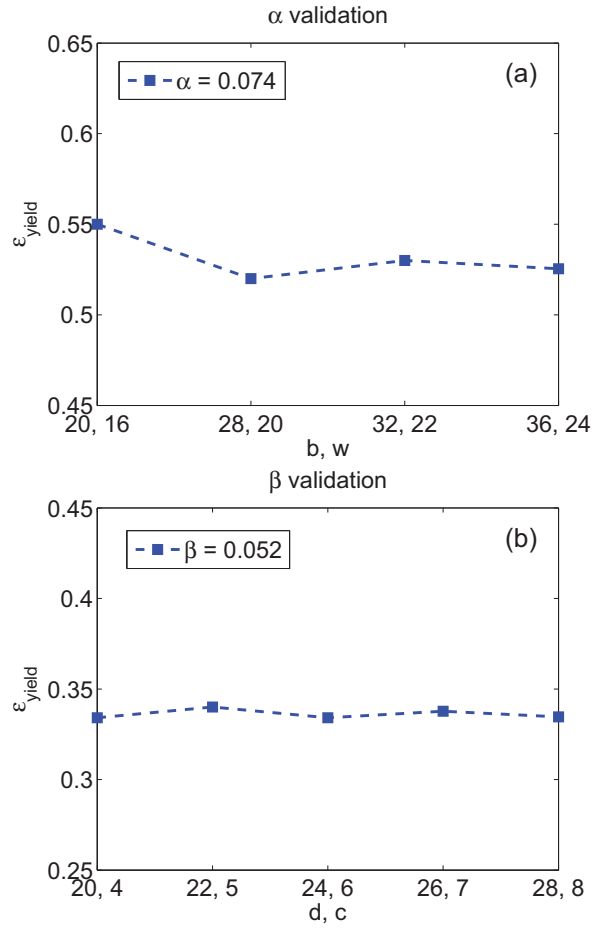


Figure 5-4: (a) α validation with varying w and b , all cases were zigzag with constant $\alpha = 0.074$. (b) β validation with varying d and c , all cases were zigzag with constant $\beta = 0.052$, $L_0 = 115\text{\AA}$.

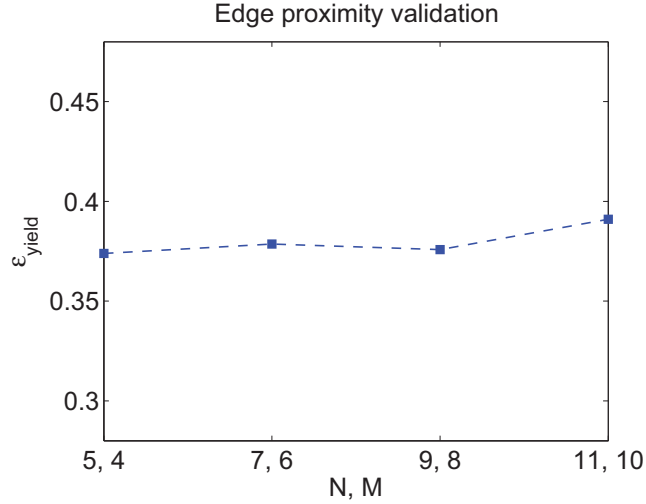


Figure 5-5: Yield strain as a function of interior (N) and edge (M) cut pairs, demonstrating that the choice of 7 interior and 6 edge cut pairs used in this work is representative of the kirigami deformation within the limits of computational capabilities.

of number of cuts were conducted with corresponding length L_0 , while the other geometric parameters b , w , c and d were kept constant. In Fig. 5-5, it shows that yield strains are nearly constant, which shows that within the limits of computational capabilities, the results presented in this work are independent of the number of interior and edge cut pairs.

The first parameter, α , is the ratio of the overlapping cut length to the nanoribbon length, and controls how much the interior cut, and thus the kirigami, can elongate during tensile deformation. Specifically, α affects the yield strain and fracture strain due to the flipping elongation mechanism shown in Fig. 5-2(a2). The yield strain and fracture strain for different values of α are shown in Fig. 5-6. It is clear that for $\alpha > 0$, the kirigami becomes significantly more ductile, where the fracture strain ϵ_{frac} is normalized by the fracture strain for bulk graphene. This is because $\alpha = 0$ corresponds to the configuration when the edge cuts and interior cuts just overlap. When $\alpha < 0$, the edge and interior cuts do not overlap and the flipping and rotation

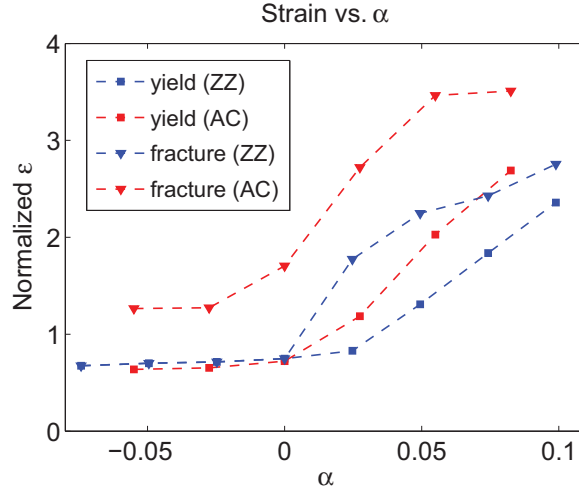


Figure 5-6: Influence of α on yield strain and fracture strain for zigzag and armchair graphene kirigami, for constant $\beta = 0.057$. Data are normalized by graphene nanoribbon results with the same width.

mechanism of Fig. 5-2(a2) and (b2) does not occur. In contrast, when $\alpha > 0$, the flip-rotation mechanism for the interior cuts does occur, and enables the kirigami to expand without substantial stretching of the carbon bonds. This is also reflected from the 2D stress-strain curve as shown in Fig. 5-3, where the stress was calculated as stress times thickness to avoid known controversies in defining the thickness for carbon-based nanostructures (Huang et al., 2006). For completeness, note that for the paper kirigami seen in Fig. 5-2(b1-b3), the non-dimensional values are $\alpha \sim 0.13$ and $\beta \sim 0.06$.

The deformation illustrated in Fig. 5-2(a1) and (b1) corresponds to the green region in Fig. 5-3, where before roughly $\epsilon = 0.2$ the kirigami structure elongates without significant stretching of the carbon bonds, which explains the very low value of stress for that strain region. However, between strains of $\epsilon = 0.2$ to $\epsilon = 0.38$ (yield strain), the carbon bonds begin to be stretched substantially, leading to the increase in stress seen in Fig. 5-3. With a further increase in strain, yielding occurs via local fracture of graphene as shown in Fig. 5-2(a3) and (b3). Eventually, the local fracture

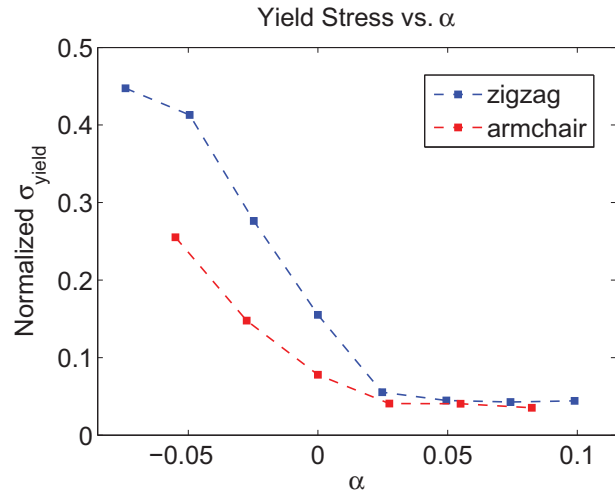


Figure 5-7: Influence of α on the kirigami yield stress, for constant $\beta = 0.057$. Data are normalized by graphene nanoribbon results with the same width.

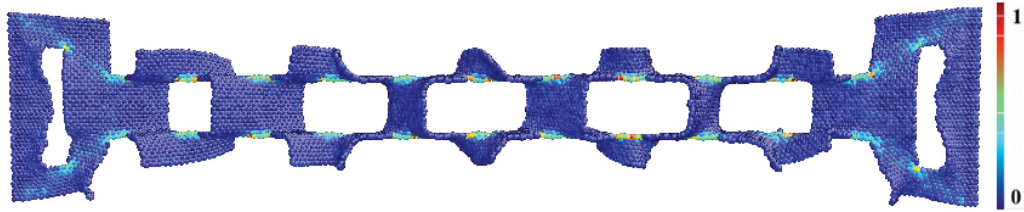


Figure 5-8: Von Mises stress distribution of zigzag graphene kirigami corresponding to the snapshots in Fig. 5-2(a3), where the data was scaled between 0 to 1. Figure was generated by AtomEye (Li, 2003).

propagates and results in global fracture at $\epsilon = 0.65$ as shown in Fig. 5-2(a4) and the red region in Fig. 5-3.

In contrast to the pristine graphene nanoribbon as shown in Fig. 5-3, it is clear that the stress that can be sustained by the kirigami is about one order of magnitude smaller. However, the stretchability, as defined by the fracture strain, is increased by more than a factor of two. Furthermore, the ductility, defined as the strain after yield, is significantly higher for the kirigami, as it can sustain more than 20% elongation after yield, while the pristine graphene nanoribbon fractures immediately after yielding.

While the yield strain increases for increasing α , the opposite trend is observed

for the yield stress, as shown in Fig. 5-7. This is also because for negative α , the middle and edge cuts do not overlap, and thus the kirigami behaves like a cut-free nanoribbon. However, when α is positive, the kirigami deforms like the snapshots shown in Fig. 5-2 and yields due to the tearing mechanism previously described, where the stress distribution prior to yielding is shown in Fig. 5-8.

The graphene kirigami thus fractures quite differently as compared to bulk graphene or a graphene nanoribbon. Instead of brittle fracture, the yielding of graphene kirigami begins from the corners of the interior cuts, and gradually propagates until fracture occurs. The stress distribution in Fig. 5-8 shows that the stress is concentrated at the corners of the interior cuts while being very small in other regions of the kirigami. This stress localization explains why the yield stress curve turns flat after α becomes positive, as shown in Fig. 5-7.

The results shown in Figs. 5-6 and 5-7 were carried out at a constant value of $\beta = 0.057$. While α describes the geometry perpendicular to the tensile loading direction, β describes the geometry parallel to the tensile loading direction. Referring to the kirigami schematic in Fig. 5-1, shows that β represents the ratio of overlapping width to the nanoribbon length, which is directly related to the density of cuts, and where theoretically β can take values ranging from nearly zero to one. However, in practice, when β exceeds about 0.125, the edge atoms between adjacent edge cuts interact and thus break the kirigami structure.

The impact of β on the yield strain is shown in Fig. 5-9 for constant $\alpha = 0.07$. In contrast to α , which describes the length of the overlapping region, β describes the width of the cuts. Furthermore, while the cut length determines how much the kirigami can elongate in along the loading direction, as previously illustrated in Fig. 5-6, the cut width determines the aspect ratio of the overlapping region, which controls the likelihood of the flipping and rotating mechanism previously discussed.

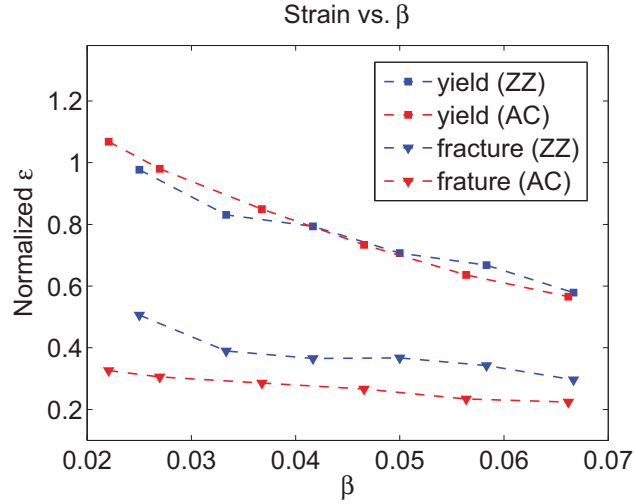


Figure 5-9: Influence of β on fracture strain and yield strain, for constant $\alpha = 0.07$. Data are normalized by graphene nanoribbon results with the same width.

Therefore, Fig. 5-9 demonstrates that when β increases, the overlapping region width increases, which results in increased difficulty for the flipping and rotation mechanism to occur, resulting in a decrease in the yield and fracture strains.

Other than the yield strain, fracture strain and yield stress, other parameters were also studied, including the Young's modulus, toughness and fracture strength for the graphene kirigami. Results for the kirigami geometry in Fig. 5-1 are listed in Table. 5.1, where the Young's modulus was obtained through linear fitting of the stress-strain curve, while the toughness U_T was calculated as $U_T = \int_0^{\epsilon_f} \sigma d\epsilon$. The nature of the stress-strain curve of Fig. 5-3 leads one to define two Young's moduli. The first (E_1) corresponds to the low stress region for strains smaller than $\epsilon = 0.2$ (green) in Fig. 5-3, while the second (E_2) corresponds to the increasing stress region between $\epsilon = 0.2$ and $\epsilon = 0.38$ (blue). Table. 5.1 illustrates that for both armchair and zigzag graphene kirigami, the Young's modulus, toughness and fracture strength are significantly lower compared to either bulk graphene or graphene nanoribbons. Furthermore, though the kirigami structure significantly enhances the

Table 5.1: Young’s Modulus (E), Toughness (U_T) and Fracture Strength (σ_{frac})

Case	E_1	E_2	U_T	σ_{frac}
kirigami(ZZ)	0.80	15.17	1.21	4.73
kirigami(AC)	0.36	11.03	1.12	5.01
nanoribbon(ZZ)	-	295.91	8.27	54.64
nanoribbon(AC)	-	304.70	4.78	43.31
bulk(ZZ)	-	315.53	9.29	67.14
bulk(AC)	-	319.69	5.34	44.93

Note: all results are in unit of N/m. For kirigami (ZZ) cases, $L_0 = 340\text{\AA}$, $b = 100\text{\AA}$, $\alpha \sim 0.05$ and $\beta \sim 0.06$; for kirigami (AC) cases, $L_0 = 347\text{\AA}$, $b = 117\text{\AA}$, $\alpha \sim 0.05$ and $\beta \sim 0.05$.

yield and fracture strains for graphene, the order of magnitude reduction in yield stress and fracture strength results in an overall decrease in toughness for graphene kirigami as compared to pristine graphene.

Besides the single-unit kirigami model above, double-unit models were also studied as shown in Fig. 5-10. These are essentially same as the single-unit models but duplicated in the direction that is orthogonal to the applied strain. These “double-unit” kirigami structures are considered because they have been fabricated experimentally (Blees et al., 2014). Results for the yield and fracture strains of double-unit kirigamis as well as the deformation mechanisms are similar in all aspects to the single-unit kirigami models.

Finally, simulation shows that the large deformations enabled by the kirigami geometry can strongly impact graphene’s electronic properties. In particular, the coupling between mechanical deformation and PMFs have previously been investigated both experimentally (Levy et al., 2010), and theoretically (Guinea et al., 2010b; Qi et al., 2013; Qi et al., 2014). The PMFs of deformed graphene kirigami were calculated at about 17% strain, or before yielding occurs, in Fig. 5-11. The PMFs were calculated using the tight binding method including both in-plane and bending terms, as discussed previously (Qi et al., 2013; Qi et al., 2014). It is evident that signifi-

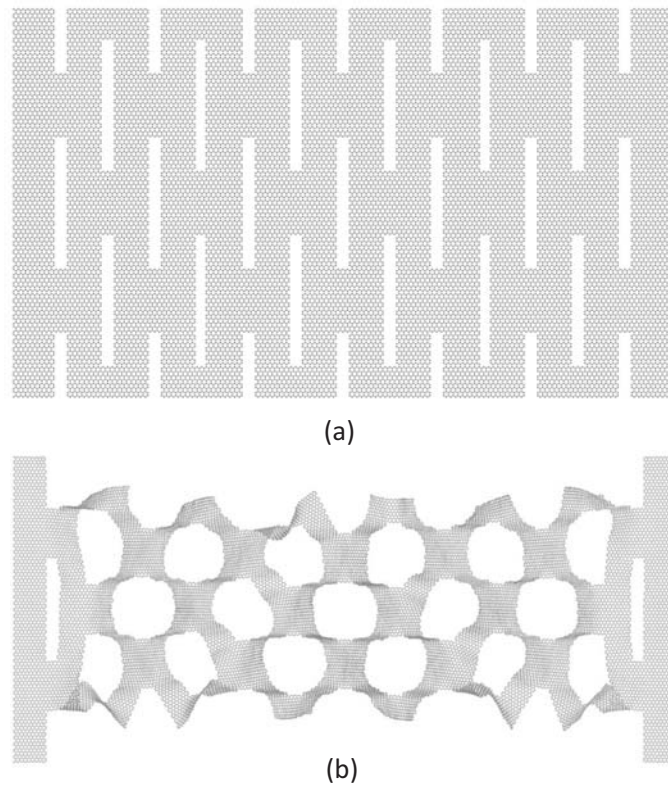


Figure 5-10: (a) Original and (b) deformed ($\epsilon = 0.24$) configuration top-view snapshots of double Y-unit graphene kirigami structures. The geometry parameters are same as the text, Fig. 1, but with twice the width. Figure was generated by VMD (Humphrey et al., 1996). *The snapshots were scaled to same length for visualization purposes.*

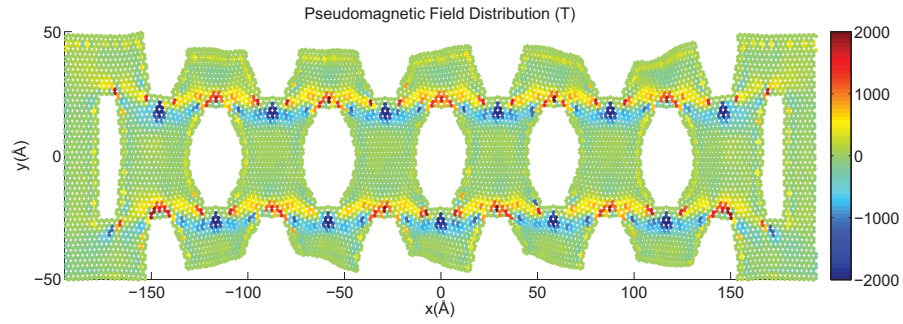


Figure 5.11: Pseudomagnetic field distribution for zigzag graphene kirigami at $\epsilon \sim 0.17$ (i.e. before yield) with $L_0 \sim 340\text{\AA}$, $b \sim 100\text{\AA}$, $\alpha \sim 0.008$, $\beta \sim 0.06$.

cant PMFs can be generated by deforming the graphene kirigami in tension, with the largest magnitudes arising near the sites of highest stress concentration between two kirigami unit cells.

Chapter 6

Mode Coupling in Graphene Nanoresonator

6.1 Simulation setup

While mode-coupling is present in any crystalline membrane, this chapter focuses on graphene due to the many realizations of membrane resonators using this material. To study the intrinsic loss mechanisms in such systems, classical MD simulations and continuum mechanics model (details discussed in sections 2.4 and 2.5) were utilized to systematically investigate the free vibrations of pristine circular graphene monolayers with varying radius, pre-strain, temperature and excitation energy.

After an initial relaxation stage, the graphene monolayer was strained and fixed at its edges. The system was then equilibrated at a specific temperature within the canonical ensemble (NVT) for 10 ps. Thereafter, the monolayer was actuated by assigning an initial velocity profile in the out of plane direction corresponding to the fundamental mode shape of the resonator. After that point, the system was allowed to vibrate freely in the micro canonical (NVE, or energy conserving) ensemble for 5000 ps with a time step of 1 fs. The entire simulation was divided into 10 time windows of 500 ps each; the first 100 ps of each time window were used for further analysis. Specifically, total kinetic energy and velocity history of each atom were recorded to calculate the total kinetic energy spectrum. Four temperatures ($T = \sim 0, 50, 100$ and 300 K), four radii ($R = 5, 7, 9$ and 11 nm) and four initial excitation

energies ($v_{\max} = 2, 5, 10$ and 15 \AA/ps) were studied. Additionally, the pre-strain ϵ_{pre} of the structures was varied.

6.2 Results and discussion

In Fig. 6.1, the time evolution of the kinetic energy spectral density of a circular graphene sheet of radius 5 nm, $\epsilon_{\text{pre}} = 0.5\%$ kept at a temperature of 300 K is reported up to a time of 5 ns. Initially, the FM was excited by a velocity of 10 \AA/ps .

The spectral density of the kinetic energy in Fig. 6.1 corresponds to the frequency distribution of the contribution to the kinetic energy from the out-of-plane motion. The in-plane contribution is negligible in the frequency range relevant for flexural vibrations. The area under a peak gives the kinetic energy of that mode. The prominent peak initially located around $\sim 200 \text{ GHz}$ corresponds to the FM, and its energy decreases continuously during the time evolution. Simultaneously, the frequency of the FM decreases. As the FM frequency is energy-dependent, this suggests that energy is redistributed among normal modes in the system.

This redistribution is known to occur in the problem of coupled Duffing oscillators. In fact, in a continuum mechanics (CM) approach (Eriksson et al., 2013; Atalaya et al., 2008) the present system is also described by a system of coupled Duffing oscillators. In dimensionless form, the equation of motion for the mode amplitudes q_n is written as [see section 2.4]

$$\partial_\tau^2 q_n + \tilde{\omega}_n^2 q_n + \sum_{ijk} W_{ij;kn} q_i q_j q_k = 0. \quad (6.1)$$

The coupling matrix $W_{ij;kn}$ depends only on the geometry of the resonator. For drum geometries it is, in contrast to the FPU case (Lichtenberg et al., 2008), a dense matrix, with permutation symmetry in the indices $i \leftrightarrow j$ and $k \leftrightarrow n$ (Eriksson et al., 2013).

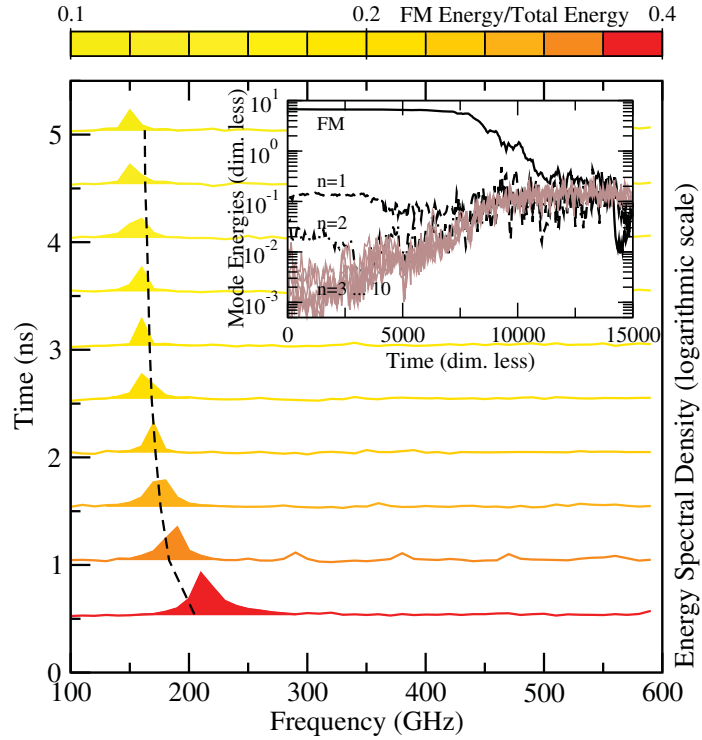


Figure 6-1: Time evolution of the energy spectral density of a circular graphene sheet obtained by MD simulations for the out-of-plane motion. Parameters are given in the text. Note the decay of the FM energy which is indicated by the filled area under the curve, as well as the shift in the FM frequency. The dashed black line is the FM frequency as estimated from the CM model. The inset shows the evolution of the individual mode energies obtained from the CM model in logarithmic scale.

The dimensionless time and energy are related to the physical units through

$$\tau = \frac{\sqrt{\epsilon_{\text{pre}} c_L}}{R} t, \quad \tilde{E} = \frac{E}{2\pi \epsilon_{\text{pre}}^2 c_L^2 \rho_G R^2}, \quad (6.2)$$

where $c_L = \sqrt{Y_{2D}/\rho_G}$ is the longitudinal speed of sound in graphene, with $Y_{2D} \approx 350$ N/m being the two dimensional Young's modulus of graphene (Lee et al., 2008) and $\rho_G = 0.76$ mg/m² the graphene mass density. In deriving Eq. 6.1 the radial coordinate r and the vertical displacement w are scaled according to $\tilde{r} = r/R$, $\tilde{w} = (1/2)w/(\epsilon_{\text{pre}}^2 R)$. The linear frequencies are given by the zeros $\xi_{0,n}$ of the zeroth order Bessel function, $\tilde{\omega}_n = \xi_{0,n}$.

The two models (CM and MD) complement each other. The MD is derived from an atomistic approach, but is computationally heavy and is restricted to relatively small systems. The CM equations are derived assuming negligible bending rigidity and long wavelength deformations, but require less computational power and further allow to predict scaling behaviors for various physical parameters. Since the CM model is a long wavelength approximation, only the low-frequency modes can be accurately described within the model. Additionally, in the CM-simulations presented here only radially symmetric modes are considered, as the interaction term in Eq. 6.1 conserves the radial symmetry of the fundamental mode.

The dimensionless and parameter free form of the CM equations implies that the dynamics is completely determined by the initial conditions. Further, strong mixing in phase space causes the distribution functions of the modes to decouple. The dynamics of the system is then described by the total dimensionless energy \tilde{E} and the ratio of applied FM energy \tilde{E}_0 to total energy, $\eta = \tilde{E}_0/\tilde{E}$. There will also be a dependence on the number of degrees of freedom in the system, set by the number of atoms. In the CM model, this is introduced artificially through the number of modes N that are considered in the simulations. This number is always much smaller than the number

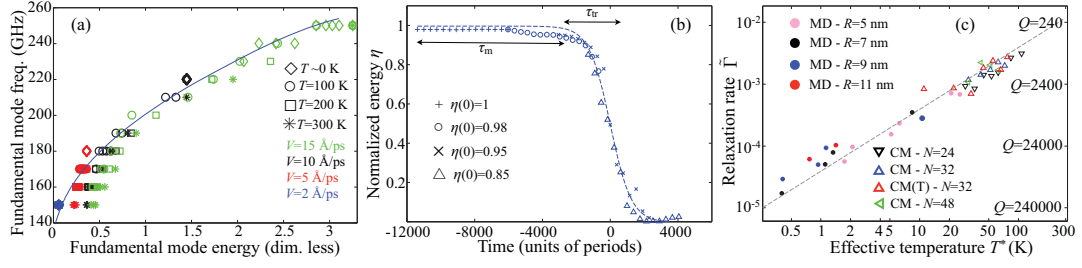


Figure 6.2: (a) Fundamental mode frequency as a function of mode energy. Symbols correspond to MD results, while the full line is the curve predicted from CM. The finite length of the time window used to calculate the frequency spectrum limits the frequency resolution. This is represented by the size of the symbols. (b) Simulation of Eq. 6.1 for a fixed total energy, but with varying initial FM energy. By shifting time, the curves align. The solid line is a fitted sigmoid function used to extract the transition time τ_{tr} . (c) Extracted rates $\Gamma = \tau_{tr}^{-1}$ from MD simulations (filled symbols) and CM (open symbols) for fixed initial value of $\eta = 1/2$ and varying total energy, reported as a function of the effective temperature T^* for fixed $\epsilon_{pre} = 0.2\%$ according to Eq. 6.3. The dashed line corresponds to a linear scaling with T^* .

of atoms in the physical system.

The dimensionless energy can be written in terms of the average energy per atom κ as

$$\tilde{E} = \frac{1}{2\epsilon_{pre}^2} \frac{\kappa}{m_c c_L^2}, \quad (6.3)$$

where m_c is the carbon atom mass. For a system of uncoupled harmonic oscillators in equilibrium, $\kappa = k_B T$. A non equilibrium situation was studied, but an effective temperature may be defined by considering the energy not residing in the FM, $k_B T^* \equiv (E - E_0)/N$ where N is the number of degrees of freedom. The relation in Eq. 6.3 shows the correspondence between temperature and strain in this system. The importance of the mode coupling is determined by the thermal fluctuations of the membrane. These may be enhanced either by increasing the temperature, or by decreasing the strain.

The shift of the FM frequency in Fig. 6.1 can be reproduced in the CM model. In Fig. 6.2(a), the energy dependence of the FM frequency is reported for the MD simulations (symbols), together with the predicted curve from the CM model. The frequency shift is a result of nonlinearities, and the overall agreement indicates that the nonlinearities are well described within the CM model.

Next the dynamics of the FM energy is considered. The inset of Fig. 6.1 shows the temporal evolution of the individual mode energies in the CM model, when initially all energy is fed into the fundamental mode. Note the appearance of an initial metastable state, with nearly all energy localized in the fundamental mode. Among modes with mode number > 3 , the energy is always equipartitioned, indicating that the assumption of strong mixing is valid. These modes define an instantaneous effective temperature of the system, which due to the redistribution increases in time. This effect is more pronounced in the CM-simulations due to the mode number cut-off.

In Fig. 6.2(b) the normalized FM energy η was monitored as a function of time, by calculating the mode dynamics from Eq. 6.1 for a system of $N = 32$ modes for a fixed total energy $\tilde{E} = 3.25$. The degree of initial excitation over the thermal background, i.e. η , was varied in the simulations. Shifting the time, so that $\eta = 1/2$ at $t = 0$, the curves align. This indicates that the important parameters are the total energy and η . Further, two separate time-scales associated with the non-equilibrium dynamics of the system can be identified; initially, when most energy is in the FM, the system relaxes to a long-lived metastable state with energy dependent life-time τ_m . In this region, the system is sensitive to fluctuations and the relaxation is therefore strongly temperature dependent. Thereafter the system undergoes a sharp transition to an equipartition region during a time $\tau_{tr} = \Gamma^{-1}$.

The MD simulations are best suited to investigate the shortest of these timescales, the transition time τ_{tr} . MD simulations were performed at various total energies

with initial data chosen such that the system was initially in the transition stage. The velocity applied to the FM was chosen such that $\eta \approx 1/2$ at the beginning of each simulation. An estimate of the inverse transition time is then given by the (dimensionless) time derivative of the ratio between fundamental and total energy, $\Gamma = \partial_\tau \eta = \xi_{0,0} \partial_t \tilde{E}_0 / \omega_0 \tilde{E}$. This quantity may be considered as an “instantaneous Q-factor” of the resonator. The Q-factors reported here were evaluated at $\eta \approx 1/2$, where the relaxation rate is maximal. If temperature and excitation velocity are changed independently the ratio of fundamental to total energy will also change, which will obscure the scaling of the transition time-scale with energy. To avoid this, the total energy was tuned by changing the pre-strain, employing the duality between temperature and strain apparent from Eq. 6.3. The pre-strains of the structures used in the MD simulations are determined by considering the number of atoms in the resonators and the radius, using further the known value for the graphene bond length obtained from the AIREBO potential (1.396 Å (Stuart et al., 2000)).

The results from the MD simulations (filled symbols) and CM model (open symbols) are compared in Fig. 6.2(c). There is no dependence of the dimensionless relaxation rate on the size of the drum. This is consistent with the observation that the dimensionless energy in Eq. 6.3 does not contain any length scale. The transition rate is linear in energy for both models, i.e. $\Gamma \propto T^*/\epsilon_{\text{pre}}^2$. Note that previous studies on CVD-grown resonators show a power law dependence of the Q-factor on radius (Barton et al., 2011), in contrast to what is reported here. However, for CVD-grown graphene grain boundaries will introduce an additional length scale that determines the mode coupling (Qi and Park, 2012).

The existence of an initial metastable state for initial conditions far from equilibrium is a well known feature of the FPU-problem (Benettin et al., 2008; Fucito et al., 1982; Campbell et al., 2005), and occurs also in other nonlinear lattices (Fucito et al.,

1982) [see section 2.5]. The metastable state is strongly localized in mode space, and is related to so called q-breathers (Flach et al., 2005; Penati and Flach, 2007). The metastable state is obtained when the energy in the FM is much larger than the thermal energy. External losses and thermal noise are expected to destroy this state, but traces of it may be found by considering the relaxation as a function of excitation energy. Numerical evidence on the FPU-chain suggests a stretched exponential dependence of the life-time with excitation energy, $\tau_m \approx \exp(\tilde{E}^{-\alpha})$ (Benettin et al., 1984; Benettin et al., 2008).

The metastable state was probed by initially feeding all energy into the FM, and monitoring the evolution of the FM energy. As the time-scales for the decay of this state is very long compared to the FM oscillations, this state is most readily investigated using the CM model. For the present model, the exponent $\alpha \approx 0.18$ was obtained from CM simulations with $N = 32$ and $N = 40$ modes (see Fig. 6-3). The life-time of the metastable state didn't show a dependence on the number of modes. Note that the exponent α is model dependent (Pettini and Landolfi, 1990), e.g. for the FPU- β -problem $\alpha = 0.25$ has been reported (Berchiolla et al., 2004).

The energy was strongly localized to the FM during the metastable state. The localization of the metastable state in mode space depends on the frequency spectrum. For the drum resonator, the frequencies can be approximated by $\omega_{n,\text{drum}} \approx \xi_{0,0} + n\pi$. In comparison, for small wave numbers the frequencies of the FPU chain are given by $\omega_{n,\text{FPU}} \approx n\pi$ (Berman and Izrailev, 2005). Low frequencies of the FPU chain are almost resonant, and so the formation of a q-breather will consist of a cascade of modes being excited. The present system, being far from resonant, displays a strong localization of energy.

The CM model can make quantitative predictions for the relaxation rate due to energy redistribution in resonators of arbitrary size and tension. As an example, a

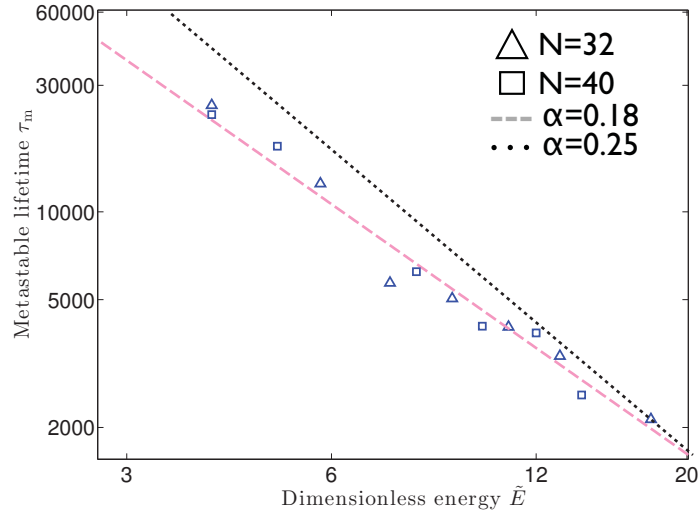


Figure 6-3: Dependence of the metastable lifetime τ_m on system energy, for the CM model with 32 modes (triangles) and 40 modes (squares). The lines corresponds to stretched exponentials of the form $\tau_m \approx \exp(\tilde{E}^{-\alpha})$. The dashed line corresponds to $\alpha = 0.18$, the dotted corresponds to $\alpha = 0.25$.

drum of arbitrary radius, $\epsilon_{\text{pre}} = 0.2\%$ and $T = 4$ K. The relaxation rate can be read off from Fig. 6-2(c), giving a transition time of approximately 24000 oscillations, decreasing to ~ 200 oscillations at 300 K. For this relaxation to be observable, the Q-factor arising from external losses must exceed these values.

Chapter 7

Future Work

Besides the work on graphene hexagon, bubble and kirigami presented in this thesis, there are infinitely many more possible couplings of mechanical deformation graphene's electronic properties. One immediate extension (though non-trivial, particularly within the context of calculating electronic properties in the presence of mechanical strain) is to extend the ideas presented in this thesis to other two-dimensional materials. One important and emerging group of 2D materials is the transition metal dichalcogenides (TMDs), which have the atomic structure of MX_2 , where M denotes a transition metal atom and X denotes a chalcogen atom. As one of the representative TMDs, Molybdenum disulfide (MoS_2) has drawn large amount of interests; while another 2D material that has recently been widely studied is black phosphorus. MoS_2 has sandwich layer and band gap (Mak et al., 2010) which is different from graphene, and it can also be obtained by exfoliation. Black phosphorus also has a band gap (Keyes, 1953) and its puckered lattice structure results in interesting properties like auxeticity (Jiang and Park, 2014). Furthermore, both MoS_2 and black phosphorus's band gaps can be tuned by mechanical strain (Rodin et al., 2014; Conley et al., 2013), which opens new doors for NEMS/MEMS applications. Because of the 2D nature, they can be stacked to make heterostructures adding another dimension to them. This stacking turns out to unveil a lot of more promising engineering applications (Geim and Grigorieva, 2013; Novoselov and Neto, 2012). Therefore, future studies can be carried out to explore the possibility to apply similar

mechanical-electronic approach to simulate MoS₂, black phosphorus and their heterostructures. These future studies rely on appropriate corresponding MD potentials and TB formalism.

Chapter 8

Conclusions

The unparalleled elastic properties of graphene and the unusual response of its electrons to deformations captured by the PMF concept imply that nanostructures deformed with the right symmetry can behave as magnetic quantum dots. Conductance at low E_F is limited to edge state assisted resonant tunneling, and the valley degeneracy can be explicitly broken under an external field, allowing control over which valley assists in the tunneling process. Since B_s can easily reach hundreds of Tesla in experiments (Levy et al., 2010; Lu et al., 2012), such small pseudomagnetic quantum dots are a viable prospect and certainly warrant further investigation.

PMFs in pressure-inflated graphene nanobubbles of different geometries and on different substrates were also investigated, whose configurations under pressure were obtained by classical MD simulations. The geometry of the nanobubbles is established by an aperture of prescribed shape in the substrate against which a graphene monolayer is pressed under gas pressure. The results provide new insights into the nature of pseudomagnetic fields determined by the interplay of the bubble shape and the degree of interaction with the underlying substrate. In particular, comparing nanobubbles inflated in three different substrate scenarios (clamped without substrate, Au(111) and Cu(111)), demonstrates that the graphene-substrate interaction is an essential aspect in determining the overall distribution and magnitude of the strain and the PMFs both inside and outside the aperture region. For example, in atomically flat regions graphene can adhere substantially to the substrate, leading to

sizeable PMFs stemming from epitaxial strain even in the absence of any pressure or substrate patterning. This adhesion varies from substrate to substrate and, in the presence of an aperture or other substrate patterning, perturbs the strain distribution of the nanobubble when compared to a simply clamped edge, thus altering the final PMF profile as well. The magnitude of the separate contributions from bond bending and stretching to the PMF was analyzed as well. In this respect, whereas the overall, large-scale curvature of the graphene sheet leads to significant corrections to the pseudomagnetic field only in ultra-small bubbles with diameter smaller than 2 nm, sharp bends arising from direct clamping or from being pressed against an edge in the substrate aperture result in much stronger PMFs locally, which remain in considerably larger systems. In these cases, the bending contribution to the PMF can be many times larger than the stretching counterpart, leading to a PMF distribution dominated by large values near the edges of the substrate apertures. Furthermore, if bending is (or can be) neglected, it has been established that an approximate *displacement* approach is adequate to obtain the strain tensor and accurate values of the pseudomagnetic fields from MD simulations, when compared with a direct *tight-binding* approach where the modified hoppings are considered explicitly.

As alternative way of patterning and deforming graphene, a systematic study of an experimentally-realized form of graphene kirigami was performed. In doing so, two key geometric parameters are identified that can be tuned to controllably and predictably tailor the mechanical properties of graphene kirigami. Of particular interest, the kirigami structures were found to exhibit yield and fracture strains that can be more than three times that of bulk graphene or graphene nanoribbons. These simulations demonstrate that the benefits of kirigami patterning, which have been exploited for macroscale structures, may also hold in the thinnest possible nanostructures. It is therefore expected that these kirigami structures may prove to be extremely useful in

ameliorating the known brittle behavior of graphene nanostructures, and to provide new methods for producing novel strain engineered graphene devices.

Energy dissipation in a mechanical graphene nanoresonator was systematically studied. For pristine graphene, the redistribution of energy in graphene resonators due to nonlinear mode coupling was investigated numerically in a ring-down setup. This coupling is a limiting factor for the stability of excitations of individual modes. At low temperatures, evidence was found for a state akin to the metastable state found in the FPU problem. After a time increasing exponentially with inverse excitation energy, the system relaxes toward its equilibrium with an energy-dependent rate. The rate of relaxation from a strong non-equilibrium situation with all energy in the FM to a situation close to equipartition depends only on the dimensionless energy of the resonator, which in turn depends on temperature and strain through the ratio $T^*/\epsilon_{\text{pre}}^2$, but not on resonator size. The Q-factors obtained are comparable in magnitude to experimentally observed Q-factors (Eichler et al., 2011). Therefore, it should be possible to experimentally verify the proposed mechanisms. Since the system is closed, the rates reported here constitute a lower bound on the dissipation of graphene resonators. Many applications of nanomechanical systems rely on high Q-factors (Ilic et al., 2004; LaHaye et al., 2004), and therefore an improved understanding of the physical processes limiting this is of fundamental interest. The results demonstrate the possibility of using graphene resonators as a test bed for FPU physics. By this approach long standing questions in non-equilibrium statistical mechanics might eventually be within experimental reach.

References

- Abanin, D. A. and Pesin, D. A. (2012). Interaction-induced topological insulator states in strained graphene. *Physical Review Letters*, 109:066802.
- Abedpour, N., Asgari, R., and Guinea, F. (2011). Strains and pseudomagnetic fields in circular graphene rings. *Physical Review B*, 84:115437.
- Abraham, F. F., Walkup, R., Gao, H., Duchaineau, M., De La Rubia, T. D., and Seager, M. (2002). Simulating materials failure by using up to one billion atoms and the world's fastest computer: Brittle fracture. *Proceedings of the National Academy of Sciences of USA*, 99(9):5777–5782.
- Alder, B. J. and Wainwright, T. (1959). Studies in molecular dynamics. i. general method. *Journal of Chemical Physics*, 31(2):459–466.
- Atalaya, J., Isacson, A., and Kinaret, J. M. (2008). Continuum elastic modeling of graphene resonators. *Nano Letters*, 8(12):4196–4200.
- Bahamon, D. A., Pereira, A. L. C., and Schulz, P. A. (2010). Tunable resonances due to vacancies in graphene nanoribbons. *Physical Review B*, 82:165438.
- Bahamon, D. A., Pereira, A. L. C., and Schulz, P. A. (2011). Third edge for a graphene nanoribbon: A tight-binding model calculation. *Physical Review B*, 83:155436.
- Balandin, A. A., Ghosh, S., Bao, W., Calizo, I., Teweldebrhan, D., Miao, F., and Lau, C. N. (2008). Superior thermal conductivity of single-layer graphene. *Nano Letters*, 8(3):902–907.
- Bambusi, D. and Ponno, A. (2008). Resonance, metastability and blow up in fpu. In *The Fermi-Pasta-Ulam problem*. Springer.
- Barnard, A. W., Sazonova, V., van der Zande, A. M., and McEuen, P. L. (2012). Fluctuation broadening in carbon nanotube resonators. *Proceedings of the National Academy of Sciences of USA*, 109(47):19093–19096.
- Barton, R. A., Ilic, B., van der Zande, A. M., Whitney, W. S., McEuen, P. L., Parpia, J. M., and Craighead, H. G. (2011). High, size-dependent quality factor in an array of graphene mechanical resonators. *Nano Letters*, 11(3):1232–1236.

- Benettin, G., Carati, A., Galgani, L., and Giorgilli, A. (2008). The fermi-pasta-ulam problem and the metastability perspective. In *The Fermi-Pasta-Ulam problem*. Springer.
- Benettin, G., Galgani, L., and Giorgilli, A. (1984). Boltzmann's ultraviolet cutoff and nekhoroshev's theorem on arnold diffusion. *Nature*, 311(5985):444–446.
- Berchialla, L., Giorgilli, A., and Paleari, S. (2004). Exponentially long times to equipartition in the thermodynamic limit. *Physics Letters A*, 321(3):167 – 172.
- Berman, G. P. and Izrailev, F. M. (2005). The fermi-pasta-ulam problem: fifty years of progress. *Chaos*, 15(1):015104.
- Blakslee, O. L., Proctor, D. G., Seldin, E. J., Spence, G. B., and Weng, T. (1970). Elastic constants of compression-annealed pyrolytic graphite. *Journal of Applied Physics*, 41(8):3373.
- Blase, X., Benedict, L. X., Shirley, E. L., and Louie, S. G. (1994). Hybridization effects and metallicity in small radius carbon nanotubes. *Physical Review Letters*, 72:1878–1881.
- Blees, M., Rose, P., Barnard, A., Roberts, S., and McEuen, P. L. (2014). Graphene kirigami. <http://meetings.aps.org/link/BAPS.2014.MAR.L30.11>.
- Bolotin, K. I., Sikes, K., Jiang, Z., Klima, M., Fudenberg, G., Hone, J., Kim, P., and Stormer, H. (2008). Ultrahigh electron mobility in suspended graphene. *Solid State Communications*, 146(9):351–355.
- Branício, P. S. and Rino, J.-P. (2000). Large deformation and amorphization of ni nanowires under uniaxial strain: a molecular dynamics study. *Physical Review B*, 62(24):16950.
- Buehler, M. J., Hartmaier, A., Gao, H., Duchaineau, M., and Abraham, F. F. (2004). Atomic plasticity: description and analysis of a one-billion atom simulation of ductile materials failure. *Computer Methods in Applied Mechanics and Engineering*, 193(48):5257–5282.
- Bunch, J. S., van der Zande, A. M., Verbridge, S. S., Frank, I. W., Tanenbaum, D. M., Parpia, J. M., Craighead, H. G., and McEuen, P. L. (2007). Electromechanical resonators from graphene sheets. *Science*, 315(5811):490–493.
- Bunch, J. S., Verbridge, S. S., Alden, J. S., van der Zande, A. M., Parpia, J. M., Craighead, H. G., and McEuen, P. L. (2008). Impermeable atomic membranes from graphene sheets. *Nano Letters*, 8(8):2458–2462.
- Cadelano, E., Palla, P. L., Giordano, S., and Colombo, L. (2009). Nonlinear Elasticity of Monolayer Graphene. *Physical Review Letters*, 102:235502.

- Cai, J. *et al.* (2010). Atomically precise bottom-up fabrication of graphene nanoribbons. *Nature*, 466:470.
- Campbell, D. K., Rosenau, P., and Zaslavsky, G. (2005). Introduction: The fermi–pasta–ulam problem—the first fifty years. *Chaos*, 15:015101.
- Castle, T., Cho, Y., Gong, X., Jung, E., Sussman, D. M., Yang, S., and Kamien, R. D. (2014). Making the cut: Lattice kirigami rules. *Physical Review Letters*, 113(24):245502.
- Castro Neto, A. H., Guinea, F., Peres, N. M. R., Novoselov, K. S., and Geim, A. K. (2009). The electronic properties of graphene. *Reviews of Modern Physics*, 81(1):109–162.
- Chen, C., Rosenblatt, S., Bolotin, K. I., Kalb, W., Kim, P., Kymissis, I., Stormer, H. L., Heinz, T. F., and Hone, J. (2009). Performance of monolayer graphene nanomechanical resonators with electrical readout. *Nature Nanotechnology*, 4:861–867.
- Choi, S.-M., Jhi, S.-H., and Son, Y.-W. (2010). Effects of strain on electronic properties of graphene. *Physical Review B*, 81:081407.
- Conley, H. J., Wang, B., Ziegler, J. I., Haglund Jr, R. F., Pantelides, S. T., and Bolotin, K. I. (2013). Bandgap engineering of strained monolayer and bilayer mos₂. *Nano Letters*, 13(8):3626–3630.
- Cross, M. C. and Lifshitz, R. (2001). Elastic wave transmission at an abrupt junction in a thin plate with application to heat transport and vibrations in mesoscopic systems. *Physical Review B*, 64:085324.
- Croy, A., Midtvedt, D., Isacsson, A., and Kinaret, J. M. (2012). Nonlinear damping in graphene resonators. *Physical Review B*, 86:235435.
- Datta, S. (1995). *Electronic Transport in Mesoscopic Systems*. Cambridge University Press.
- de Juan, F., Mañes, J. L., and Vozmediano, M. A. H. (2013). Gauge fields from strain in graphene. *Physical Review B*, 87:165131.
- De Martino, A., Dell’Anna, L., and Egger, R. (2007). Magnetic confinement of massless dirac fermions in graphene. *Physical Review Letters*, 98:066802.
- Eichler, A., Moser, J., Chaste, J., Zdrojek, M., Wilson-Rae, I., and Bachtold, A. (2011). Nonlinear damping in mechanical resonators made from carbon nanotubes and graphene. *Nature Nanotechnology*, 6:339–342.

- Eom, K., Park, H. S., Yoon, D. S., and Kwon, T. (2011). Nanomechanical resonators and their applications in biological/chemical detection: nanomechanics principles. *Physics Reports*, 503(4):115–163.
- Eriksson, A., Lee, S., Sourab, A. A., Isacson, A., Kaunisto, R., Kinaret, J. M., and Campbell, E. E. B. (2008). Direct transmission detection of tunable mechanical resonance in an individual carbon nanofiber relay. *Nano Letters*, 8:1224–1228.
- Eriksson, A. M., Midtvedt, D., Croy, A., and Isacson, A. (2013). Frequency tuning, nonlinearities and mode coupling in circular graphene resonators. *Nanotechnology*, 24:39570.
- Farjam, M. and Rafii-Tabar, H. (2009). Comment on “band structure engineering of graphene by strain: First-principles calculations”. *Physical Review B*, 80:167401.
- Fermi, E., Pasta, J. R., and Ulam, S. (1955). Studies of nonlinear problems. Technical report, Los Alamos Scientific Laboratory.
- Fichter, W. B. (1997). Some solutions for the large deflections of uniformly loaded circular membranes. Technical Report 3658, NASA Langley Research Center.
- Flach, S., Ivanchenko, M. V., and Kanakov, O. I. (2005). q -breathers and the fermi-pasta-ulam problem. *Physical Review Letters*, 95:064102.
- Frenkel, D. and Smit, B. (2001). *Understanding molecular simulation: from algorithms to applications*. Academic Press.
- Fucito, F., Marchesoni, F., Marinari, E., Parisi, G., Peliti, L., and Ruffo, S. (1982). Approach to equilibrium in a chain of nonlinear oscillators. *Journal de Physique*, 43:707–713.
- Geim, A. and Grigorieva, I. (2013). Van der waals heterostructures. *Nature*, 499(7459):419–425.
- Geim, A. K. (2009). Graphene: status and prospects. *Science*, 324(5934):1530–1534.
- Geim, A. K. and Novoselov, K. S. (2007). The rise of graphene. *Nature Materials*, 6(3):183–191.
- Gomes, K. K. and *et al.* (2012). Designer Dirac fermions and topological phases in molecular graphene. *Nature*, 483(7389):306–310.
- Gong, L., Kinloch, I. A., Young, R. J., Riaz, I., Jalil, R., and Novoselov, K. S. (2010). Interfacial stress transfer in a graphene monolayer nanocomposite. *Advanced Materials*, 22:2694.

- Guinea, F., Geim, A. K., Katsnelson, M. I., and Novoselov, K. S. (2010a). Generating quantizing pseudomagnetic fields by bending graphene ribbons. *Physical Review B*, 81(3):035408.
- Guinea, F., Horovitz, B., and Le Doussal, P. (2008). Gauge field induced by ripples in graphene. *Physical Review B*, 77:205421.
- Guinea, F., Katsnelson, M. I., and Geim, A. K. (2010b). Energy gaps and a zero-field quantum hall effect in graphene by strain engineering. *Nature Physics*, 6(1):30–33.
- Guinea, F. and Low, T. (2010). Band structure and gaps of triangular graphene superlattices. *Philosophical Transactions of the Royal Society A-Mathematical Physical and Engineering Sciences*, 368(1932):5391–5402.
- Han, D., Pal, S., Liu, Y., and Yan, H. (2010). Folding and cutting dna into reconfigurable topological nanostructures. *Nature Nanotechnology*, 5(10):712–717.
- Han, M. Y., Ozyilmaz, B., Zhang, Y., and Kim, P. (2007). Energy band-gap engineering of graphene nanoribbons. *Physical Review Letters*, 98(20):206805.
- Hansson, A. and Stafström, S. (2003). Intershell conductance in multiwall carbon nanotubes. *Physical Review B*, 67:075406.
- He, R., Zhao, L., Petrone, N., Kim, K. S., Roth, M., Hone, J., Kim, P., Pasupathy, A., and Pinczuk, A. (2012). Large physisorption strain in chemical vapor deposition of graphene on copper substrates. *Nano Letters*, 12(5):2408–2413.
- Hoover, W. G. (1985). Canonical dynamics: Equilibrium phase-space distributions. *Physical Review A*, 31(3):1695–1697.
- Hou, Y., Neville, R., Scarpa, F., Remillat, C., Gu, B., and Ruzzene, M. (2014). Graded conventional-auxetic kirigami sandwich structures: flatwise compression and edgewise loading. *Composites Part B: Engineering*, 59:33–42.
- Huang, Y., Wu, J., and Hwang, K. C. (2006). Thickness of graphene and single-wall carbon nanotubes. *Physical Review B*, 74(24):245413.
- Hughes, T. J. R. (1987). *The Finite Element Method: Linear Static and Dynamic Finite Element Analysis*. Prentice-Hall.
- Humphrey, W., Dalke, A., and Schulten, K. (1996). VMD – Visual Molecular Dynamics. *Journal of Molecular Graphics*, 14(1):33–38.
- Ikeda, H., Qi, Y., Cagin, T., Samwer, K., Johnson, W. L., and Goddard III, W. A. (1999). Strain rate induced amorphization in metallic nanowires. *Physical Review Letters*, 82(14):2900.

- Ilic, B., Yang, Y., and Craighead, H. (2004). Virus detection using nanoelectromechanical devices. *Applied Physics Letters*, 85(13):2604–2606.
- Imboden, M. and Mohanty, P. (2014). Dissipation in nanoelectromechanical systems. *Physics Reports*, 534(3):89 – 146.
- Isacsson, A., Jonsson, L. M., Kinaret, J. M., and Jonson, M. (2008). Electronic superlattices in corrugated graphene. *Physical Review B*, 77:035423.
- Izrailev, F. and Chirikov, B. V. (1966). Statistical properties of a nonlinear spring. *Soviet Physics Doklady*, 11(1):30–32.
- Jiang, J.-W. and Park, H. S. (2014). Negative poisson’s ratio in single-layer black phosphorus. *Nature Communications*, 5:4727.
- Jun, S., Tashi, T., and Park, H. S. (2011). Size-dependence of the nonlinear elastic softening of nanoscale graphene monolayers under plane-strain bulge tests: a molecular dynamics study. *Journal of Nanomaterials*, 2011:380286.
- Jung, J., DaSilva, A., Adam, S., and MacDonald, A. H. (2015). Origin of band gaps in graphene on hexagonal boron nitride. *Nature Communications*, 6:6308.
- Kane, C. L. and Mele, E. J. (1997). Size, shape, and low energy electronic structure of carbon nanotubes. *Physical Review Letters*, 78:1932.
- Kebllinski, P., Wolf, D., and Gleiter, H. (1998). Molecular-dynamics simulation of grain-boundary diffusion creep. *Interface Science*, 6(3):205–212.
- Keyes, R. W. (1953). The electrical properties of black phosphorus. *Physical Review*, 92(3):580.
- Kim, E. A. and Castro Neto, A. H. (2008). Graphene as an electronic membrane. *Europhysics Letters*, 84(5):57007.
- Kim, K.-J., Blanter, Y. M., and Ahn, K.-H. (2011). Interplay between real and pseudomagnetic field in graphene with strain. *Physical Review B*, 84(8):081401.
- Kitt, A., Qi, Z., Remi, S., Park, H. S., Swan, A. K., and Goldberg, B. (2013a). How graphene slides: Measurement and theory of strain-dependent frictional forces between graphene and sio₂. *Nano Letters*, 13(6):2605–2610.
- Kitt, A. L., Pereira, V. M., Swan, A. K., and Goldberg, B. B. (2012). Lattice-corrected strain-induced vector potentials in graphene. *Physical Review B*, 85:115432.
- Kitt, A. L., Pereira, V. M., Swan, A. K., and Goldberg, B. B. (2013b). Erratum: Lattice-corrected strain-induced vector potentials in graphene [phys. rev. b 85, 115432 (2012)]. *Physical Review B*, 87:159909(E).

- Klimov, N. N., Jung, S., Zhu, S. Z., Li, T., Wright, C. A., Solares, S. D., Newell, D. B., Zhitenev, N. B., and Strosio, J. A. (2012). Electromechanical properties of graphene drumheads. *Science*, 336(6088):1557–1561.
- Koenig, S. P., Boddeti, N. G., Dunn, M. L., and Bunch, J. S. (2011). Ultrastrong adhesion of graphene membranes. *Nature Nanotechnology*, 6:543–546.
- LaHaye, M. D., Buu, O., Camarota, B., and Schwab, K. C. (2004). Approaching the quantum limit of a nanomechanical resonator. *Science*, 304(5667):74–77.
- Lammmps (2012). <http://lammmps.sandia.gov>.
- Lee, C., Wei, X., Kysar, J. W., and Hone, J. (2008). Measurement of the elastic properties and intrinsic strength of monolayer graphene. *Science*, 321:385–388.
- Lent, C. S. (1991). Edge states in a circular quantum dot. *Physical Review B*, 43:4179–4186.
- Levy, N., Burke, S. A., Meaker, K. L., Panlasigui, M., Zettl, A., Guinea, F., Castro Neto, A. H., and Crommie, M. F. (2010). Strain-induced pseudo-magnetic fields greater than 300 tesla in graphene nanobubbles. *Science*, 329(5991):544–547.
- Li, J. (2003). Atomeye: an efficient atomistic configuration viewer. *Modelling and Simulation in Materials Science and Engineering*, 11(2):173.
- Lichtenberg, A. J., Livi, R., and Pettini, M. (2008). Dynamics of oscillator chains. In Gallavotti, G., editor, *The Fermi-Pasta-Ulam problem*. Springer.
- Lifshitz, R. and Roukes, M. L. (2000). Thermoelastic damping in micro- and nanomechanical systems. *Physical Review B*, 61:5600–5609.
- Lim, C. H. Y. X., Sorkin, A., Bao, Q., Li, A., Zhang, K., Nesladek, M., and Loh, K. P. (2012). A hydrothermal anvil made of graphene nanobubbles on diamond. *Nature Communications*, 4:1556.
- Liu, F., Ming, P., and Li, J. (2007). Ab initio calculation of ideal strength and phonon instability of graphene under tension. *Physical Review B*, 76(6):064120.
- Lu, J., Castro Neto, A. H., and Loh, K. P. (2012). Transforming moire blisters into geometric graphene nano-bubbles. *Nature Communications*, 3:823.
- Lu, Q., Gao, W., and Huang, R. (2011). Atomistic simulation and continuum modeling of graphene nanoribbons under uniaxial tension. *Modelling and Simulation in Materials Science and Engineering*, 19(5):054006.
- Maekawa, K. and Itoh, A. (1995). Friction and tool wear in nano-scale machining: a molecular dynamics approach. *Wear*, 188(12):115 – 122.

- Mak, K. F., Lee, C., Hone, J., Shan, J., and Heinz, T. F. (2010). Atomically thin mos_2 : a new direct-gap semiconductor. *Physical Review Letters*, 105(4):136805.
- Masir, M. R., Vasilopoulos, P., and Peeters, F. M. (2009). Magnetic Kronig-Penney model for dirac electrons in single-layer graphene. *New Journal of Physics*, 11:095009.
- Masir, M. R., Vasilopoulos, P., and Peeters, F. M. (2011). Graphene in inhomogeneous magnetic fields: bound, quasi-bound and scattering states. *Journal of Physics: Condensed Matter*, 23(31):315301.
- Matheny, M. H., Villanueva, L. G., Karabalin, R. B., Sader, J. E., and Roukes, M. L. (2013). Nonlinear mode-coupling in nanomechanical systems. *Nano Letters*, 13(4):1622–1626.
- McClure, J. W. (1956). Diamagnetism of Graphite. *Physical Review*, 104:666.
- Min, K. and Aluru, N. R. (2011). Mechanical properties of graphene under shear deformation. *Applied Physics Letters*, 98(1):013113.
- Nair, R., Blake, P., Grigorenko, A., Novoselov, K., Booth, T., Stauber, T., Peres, N., and Geim, A. (2008). Fine structure constant defines visual transparency of graphene. *Science*, 320(5881):1308–1308.
- Nair, R. R., Wu, H. A., Jayaram, P. N., Grigorieva, I. V., and Geim, A. K. (2012). Unimpeded permeation of water through helium-leak-tight graphene-based membranes. *Science*, 335(6067):442–444.
- Neek-Amal, M., Covaci, L., and Peeters, F. M. (2012). Nanoengineered nonuniform strain in graphene using nanopillars. *Physical Review B*, 86(4):041405.
- Neek-Amal, M. and Peeters, F. M. (2012a). Strain-engineered graphene through a nanostructured substrate. i. deformations. *Physical Review B*, 85(19):195445.
- Neek-Amal, M. and Peeters, F. M. (2012b). Strain-engineered graphene through a nanostructured substrate. ii. pseudomagnetic fields. *Physical Review B*, 85:195446.
- Neek-Amal, M. and Peeters, F. M. (2014). Graphene on boron-nitride: Moiré pattern in the van der waals energy. *Applied Physics Letters*, 104:041909.
- Ni, Z. H., Yu, T., Lu, Y. H., Wang, Y. Y., Feng, Y. P., and Shen, Z. X. (2009). Uniaxial Strain on Graphene: Raman Spectroscopy Study and Band-Gap Opening. *ACS Nano*, 3:483.
- Novoselov, K. and Neto, A. C. (2012). Two-dimensional crystals-based heterostructures: materials with tailored properties. *Physica Scripta*, 2012(T146):014006.

- Novoselov, K. S., Geim, A. K., Morozov, S., Jiang, D., Zhang, Y., Dubonos, S., Grigorieva, I., and Firsov, A. (2004). Electric field effect in atomically thin carbon films. *Science*, 306(5696):666–669.
- Novoselov, K. S., Geim, A. K., Morozov, S. V., Jiang, D., Katsnelson, M. I., Grigorieva, I. V., Dubonos, S. V., and Firsov, A. A. (2005). Two-dimensional gas of massless Dirac fermions in graphene. *Nature*, 438(7065):197–200.
- Oliva-Leyva, M. and Naumis, G. G. (2013). Understanding electron behavior in strained graphene as a reciprocal space distortion. *Physical Review B*, 88:085430.
- Oshidari, Y., Hatakeyama, T., Kometani, R., Warisawa, S., and Ishihara, S. (2012). High quality factor graphene resonator fabrication using resist shrinkage-induced strain. *Applied Physics Express*, 5:117201.
- Pacheco Sanjuan, A. A., Wang, Z., Imani, H. P., Vanević, M., and Barraza-Lopez, S. (2014). Graphene’s morphology and electronic properties from discrete differential geometry. *Physical Review B*, 89(12):121403.
- Pellegrino, F. M. D., Angilella, G. G. N., and Pucci, R. (2010). Strain effect on the optical conductivity of graphene. *Physical Review B*, 81:035411.
- Penati, T. and Flach, S. (2007). Tail resonances of fermi-pasta-ulam q-breathers and their impact on the pathway to equipartition. *Chaos*, 17(2):023102.
- Pereira, V. M. and Castro Neto, A. H. (2009). Strain engineering of graphene’s electronic structure. *Physical Review Letters*, 103:046801.
- Pereira, V. M., Castro Neto, A. H., Liang, H. Y., and Mahadevan, L. (2010a). Geometry, mechanics, and electronics of singular structures and wrinkles in graphene. *Physical Review Letters*, 105:156603.
- Pereira, V. M., Castro Neto, A. H., and Peres, N. M. R. (2009). Tight-binding approach to uniaxial strain in graphene. *Physical Review B*, 80:045401.
- Pereira, V. M., Ribeiro, R. M., Peres, N. M. R., and Castro Neto, A. H. (2010b). Optical properties of strained graphene. *Europhysics Letters*, 92:67001.
- Pettini, M., Casetti, L., Cerrutti-Sola, M., Franzosi, R., and Cohen, E. G. (2005). Weak and strong chaos in fermi-pasta-ulam models and beyond. *Chaos*, 15(1).
- Pettini, M. and Landolfi, M. (1990). Relaxation properties and ergodicity breaking in nonlinear hamiltonian dynamics. *Physical Review A*, 41(2):768–783.
- Piana, S. and Bilic, A. (2006). The nature of the adsorption of nucleobases on the gold 111 surface. *Journal of Physical Chemistry B*, 110(46):23467–23471.

- Plimpton, S. (1995). Fast parallel algorithms for short-range molecular-dynamics. *Journal of Computational Physics*, 117(1):1–19.
- Qi, Z., Bahamon, D. A., Pereira, V. M., Park, H. S., Campbell, D. K., and Castro Neto, A. H. (2013). Resonant tunneling in graphene pseudomagnetic quantum dots. *Nano Letters*, 13(6):2692–2697.
- Qi, Z., Kitt, A. L., Park, H. S., Pereira, V. M., Campbell, D. K., and Castro Neto, A. H. (2014). Pseudomagnetic fields in graphene nanobubbles of constrained geometry: A molecular dynamics study. *Physical Review B*, 90:125419.
- Qi, Z. and Park, H. S. (2012). Intrinsic energy dissipation in cvd-grown graphene nanoresonators. *Nanoscale*, 4:3460–3465.
- Qi, Z., Zhao, F., Zhou, X., Sun, Z., Park, H., and Wu, H. (2010). A molecular simulation analysis of producing monatomic carbon chains by stretching ultranarrow graphene nanoribbons. *Nanotechnology*, 21(26):7.
- Remus, L. G., Blencowe, M. P., and Tanaka, Y. (2009). Damping and decoherence of a nanomechanical resonator due to a few two-level systems. *Physical Review B*, 80:174103.
- Ribeiro, R. M. and *et al.* (2009). Strained graphene: tight-binding and density functional calculations. *New Journal of Physics*, 11:115002.
- Rodin, A., Carvalho, A., and Neto, A. C. (2014). Strain-induced gap modification in black phosphorus. *Physical Review Letters*, 112(17):176801.
- Rose, P., Huang, P., Blees, M., Barnard, A., Muller, D., and McEuen, P. (2014). Focused ion beam patterning of suspended graphene for cantilever and kirigami devices. <http://meetings.aps.org/link/BAPS.2014.MAR.L30.5>.
- Rytken, A., Valkealahti, S., and Manninen, M. (1998). Phase diagram of argon clusters. *Journal of Chemical Physics*, 108(14):5826–5833.
- San-Jose, P., Gutiérrez-Rubio, A., Sturla, M., and Guinea, F. (2014). Spontaneous strains and gap in graphene on boron nitride. *Physical Review B*, 90:075428.
- Sareh, S. and Rossiter, J. (2013). Kirigami artificial muscles with complex biologically inspired morphologies. *Smart Materials and Structures*, 22(1):014004.
- Seol, J. H., Jo, I., Moore, A. L., Lindsay, L., Aitken, Z. H., Pettes, M. T., Li, X., Yao, Z., Huang, R., Broido, D., Mingo, N., Ruoff, R. S., and Shi, L. (2010). Two-dimensional phonon transport in supported graphene. *Science*, 328(5975):213–216.

- Sharma, A., Kotov, V. N., and Castro Neto, A. H. (2013). Effect of uniaxial strain on ferromagnetic instability and formation of localized magnetic states on adatoms in graphene. *Physical Review B*, 87:155431.
- Sivan, U., Imry, Y., and Hartzstein, C. (1989). Aharonov-Bohm and quantum Hall effects in singly connected quantum dots. *Physical Review B*, 39:1242–1250.
- Sloan, J. V., Sanjuan, A. A. P., Wang, Z., Horvath, C., and Barraza-Lopez, S. (2013). Strain gauge fields for rippled graphene membranes under central mechanical load: An approach beyond first-order continuum elasticity. *Physical Review B*, 87:155436.
- Stuart, S. J., Tutein, A. B., and Harrison, J. A. (2000). A reactive potential for hydrocarbons with intermolecular interactions. *Journal of Chemical Physics*, 112(14):6472–6486.
- Suzuura, H. and Ando, T. (2002). Phonons and electron-phonon scattering in carbon nanotubes. *Physical Review B*, 65:235412.
- Temko, F. and Takahama, T. (1978). *The Magic of Kirigami: Happenings with Paper and Scissors by Florance Temko and Toshie Takahama*. Japan Publications, Incorporated.
- Thompson, A. P., Plimpton, S. J., and Mattson, W. (2009). General formulation of pressure and stress tensor for arbitrary many-body interaction potentials under periodic boundary conditions. *Journal of Chemical Physics*, 131(15).
- Tildesley, D. and Allen, M. (1987). *Computer simulation of liquids*. Clarendon, Oxford.
- Tomori, H., Kanda, A., Goto, H., Ootuka, Y., Tsukagoshi, K., Moriyama, S., Watanabe, E., and Tsuya, D. (2011). Introducing nonuniform strain to graphene using dielectric nanopillars. *Applied Physics Express*, 4(7):3.
- Tuzun, R. E., Noid, D. W., Sumpter, B. G., and Merkle, R. C. (1996). Dynamics of fluid flow inside carbon nanotubes. *Nanotechnology*, 7(3):241.
- van der Zande, A. M., Barton, R. A., Alden, J. S., Ruiz-Vargas, C. S., Whitney, W. S., Pham, P. H. Q., Park, J., Parpia, J. M., Craighead, H. G., and McEuen, P. L. (2010). Large-scale arrays of single-layer graphene resonators. *Nano Letters*, 10(12):4869–4873.
- Wallace, P. R. (1947). The band theory of graphite. *Physical Review*, 71(9):622.
- Wang, M. and *et al.* (2012). Effect of defects on fracture strength of graphene sheets. *Computational Materials Science*, 54(0):236–239.

- Wang, P., Gao, W., Cao, Z., Liechti, K. M., and Huang, R. (2013). Numerical analysis of circular graphene bubbles. *Journal of Applied Mechanics*, 80(4):040905.
- Wang, Z. F., Zhang, Y., and Liu, F. (2011). Formation of hydrogenated graphene nanoripples by strain engineering and directed surface self-assembly. *Physical Review B*, 83:041403.
- Wei, Y., Wang, B., Wu, J., Yang, R., and Dunn, M. L. (2013). Bending rigidity and gaussian bending stiffness of single-layered graphene. *Nano Letters*, 13(1):26–30.
- Wilson-Rae, I. (2008). Intrinsic dissipation in nanomechanical resonators due to phonon tunneling. *Physical Review B*, 77(24):245418.
- Wolf, D., Yamakov, V., Phillpot, S., Mukherjee, A., and Gleiter, H. (2005). Deformation of nanocrystalline materials by molecular-dynamics simulation: relationship to experiments? *Acta Materialia*, 53(1):1–40.
- Woods, C., Britnell, L., Eckmann, A., Ma, R., Lu, J., Guo, H., Lin, X., Yu, G., Cao, Y., Gorbachev, R., et al. (2014). Commensurate-incommensurate transition in graphene on hexagonal boron nitride. *Nature Physics*, 10(6):451–456.
- Xiaodong, L. L. T. (2007). The visual extension of kirigami in modern art. *Art and Design*, 10:066.
- Yamakov, V., Wolf, D., Phillpot, S. R., Mukherjee, A. K., and Gleiter, H. (2002). Dislocation processes in the deformation of nanocrystalline aluminium by molecular-dynamics simulation. *Nature Materials*, 1(1):45–49.
- Yang, H. T. (2011). Strain induced shift of dirac points and the pseudo-magnetic field in graphene. *Journal of Physics-Condensed Matter*, 23(50).
- Yeh, N. C., Teague, M. L., Yeom, S., Standley, B. L., Wu, R. T. P., Boyd, D. A., and Bockrath, M. W. (2011). Strain-induced pseudo-magnetic fields and charging effects on cvd-grown graphene. *Surface Science*, 605(17-18):1649–1656.
- Yue, K., Gao, W., Huang, R., and Liechti, K. M. (2012). Analytical methods for the mechanics of graphene bubbles. *Journal of Applied Physics*, 112(8):083512.
- Zabusky, N. J. and Kruskal, M. D. (1965). Interaction of "solitons" in a collisionless plasma and the recurrence of initial states. *Physical Review Letters*, 15(6):240–243.
- Zhang, P., Ma, L., Fan, F., Zeng, Z., Peng, C., Loya, P. E., Liu, Z., Gong, Y., Zhang, J., Zhang, X., et al. (2014). Fracture toughness of graphene. *Nature Communications*, 5:3782.

- Zhang, Y., Tan, Y.-W., Stormer, H. L., and Kim, P. (2005). Experimental observation of the quantum hall effect and berry's phase in graphene. *Nature*, 438(7065):201–204.
- Zhao, H. and Aluru, N. R. (2010). Temperature and strain-rate dependent fracture strength of graphene. *Journal of Applied Physics*, 108(6):064321.
- Zhao, H., Min, K., and Aluru, N. R. (2009). Size and Chirality Dependent Elastic Properties of Graphene Nanoribbons under Uniaxial Tension. *Nano Letters*, 9(8):3012–3015.
- Zhi, L. and Mullen, K. (2008). A bottom-up approach from molecular nanographenes to unconventional carbon materials. *Journal of Materials Chemistry*, 18:1472.
- Zhu, S., Huang, Y., and Li, T. (2014). Extremely compliant and highly stretchable patterned graphene. *Applied Physics Letters*, 104(17):173103.

CURRICULUM VITAE

ZENAN QI

EDUCATION

2015 **Ph.D.** Boston University, Mechanical Engineering
2012 **M.S.** Boston University, Mechanical Engineering
2010 **B.S.** University of Sci. & Technol. of China, Modern Mechanics

PROFESSIONAL EXPERIENCE

Research Assistant May 2011 - May 2015
Boston University, Mechanical Engineering

Visiting Researcher Sept. - Oct. 2013
Chalmers University of Technology, Sweden

Visiting Researcher Jun. - Jul. 2011, Jun. - Aug. 2012, Jan. - Mar. 2013
Graphene Research Center, National University of Singapore, Singapore

Teaching Assistant Sept. 2010 - May 2011
Boston University, Mechanical Engineering

PUBLICATIONS

1. Z. Qi, J. Zhang, G. Zhang, H.S. Park, Coupling tension and shear for highly sensitive graphene-based strain sensors, submitted
2. D. A. Bahamon, Z. Qi, H.S. Park, V.M. Pereira, D.K. Campbell, Conductance signatures of electron confinement induced by strained nanobubbles in graphene, submitted
3. Z. Qi, D.K. Campbell, H.S. Park, Atomistic simulations of tension-induced large deformation and stretchability in graphene kirigami, Physical Review B, 2014, 90:245437
4. Z. Qi, A.L. Kitt, H.S. Park, V.M. Pereira, D.K. Campbell, A.H. Castro Neto, Pseudomagnetic fields in graphene nanobubbles of constrained geometry: a molecular dynamics study, Physical Review B, 2014, 90:125419

5. D. Midtvedt, Z. Qi, A. Croy, H.S. Park, A. Isacsson, Fermi-Pasta-Ulam physics with nanomechanical graphene resonators: Intrinsic relaxation and thermalization in nanomechanical graphene drums, *Physical Review Letters*, 2014, 112(14):145503
6. Z. Qi, D.A. Bahamon, V.M. Pereira, H.S. Park, D.K. Campbell, A.H. Castro Neto, Resonant tunneling in graphene pseudomagnetic quantum dots, *Nano Letters* 2013, 13 (6):2692-2697
7. A.L. Kitt, Z. Qi, S. Remi, H.S. Park, A.K. Swan, B.B. Goldberg, How graphene slides: measurement and theory of frictional forces between graphene and SiO₂, *Nano Letters* 2013, 13 (6):2605-2610
8. Z. Qi, P. Cao, H.S. Park, Density functional theory calculation of edge stresses in monolayer MoS₂, *Journal of Applied Physics* 2013, 114:163508
9. J.W. Jiang, Z. Qi, H.S. Park, T. Rabczuk, Elastic bending modulus of single-layer molybdenum disulphide (MoS₂): finite thickness effect, *Nanotechnology* 2013, 24:435705
10. Z. Qi, H.S. Park, Intrinsic energy dissipation in CVD-grown graphene nanoresonators, *Nanoscale* 2012, 4(11):3460-3465
11. Z. Qi, F. Zhao, X. Zhou, Z. Sun, H.S. Park, H. Wu, A molecular simulation analysis of producing monatomic carbon chains by stretching ultranarrow graphene nanoribbons, *Nanotechnology* 2010. 21(26): 265702

CONFERENCES

1. Z. Qi, D.A. Bahamon, D.K. Campbell, H.S. Park, Kirigami for Two-Dimensional Electronic Membranes, *Bulletin of the American Physical Society*, San Antonio, TX, March 2015
2. Z. Qi, H.S. Park, D.K. Campbell, Highly Ductile Graphene Kirigami, XXVI IUPAP Conference on Computational Physics, Boston, MA, August 2014
3. Z. Qi, D. Bahamon, A.L. Kitt, V.M. Pereira, H.S. Park, D.K. Campbell, A.H. Castro Neto, Strain Engineering of Graphene Hexagon and Nanobubbles, XXVI IUPAP Conference on Computational Physics, Boston, MA, August 2014
4. Z. Qi, D.A. Bahamon, V.M. Pereira, H.S. Park, D.K. Campbell, A.H. Castro Neto, Strain Engineering of Graphene: Atomistic Simulation of Y-junctions and Nanobubbles, *Bulletin of the American Physical Society*, Denver, CO, March 2014

5. D. Midtvedt, Z. Qi, A. Croy, H.S. Park, A. Isacsson, Intrinsic Mode-Coupling and Thermalization in Nanomechanical Graphene Drums, Bulletin of the American Physical Society, Denver, CO, March 2014
6. Z. Qi, D.A. Bahamon, V.M. Pereira, H.S. Park, D.K. Campbell, A.H. Castro Neto, Resonance Tunneling in Graphene Pseudomagnetic Quantum Dots, Boston Area CarbOn Nanoscience Meeting, June 2013, Boston University
7. D. Midtvedt, A. Croy, Z. Qi, H.S. Park, A. Isacsson, Thermally Assisted Energy Relaxation in Nanomechanical Graphene Resonators, Graphene Week 2013, Chemnitz, Germany, June 2013
8. Z. Qi, D.A. Bahamon, V.M. Pereira, H.S. Park, D.K. Campbell, A.H. Castro Neto, Mechanical-Electronic Coupling of Graphene Y-Junction, NewMech Workshop, Northeastern University, October 2013
9. Z. Qi, H.S. Park, V.M. Pereira, A.H. Castro Neto, D.K. Campbell, Molecular Dynamics Studies of Graphene Nanobubbles, Bulletin of the American Physical Society, Baltimore, MD, March 2013
10. A. Kitt, Z. Qi, H.S. Park, A.K. Swan, B.B. Goldberg, Graphene Slides Over the Substrate When You Pull It: Direct Measurement, Theory, and Frictional Forces, Bulletin of the American Physical Society, Baltimore, MD, March 2013
11. Z. Qi, H.S. Park, Q-factors of Graphene Nanoresonators with Extended Defects, Boston Area CarbOn Nanoscience Meeting, Harvard University, April 2012

SEMINARS/TALKS

1. Strain Engineering of Graphene: Quantum Dots and Nanobubbles, Chalmers University of Technology, Applied Physics Department, Gothenburg, Sweden, Sept. 2013
2. Strain Engineering of Graphene: Resonators and Quantum Dots, University of Science and Technology of China, Department of Modern Mechanics, Hefei, China, Aug. 2013
3. Strain Engineering of Graphene: Resonator, Quantum Dot and Nanobubble, Cabot Headquarter in Boston, Cabot Poster Day, May 2013
4. Strain Engineering of Graphene: Nanobubbles and Resonators, Nanyang Technological University, Singapore, Feb. 2013